

**DESIGN PRINCIPLES AND MODELLING OF
MICROTUBULAR ELECTROCHEMICAL REACTORS: THE CASE
OF A FLOW BATTERY**

A Dissertation
Presented to
The Academic Faculty

by

Alexandros Filippas

In Partial Fulfillment
of the Requirements for the Degree
Doctor of Philosophy in the
School of Chemical and Biomolecular Engineering

Georgia Institute of Technology
December 2024

COPYRIGHT © 2024 BY ALEXANDROS FILIPPAS

**DESIGN PRINCIPLES AND MODELLING OF
MICROTUBULAR ELECTROCHEMICAL REACTORS: THE CASE
OF A FLOW BATTERY**

Approved by:

Dr. Nian Liu, Advisor
School of Chemical and
Biomolecular Engineering
Georgia Institute of Technology

Dr. Carsten Sievers
School of Chemical and
Biomolecular Engineering
Georgia Institute of Technology

Dr. Thomas Fuller
School of Chemical and
Biomolecular Engineering
Georgia Institute of Technology

Dr. Marta Hatzell
School of Mechanical
Engineering
Georgia Institute of Technology

Dr. Ryan Lively
School of Chemical and
Biomolecular Engineering
Georgia Institute of Technology

Dr. Brian Berland
Stryten Energy

Date Approved: December 3,
2024

This thesis is dedicated to my brother and my family

ACKNOWLEDGEMENTS

First and foremost, I would like to thank Professor Nian Liu for his guidance and support throughout my PhD journey. The academic and non-academic lessons I learnt from him along with his patience and understanding of my needs and challenges have been instrumental in helping me reach the finish line. I am also grateful to Professor Thomas Fuller for his insightful feedback and direct guidance, which have been crucial to the development of my work. Special thanks to Dr. Brian Berland whose thought-provoking questions triggered much of the work presented in this thesis. I would also like to thank my Thesis Committee members, Professor Ryan Lively, Marta Hatzell, Carsten Sievers, for their constructive advice and encouragement over the course of my PhD. My appreciation extends to Nick Gomez and Nidhi Menon for all the technical advice and resources they offered.

I would also like to thank our current lab's group members since they made my work environment a nice and friendly place to be; Karam who became a close friend, Lotanna for working with me and offering her help whenever needed, Zhitao for his assistance in the lab. Special thanks to my first lab mate Yutong Wu, now a Professor in Nanjing Tech University, who mentored me in my first semester in the lab and shared his knowledge and expertise on microtubular flow batteries.

Beyond the lab, I met many people in Atlanta for whom I would like to say a few words. My first roommate, Minas, was someone I barely knew when we moved in together and we became close friends by the time he moved out. As a senior Ph.D. student in Atlanta, he taught me many things, from the PhD itself to where I can find the best wings

in the city. Markos, my second roommate, dear friend, and an example of how you can be laid-back and driven at the same time. Harini and the coffee breaks, Hector the liaison, Elisavet, George, Myrto and many others who I will miss-though not every name appears here, to keep this acknowledgement from becoming a thesis of its own.

Outside the university, I would like to thank my brother and my parents for their support. I cannot imagine how difficult it must have been for them when their child moved six thousand miles away. To Nickos and Iasonas, in happiness and despair, in ecstasy and stillness, through the dusk and through the dawn, I have never felt alone. And finally, Dafni-the person who held my hand across an ocean, always reminding me the power of faith.

Finally, I would like to acknowledge Stryten Energy for funding this work, along with the Onassis and Bodossakis fellowships for the additional support they provided me throughout my PhD.

TABLE OF CONTENTS

ACKNOWLEDGEMENTS	iv
LIST OF TABLES	viii
LIST OF FIGURES	ix
LIST OF SYMBOLS	xiv
SUMMARY	xviii
CHAPTER 1. Introduction	1
1.1 General Background	1
1.2 Basics of Electrochemical Flow Reactors	1
1.3 Tubular Flow Reactors	4
1.4 Redox Flow Batteries	6
1.5 Research Problem and Hypothesis	7
1.6 Significance and Contribution of the Study	8
1.7 Thesis Outline	9
CHAPTER 2. Effect of Electrode Porosity and Configuration on Ohmic Losses of Tubular Flow Batteries	11
2.1 Introduction	11
2.2 Methods	11
2.2.1 Materials	11
2.2.2 Flow Cells	12
2.2.3 Electrochemical Characterization	14
2.2.4 Numerical Simulations	14
2.3 Results and Discussion	15
2.3.1 Overview	15
2.3.2 Preliminary Results	16
2.3.3 Ohmic Resistance Analysis	17
2.3.4 Electrode Resistance	18
2.3.5 Electrolyte and Separator Resistance	20
2.3.6 Evaluation of Electrode Configurations	23
2.3.7 Scalability	29
2.4 Conclusions	30
CHAPTER 3. An Analytical Model for Tubular Flow Reactors	31
3.1 Introduction	31
3.2 Model Development	32
3.2.1 Linear Kinetics Formulation	35
3.2.2 Tafel Kinetics Formulation	41
3.3 Results and Discussion	44
3.3.1 Current and Current Density Distribution along the Reactor Length	44

3.3.2	Electrode Potential Distribution along the Reactor Length	50
3.3.3	Reactor Resistance and Area Specific Resistance	52
3.3.4	Porous Electrode Theory and Tubular Reactor Model Comparison	59
3.3.5	Limitations of the Model	64
3.4	Conclusions	65
CHAPTER 4. Enhanced Scalability in Microtubular Vanadium Flow Batteries Via Copper Anodes		66
4.1	Introduction	66
4.2	Methods	68
4.2.1	Materials	68
4.2.2	Flow Cells	68
4.2.3	Electrochemical Characterization	69
4.3	Results	70
4.3.1	Anode Material Selection Process	70
4.3.2	Copper Anode and Graphite Anode VRFB Full-Cell Testing	77
4.3.3	Scalability Comparison of Half-Cell Symmetric Flow Batteries	79
4.3.4	Full-Cell Cycling Performance Comparison of Copper and Graphite Anode	79
4.3.5	Microtubular Copper and Carbon Fiber-based Anode Full-Cell Testing	80
4.4	Conclusions	82
CHAPTER 5. Conclusions and Future Directions		84
5.1	Conclusions	84
5.2	Future Work	87
5.2.1	Anode Coulombic Efficiency Improvements	88
5.2.2	Cathode Electrode Design	89
5.2.3	Mass Transport Investigation	90
 REFERENCES		 92

LIST OF TABLES

Table 2.1 – Parameters of the coaxial and non-coaxial flow cells used in the experiments and the simulations. ⁵⁰	22
Table 2.2 – Parameters used in the COMSOL simulations to evaluate current density distribution, ASR, and VSR.	25
Table 3.1 – Parameters used when using the model equations to visualize trends in the ASR of a tubular Vanadium Flow Battery as a case study. The values depicted are typical values found in parallel plate VRFB studies in the literature.	49
Table 3.2 - Geometric parameters used in the COMSOL simulation and the analytical solution to evaluate the deviation at high polarizations.	50
Table 4.1 – Parameters used in the estimation of the ASR of a 50 cm long electrode.	74

LIST OF FIGURES

Figure 1.1 – a. Undivided parallel plate reactor configuration, b. Undivided coaxial electrode configuration, c. Divided parallel plate reactor configuration, d. Divided coaxial electrode configuration, e. Flow-by configuration, f. Flow-through configuration, g. Monopolar reactor connection, h. Bipolar reactor connection.	3
Figure 1.2 – a. Coaxial microtubular reactor, b. Non-coaxial bundled microtubular reactor, c. Surface area per unit volume of an array of tubular and planar membranes.	6
Figure 1.3 – a. Redox Flow Battery (RFB) schematic b. Power unit schematic. ⁴⁰	7
Figure 1.4 – a. U.S. storage capacity predictions, b. ESS grouped by power and discharge time, c. Total installed cost comparison between VRFBs and Li-ion NMC batteries. ^{15,42,46}	8
Figure 2.1 – a. Coaxial flow cell fabrication steps b. Picture of the coaxial flow cell	13
Figure 2.2 – a. Porous carbon fiber-based electrodes typically used in VRFBs, b. Carbon fiber bundle electrode used in ZnI ₂ microtubular flow batteries. ^{16,39}	16
Figure 2.3 – a. Schematic of the microtubular carbon VRFB with carbon fiber electrodes, b. EIS spectrum and c. polarization curve of the carbon fiber-based VRFB	17
Figure 2.4 – The components of the ohmic resistance in a tubular flow battery showing the solid phase resistance from the electrode and the ionic resistance of the electrolyte and the separator.	18

Figure 2.5 – a. Schematic of a flow battery with carbon fiber and carbon rod-based electrodes, b. Cross-section are comparison, c. EIS spectra and d. polarization curves of the two VRFBs. 20

Figure 2.6 - a. Schematic of the co-axial configuration b. Schematic of the non-coaxial configuration with one outer electrode c. EIS of the co-axial and non-coaxial configuration d. Primary current distribution of the two configurations obtained in COMSOL e. ASR measured based on COMSOL's primary current distribution solution and the HFR obtained from EIS experimentally. 22

Figure 2.7 – a. A scaled-up coaxial configuration with a honeycomb-structured outer electrode, b. A scaled-up quasi-coaxial configuration with wire/rod-shaped outer electrodes 24

Figure 2.8 – a. Current density distribution for the coaxial configuration b. Current density distribution for the quasi-coaxial configuration, c. The current density distribution at the inner surface of the membrane as it changes with the polar angle d. The current density distribution over the average current density at the inner surface of the membrane as it changes with the polar angle. 26

Figure 2.9 – Schematic of the a. gap between the membrane and the outer coaxial tubular electrode, b. gap between the membrane and the outer rod-shaped electrode, c. half the thickness of the outer honeycombed-shaped electrode in the coaxial configuration, d. the radius of the outer rod-shaped electrode in the quasi-coaxial configuration. The variation of the ASR and the VSR as estimated from the primary current distribution simulation versus, e., g. the gap between the outer electrode and the membrane, f., h. half the thickness of the outer electrode. 28

Figure 2.10 – Schematics of the a. 5cm active length battery, b. 10 cm active length battery. c. Polarization curve comparison, d. EIS spectra comparison, e. HFR comparison 29

Figure 3.1 - Qualitative current distribution a) throughout the separator of the parallel plate reactor b) along the separator of the tubular reactor. 33

Figure 3.2 - a) Schematic of a tubular reactor. b) Tubular reactor model geometry. 34

Figure 3.3 – Cross section of the tubular reactor and a sector showing the resistances and the potentials in the radial direction	37
Figure 3.4 - Schematic of the Charge transfer resistance normalized by unit length for the cylindrical geometry.	38
Figure 3.5 - a) Schematic of the current density distribution for a tubular flow reactor. b) Schematic of the distribution of the current in the electrodes for a tubular flow reactor. c) Current density distribution for different values of the parameter ν and for $K_r=1$. d) Current density distribution for different values of the parameter K_r and for $\nu=1$. Distribution of the current in the electrodes for e) $K_r=1$ and $\nu=1$, f) $K_r=1$ and $\nu=10$, g) $K_r=10$ and $\nu=10$.	48
Figure 3.6 - Comparison of the normalized current distribution predicted by the analytical model with linear kinetics and by COMSOL with Butler-Volmer kinetics a) at 1 mA cm ⁻² b) at 10 mA cm ⁻² c) at 1000 mA cm ⁻²	49
Figure 3.7 - Inner (blue) and outer (red) electrode potential distribution a) $K_r=1$ and $\nu=1$, b) $K_r=1$ and $\nu=10$, c) $K_r=10$ and $\nu=1$.	52
Figure 3.8 - a) Changes in reactor geometry by changing interelectrode gap or radius of inner electrode b) Minimum Area Specific Resistance variation with interelectrode gap when radius of inner electrode equals to 0.1 mm c) Minimum Area Specific Resistance variation with inner electrode radius when interelectrode gap equals to 2 mm d) Minimum Area Specific Resistance variation with interelectrode gap when radius of inner electrode equals to 1 mm c) Minimum Area Specific Resistance variation with inner electrode radius when interelectrode gap equals to 1 mm	56
Figure 3.9 - a) Ratio of ASR to minimum ASR variation with ν for different values of K_r b) Total ASR variation with tubular reactor length for different inner electrode materials and $ASR_{min}=1$, $r_s=1$ mm, $r_1=0.5$ mm. c) Total ASR variation with tubular reactor length for Ti inner electrode with different radii and interelectrode gap of $d=0.5$ mm. d) Total ASR variation with tubular reactor length for Ti inner electrode with different interelectrode gaps and inner electrode radius of $r_1=1$ mm.	59

Figure 3.10 - a) Comparison of the ASR of the porous electrode model and tubular reactor model. b) Dependence of dimensionless ASR of the porous electrode model and of the tubular reactor model on the dimensionless parameter v .	63
Figure 3.11 - a) Flow-by electrodes b) Flow-by (porous) electrodes c) Flow-through (porous) electrodes	64
Figure 4.1 – a. The elements of the periodic table that are more conductive than graphite b. The potential of the anode as the SOC changes (black line) and the potential at 0.1% SOC (red line) c. The elements of the periodic table whose standard reduction potential is above the potential at 0.1% SOC. ^{71,73,74}	72
Figure 4.2 - The percentage ASR increase from a infinitesimally short electrode to a 50 cm electrode and the cost of the electrode material. ⁷⁶	74
Figure 4.3 – a. Cyclic voltammograms of Cu wire and graphite rod in V^{3+} solution at 50 mV s^{-1} in a wide potential range showing all possible reactions b. Cyclic voltammograms of Cu wire and graphite rod at 25, 50, 75, and 100 mV s^{-1} targeting the potential range that the anodic vanadium reaction occurs c. The peak separation for the two samples at each scan rate plotted against the logarithm of the scan rate.	76
Figure 4.4 – Schematics of a. the graphite-anode flow battery configuration and b. the copper-anode flow battery c. EIS spectra and d. Polarization curves of the VRFBs with Cu and the graphite anodes e. The polarization curve along with the iR -free polarization curve f. Overpotential breakdown into ohmic and non-ohmic(kinetic and mass transport) at 10 mA cm^{-2} . The flowrates of the inner and outer flow channel were 10 mL min^{-1} and 25 mL min^{-1} respectively.	78
Figure 4.5 – a. Schematic of the symmetric batteries b. Comparison of the ASR increase over length for copper and graphite symmetric batteries.	79
Figure 4.6 – a. Full cell cycling data at 3 mA cm^{-2} for two flow batteries, one with copper anode and one with graphite anode b. Coulombic efficiency c.	80

Voltage efficiency and d. Energy Efficiency comparison for the 2nd to the 6th cycle

Figure 4.7 – Schematic of a microtubular VRFB with a. carbon fibers as anode b. copper wire as anode c. EIS and d. polarization curve comparison of these two batteries. 82

Figure 5.1 – a. Evolution of ASR over the design generations in this thesis b. Comparison of the ASR of the final microtubular flow battery with a Cu-based anode, the best tubular flow battery performance in the literature along with a typical parallel plate flow battery ASR.^{18,47} 87

Figure 5.2 - Outline of completed and future work to be done. 88

Figure 5.3 – a. Schematic of slurry coated Cu wire b. Picture of a coated wire inside a hollow fiber membrane. SEM picture of c. Bare wire d. Slurry coated wire 89

Figure 5.4 – Increasing electrode surface area by using bundled wires. 91

LIST OF SYMBOLS

Symbol	Description	Units
Latin		
a	Specific interfacial area of the porous electrode	cm^{-1}
a_1	Specific interfacial area of the inner electrode	cm^{-1}
A_{c1}	Cross-sectional area of the inner electrode	cm^2
A_{c2}	Cross-sectional area of the outer electrode	cm^2
A_p	Geometric surface area of the porous electrode	cm^2
ASR	Area Specific resistance of the tubular reactor	$\Omega \text{ cm}^2$
ASR_{min}	Minimum ASR, when the length of the reactor approaches zero	$\Omega \text{ cm}^2$
ASR_p	Area Specific resistance of the porous electrode	$\Omega \text{ cm}^2$
F	Faraday constant	C mol^{-1}
i_1	Current density in the solid phase of the inner electrode	mA cm^{-2}
i_2	Current density in the solid phase of the outer electrode	mA cm^{-2}
$i_{n,1}$	Current density due to the redox reaction on the inner electrode surface	mA cm^{-2}
$i_{n,2}$	Current density due to the redox reaction on the outer electrode surface	mA cm^{-2}
i_s	Current density in the separator	mA cm^{-2}
$i_{0,1}$	Exchange current density of the reaction taking place on the inner electrode	mA cm^{-2}
$i_{0,2}$	Exchange current density of the reaction taking place on the outer electrode	mA cm^{-2}
$i_{1,s}$	Electrolyte current density close to the inner electrode	mA cm^{-2}
$i_{2,s}$	Electrolyte current density close to the outer electrode	mA cm^{-2}

I_1	Total current in the solid phase of the inner electrode	mA
I_2	Total current in the solid phase of the outer electrode	mA
I	Total current applied to the reactor	mA
I^*	Dimensionless current in the solid phase of the outer electrode	-
K_r	Dimensionless ratio of conductivities of the outer and the inner electrode	-
$K_{r,p}$	Dimensionless ratio of conductivities of the electrolyte and the electrode in the porous electrode	-
L	Reactor length	cm
L_p	Porous electrode thickness	cm
r_s	Separator radius	cm
r_1	Inner electrode radius	cm
$r_{2,I}$	Outer electrode inner radius	cm
$r_{2,O}$	Outer electrode outer radius	cm
R	Universal gas constant	$\text{J mol}^{-1} \text{K}^{-1}$
R_p	Porous electrode total resistance	Ω
R_{planar}	Planar cell total resistance	Ω
R_s	Planar cell separator resistance	Ω
R_{tot}	Tubular reactor total resistance	Ω
$R_{ct,p}$	Charge-transfer resistance of the porous electrode normalized by the interfacial area	$\Omega \text{ cm}^2$
R_{ct1}	Charge-transfer resistance of the inner electrode normalized by the electrode surface area	$\Omega \text{ cm}^2$
R_{ct2}	Charge-transfer resistance of the outer electrode normalized by the electrode surface area	$\Omega \text{ cm}^2$
R_{ct1}^l	Charge-transfer resistance of the inner electrode normalized by the reactor length	$\Omega \text{ cm}$
R_{ct2}^l	Charge-transfer resistance of the outer electrode normalized by the reactor length	$\Omega \text{ cm}$

R_{el}^l	Ohmic resistance of the electrolyte normalized by the reactor length	Ω cm
R_{el1}^l	Ohmic resistance of the electrolyte of the inner flow channel normalized by the reactor length	Ω cm
R_{el2}^l	Ohmic resistance of the electrolyte of the outer flow channel normalized by the reactor length	Ω cm
R_s^l	Ohmic resistance of the separator normalized by the reactor length	Ω cm
R_{tot}^l	Sum of resistances in the radial direction, including charge-transfer resistance of the two electrodes, separator resistance, and electrolyte resistance normalized by the reactor length	Ω cm
T	Absolute temperature	K
U	Equilibrium voltage of the reactor	V
U_1	Equilibrium potential of the reaction of the inner electrode	V
U_2	Equilibrium potential of the reaction of the outer electrode	V
w	Separator thickness	cm
x	x-coordinate	cm
z	Dimensionless x-coordinate	-

Greek

$\alpha_{a,1}$	Anodic charge-transfer coefficient of the inner electrode reaction	-
$\alpha_{c,1}$	Cathodic charge-transfer coefficient of the inner electrode reaction	-
β_1	Inverse Tafel slope for the anodic charge-transfer reaction of the inner electrode	V^{-1}
β_2	Inverse Tafel slope for the cathodic charge-transfer reaction of the outer electrode	V^{-1}
γ	Dimensionless parameter, defined by Eq. A8a	-
δ	Dimensionless parameter, defined by Eq. A8b	-
ε	Dimensionless parameter, defined by Eq. A8c	-
κ	Porous electrode electrolyte ionic conductivity	$S\text{ cm}^{-1}$
κ_{el}	Tubular reactor electrolyte ionic conductivity	$S\text{ cm}^{-1}$

κ_s	Tubular reactor separator ionic conductivity	S cm^{-1}
ν	Square root of the dimensionless ratio of the ohmic resistance of the electrodes and the resistances in the radial direction	-
ν_p	Square root of the dimensionless ratio of the ohmic resistance of the porous electrode and the charge transfer resistance	-
σ	Electrical conductivity of the solid phase of the porous electrode	S cm^{-1}
σ_1	Electronic conductivity of the inner electrode material	S cm^{-1}
σ_2	Electronic conductivity of the outer electrode material	S cm^{-1}
φ_1	Potential of the inner electrode	V
$\varphi_{1,s}$	Potential of the electrolyte outside the double layer of the inner electrode	V
$\varphi_{1,sp}$	Potential of the electrolyte-separator interface in the inner flow channel	V
$\varphi_{2,sp}$	Potential of the electrolyte-separator interface in the outer flow channel	V
φ_2	Potential of the outer electrode	V
$\varphi_{2,s}$	Potential of the electrolyte outside the double layer of the outer electrode	V
φ_1^*	Dimensional potential of the inner electrode	-
φ_2^*	Dimensional potential of the outer electrode	-

SUMMARY

This thesis investigates the performance and scalability of microtubular vanadium redox flow batteries (VRFBs), addressing key factors such as ohmic resistance, electrode configuration, and material selection. A systematic approach combining experimental studies, analytical modeling, and numerical simulations provides critical insights into the challenges and opportunities for advancing microtubular reactors. Chapter 2 explores the effect of electrode porosity and configuration on ohmic losses. Experimental work demonstrates that the conductivity of the electrode and the uniformity of the current distribution are crucial for minimizing area-specific resistance (ASR). Although coaxial configurations reduce areal resistance, they may lead to higher volumetric resistance (VSR), suggesting that a quasi-coaxial configuration may be better suited for multitubular flow batteries. Chapter 3 presents the development of an analytical model for tubular reactors, which highlights the impact of electrode geometry and material properties on current distribution, electrode utilization, and ASR scaling. The model identifies key dimensionless parameters that govern current distribution and provides a foundation for optimizing reactor design before more complex computational methods are employed. Chapter 4 focuses on enhancing the scalability of microtubular VRFBs through material selection, specifically introducing bare copper as a promising anode material. Copper's high conductivity, stability in vanadium electrolytes, and low cost make it a strong alternative to graphite, especially for larger-scale applications. Copper demonstrates superior performance and scalability compared to graphite-based anodes. In conclusion, this thesis advances the field of electrochemical reactor design by optimizing electrode

configurations, developing analytical tools, and selecting suitable materials for scalable microtubular VRFBs. The insights gained from this work contribute to the development of next-generation energy storage solutions, which are critical for the integration of renewable energy into power grids.

CHAPTER 1. INTRODUCTION

1.1 General Background

As climate change intensifies, it becomes crucial for the international community to accelerate the shift towards decarbonized solutions. Meeting this challenge requires innovative approaches across various sectors, and electrochemical technologies provide a promising path for significant emission reductions. These technologies are essential in a wide range of applications, from sustainable material production to advanced energy storage and conversion systems.^{1,2} Central to these technologies are electrochemical flow reactors, which play an important role in increasing the efficiency and scalability of energy solutions.^{3,4} Electrochemical flow reactors are used in various fields, including redox flow batteries, electrolyzers, fuel cells, organic and inorganic electrosynthesis, metal manufacturing, and environmental treatment processes.⁵⁻⁹ From traditional configurations like parallel plate reactors to more novel approaches, the diversity and potential of these reactors are key to bringing electrochemical technologies to the forefront of sustainable solutions.

1.2 Basics of Electrochemical Flow Reactors

Electrochemical flow reactors come in various configurations, and a universal categorization of these configurations is impractical. For the purposes of this thesis, we focus on two primary categories based on electrode shape: reactors with parallel plate electrodes and reactors with coaxial cylindrical electrodes (Figure 1.1a,b).⁴ These configurations can be further categorized as undivided reactors, when no separator is

included and there is only one electrolyte compartment, or divided reactors when a separator is included and two or more electrolyte compartments are created (Figure 1.1c,d). When a porous material is included, two flow configurations emerge: flow-by and flow-through. (Figure 1.1e,f) One last important distinction is the way individual reactors are electrically connected when an electrochemical system is scaled up. This gives rise to two main configurations: the monopolar configuration and the bipolar configuration (Figure 1.1g,h).¹⁰ The monopolar configuration maintains the same voltage for the system but adds the current of the individual reactors to obtain the total current of the system, while the bipolar configuration operates at the same current as the individual reactors but the system voltage is the sum of the voltages of each reactor.

Although this thesis focuses on these core configurations, it is worth noting that other important designs exist, such as trickle bed reactors, fluidized bed reactors, and rotating disk electrodes. These configurations have been extensively discussed in the literature, and the interested reader is encouraged to consult these resources (see references 11-14) for further details.¹¹⁻¹⁴

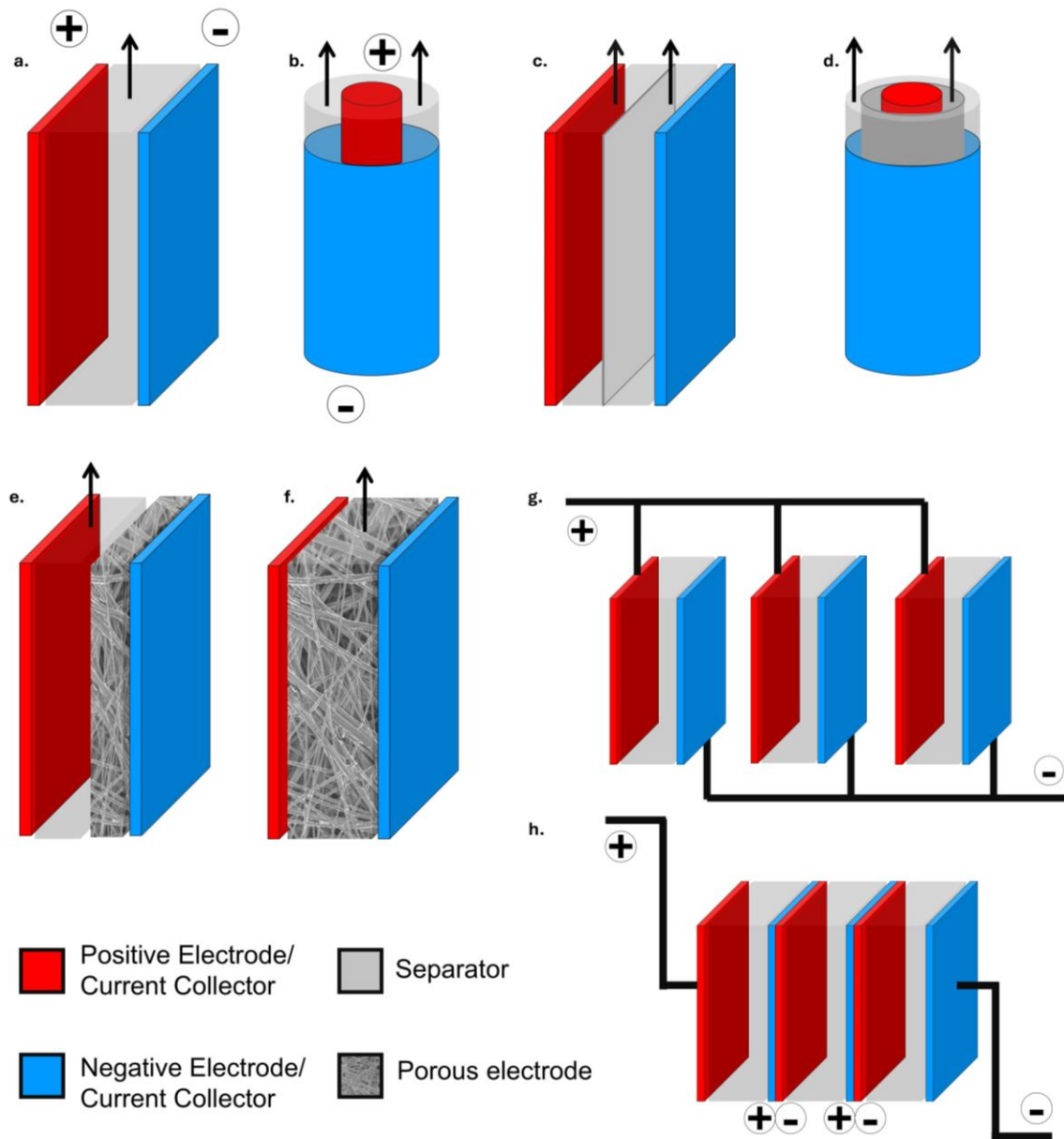


Figure 1.1 – a. Undivided parallel plate reactor configuration, b. Undivided coaxial electrode configuration, c. Divided parallel plate reactor configuration, d. Divided coaxial electrode configuration, e. Flow-by configuration, f. Flow-through configuration, g. Monopolar reactor connection, h. Bipolar reactor connection.

1.3 Tubular Flow Reactors

Among these reactor configurations, the parallel plate design stands out as the most versatile and extensively studied. However, despite its importance, this configuration has not been able to significantly reduce costs to achieve feasibility on a larger scale.^{6,15} Tubular reactors started receiving more attention as a possible alternative, due to their potential in achieving higher volumetric power density, in lowering sealing requirements and in decreasing the cost of manufacturing.¹⁶⁻¹⁹ The tubular configuration has been demonstrated in most electrochemical technologies. Tubular fuel cells were the first to be studied with several studies on hydrogen fuel cells, direct methanol fuel cell (DMFC), and solid oxide fuel cells (SOFC).²⁰⁻²² Recently, Ressel et al. developed an all-extruded tubular flow cell to be used in flow batteries and later in PEM electrolysis.^{18,19,23}

The most studied technologies that used the tubular configuration were fuel cells. These past efforts, however, faced several challenges. Power density, both areal and volumetric, proved to be lower for tubular hydrogen and solid oxide fuel cells due to typically higher ohmic losses.²⁴ Hydrogen fuel cells faced assembly and fabrication challenges, since creating a cylindrical membrane-electrode assembly (MEA) and gas diffusion layer (GDL) in a cylindrical geometry while achieving low resistance was not straightforward. The commercially available carbon fiber-based materials (cloth, carbon paper) could not be easily bent and inserted into or around the membrane, complicating the manufacturing process. Consequently, most research nowadays focuses on developing fabrication and assembly methods for air-breathing proton-exchange membrane fuel cells (PEMFCs) for portable power generation.^{22,25-29}

Tubular SOFCs have been partially commercialized, with systems demonstrated at power levels up to 1 kW.^{30,31} Their most significant advantages over their planar counterparts are the seal-less design and high-temperature stability.²¹ However, these tubular SOFCs face challenges related to low power density and manufacturing complexities that drive up costs. The tubular configuration requires longer current collection pathways, leading to higher ohmic losses compared to planar designs, which ultimately limits the power density. Additionally, thin-film deposition on curved surfaces necessitates complex manufacturing steps, further increasing production costs.³⁰ Microtubular SOFCs, with tube diameters of 1 mm or smaller, have demonstrated additional advantages over conventional tubular SOFCs. At this tube size, the packing efficiency increases significantly, improving the power density while maintaining the sealing and stability advantages.^{32,33} However, the challenges of current collection and manufacturing inherent in the tubular configuration also persist in the case of microtubular SOFCs.^{33,34}

Recently the first microtubular flow battery was introduced by Stolze et al., who emphasized the potential for a more compact design (Figure 1.2a).³⁵ Building on these ideas, Wu et al. introduced a bundled microtubular flow battery that deviated from the traditional coaxial configuration used in earlier tubular and microtubular designs (Figure 1.2b).¹⁶ Their approach leveraged the high packing efficiency of microtubular membranes to achieve very high membrane surface area per unit volume (m^2/m^3), resulting in increased volumetric power density (Figure 1.2c).

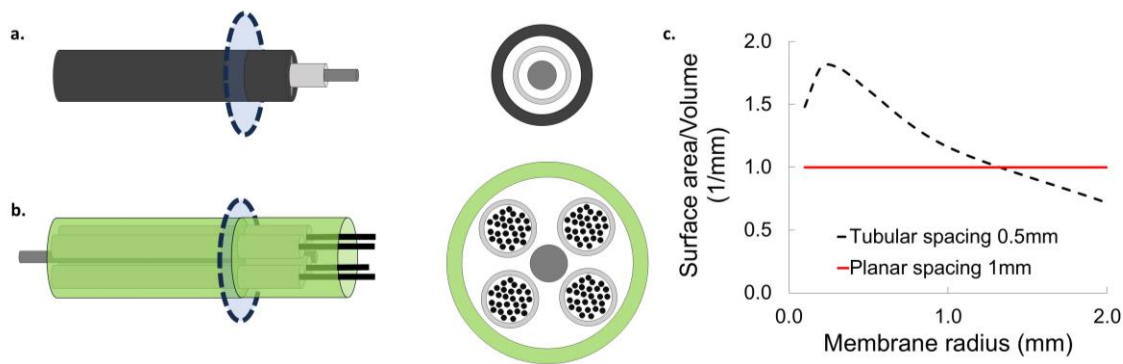


Figure 1.2 – a. Coaxial microtubular reactor, b. Non-coaxial bundled microtubular reactor, c. Surface area per unit volume of an array of tubular and planar membranes.

1.4 Redox Flow Batteries

Developed in Japan in the 1970s, the redox flow battery (RFB) is a technology where energy is stored in the form of oxidized or reduced species in an electrolyte solution.^{36,37} The RFB setup consists of two main parts: electrolyte reservoirs containing electroactive species and the power unit (reactor) where electrochemical reactions occur to generate power (Figure 1.3a). The electrolytes are constantly circulated from the tanks to the reactor and vice versa with the use of pumps. A conventional power unit of an RFB consists of a stack of parallel plate reactors. The individual parallel plate reactor of the stack contains two porous electrodes on the two sides of a separator (Figure 1.3b).³⁸ The electrodes are typically porous materials to provide high surface area for the reaction and the diffusion of the active species.³⁹

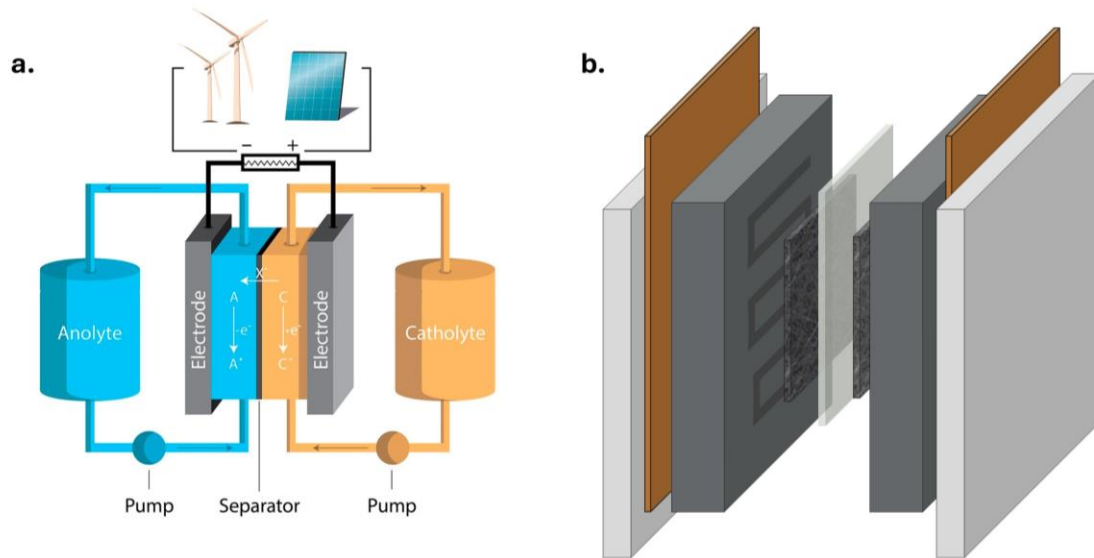


Figure 1.3 – a. Redox Flow Battery (RFB) schematic b. Power unit schematic.⁴⁰

1.5 Research Problem and Hypothesis

Energy storage systems (ESS) are critical for the integration of renewable energy sources, yet no ESS has fully met the DOE target of a storage cost below \$150/kWh.⁴¹ Depending on storage duration, different technologies are favored, with battery ESS expected to grow in the 4-8 hour range (Figure 1.4).⁴² Lithium-ion (Li-ion) batteries currently dominate the energy storage market due to their technological maturity, but they encounter significant challenges when scaled up for large-scale, long-duration storage.⁴³ In contrast, redox flow batteries offer key advantages, including easier scalability and independent adjustment of power and energy capacity, making them well-suited for grid storage.⁴⁴ However, Li-ion's closest competitor, the vanadium redox flow batteries (VRFBs), still face major cost challenges, particularly due to the high capital cost of the stack and the vanadium electrolyte.^{15,45}

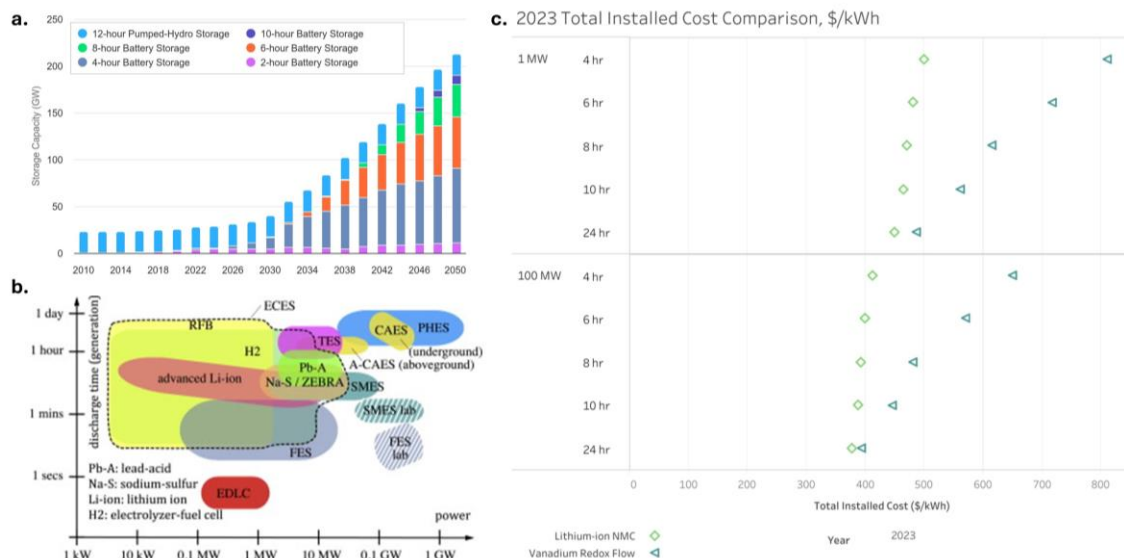


Figure 1.4 – a. U.S. storage capacity predictions, b. ESS grouped by power and discharge time, c. Total installed cost comparison between VRFBs and Li-ion NMC batteries.^{15,42,46}

This thesis investigates whether the microtubular configuration offers a promising alternative and whether its high packing efficiency can translate into performance gains and potential cost reductions. One key problem that tubular, including microtubular, reactors face is the higher resistance (ASR) compared to their parallel plate counterparts.^{18,35,47} Whether this is a feature that arises due to this tubular geometry, how it can be mitigated or compensated for by other advantages, and lastly how it would impact scalability are important questions to be answered to evaluate the potential of the microtubular configuration in the energy storage sector.

1.6 Significance and Contribution of the Study

The purpose of this study is to address existing challenges in electrochemical reactor design for flow battery applications. Specifically, a microtubular reactor is analyzed as a Vanadium Redox Flow Battery power unit. This research aims to introduce a new design to VRFB technology, which currently struggles with high capital costs. The proposed

microtubular design has not been thoroughly studied in the existing literature and remains at a proof-of-concept stage. Therefore, this work seeks to expand the current understanding of tubular reactor configurations in electrochemical engineering. More specifically:

- This research advances the knowledge of tubular electrochemical reactors by developing an analytical model that investigates the current distribution along the reactor length and resistance scaling with length. This model identifies key parameters and trends, providing a foundational understanding of the tubular configuration. It offers easy-to-apply analytical formulas and establishes a basis for future research on scalability, performance, and design improvements for tubular reactors.
- A comparative analysis of different electrode configurations in microtubular reactors is performed, offering insights into the performance advantages of each configuration. This understanding will help researchers and engineers focus their efforts on specific configurations based on desired performance metrics.
- A Cu anode is proposed as an alternative to traditional graphite-based electrodes in microtubular VRFBs, addressing existing challenges associated with these electrodes. This research explores its potential benefits in terms of electrochemical performance, scalability, and cost-effectiveness.

1.7 Thesis Outline

This thesis involves a systematic approach to evaluate, understand, and improve microtubular reactors for VRFBs. Combining experiments and modeling sheds light on

various aspects of microtubular reactors such as electrode configuration, materials, dimensions, and current distribution among others. More specifically:

- **Chapter 2 - Effect of Electrode Porosity and Configuration on Ohmic Losses of Tubular Flow Batteries:** This chapter investigates the impact of electrode porosity and configuration on the ohmic resistance of tubular flow batteries. The experimental work focuses on analyzing the contributions of different resistance components, such as electrode, electrolyte, and separator resistances. In addition, various electrode configurations are evaluated to identify design strategies that can minimize ohmic losses and improve scalability.
- **Chapter 3 - An Analytical Model for Tubular Flow Reactors:** Chapter 3 presents a mathematical approach to model a tubular flow reactor. This approach identifies key dimensionless parameters that determine the current distribution uniformity and reactor resistance. The model provides insights that can guide the optimization of reactor design for enhanced performance.
- **Chapter 4 - Enhanced Scalability in Microtubular Vanadium Flow Batteries via Copper Anodes:** Building on the model's findings, this chapter addresses scalability challenges in microtubular VRFBs by proposing the use of copper anodes to lower resistance and enhance scalability. The chapter details the material selection process, the electrochemical characterization, and the performance improvements achieved with copper anodes.

CHAPTER 2. EFFECT OF ELECTRODE POROSITY AND CONFIGURATION ON OHMIC LOSSES OF TUBULAR FLOW BATTERIES

2.1 Introduction

In this chapter the effect of electrode porosity and configuration is investigated. A microtubular flow battery is constructed following the design of Wu et al, modified to work with Vanadium chemistry. The microtubular VRFB is tested, and its performance evaluated in terms of its area-specific resistance (ASR) and polarization curve. The effect of the electrode porosity and the electrode configuration are investigated in a single-membrane flow battery. The electrode configuration is further studied for a multi-tubular flow battery. Specifically, the current distribution of coaxial (Cx) and a quasi-coaxial (Q-Cx) configuration are numerically solved to evaluate the uniformity and compare areal and volumetric performance of the different configurations.

2.2 Methods

2.2.1 Materials

The tubular flow batteries were assembled using microtubular membranes sourced from Perma Pure. The membranes had inner diameters (ID) of 2.17 mm with wall thicknesses of 254 μm . Graphite materials were obtained from Ohio Carbon Blank Inc. The graphite rods used in the experiments measured 1.5 mm in diameter and 20 cm in length. All graphite tubes had an outer diameter (OD) of 0.25 inches and inner diameters

(ID) of 0.185 inches. Graphitic carbon fibers, supplied by Toray Composites (Item #: T700SC-12K-50C), were heat-treated prior to use to carbonize the polymer sizing. The VRFB electrolyte was supplied by U.S. Vanadium, LLC in the form of $V^{3.5+}$ and charged to 50% state of charge (SOC).

2.2.2 *Flow Cells*

Each tubular flow battery was constructed using three polypropylene tee compression tube fittings (sized for 0.25-inch outer diameter tubing, McMaster-Carr). Fluorinated ethylene propylene (FEP) tubing with a 0.25-inch outer diameter (OD) from McMaster-Carr was used to contain the electrolyte within the flow cells. Graphite tubes served as the electrodes in the active section of the cell. J-B WELD Epoxy Adhesive (Grainger, Inc.) was applied as needed to ensure proper sealing. Teflon tape (Swagelok) was applied to the threads of the fittings for additional sealing. A schematic of the fabrication steps for a coaxial flow cells and a picture of the finished cell are shown in Figure 2.1. The electrolyte was circulated using a Masterflex L/S Standard Digital PTFE-Tubing Pump System supplied by Avantor.

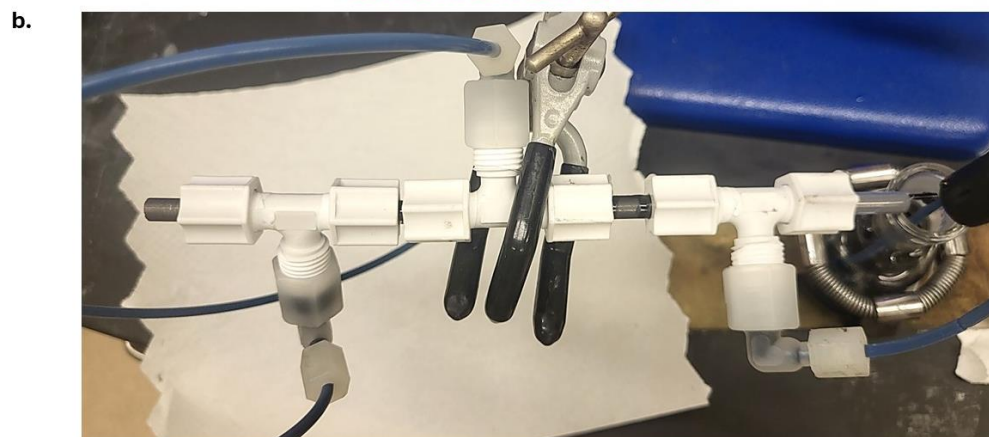
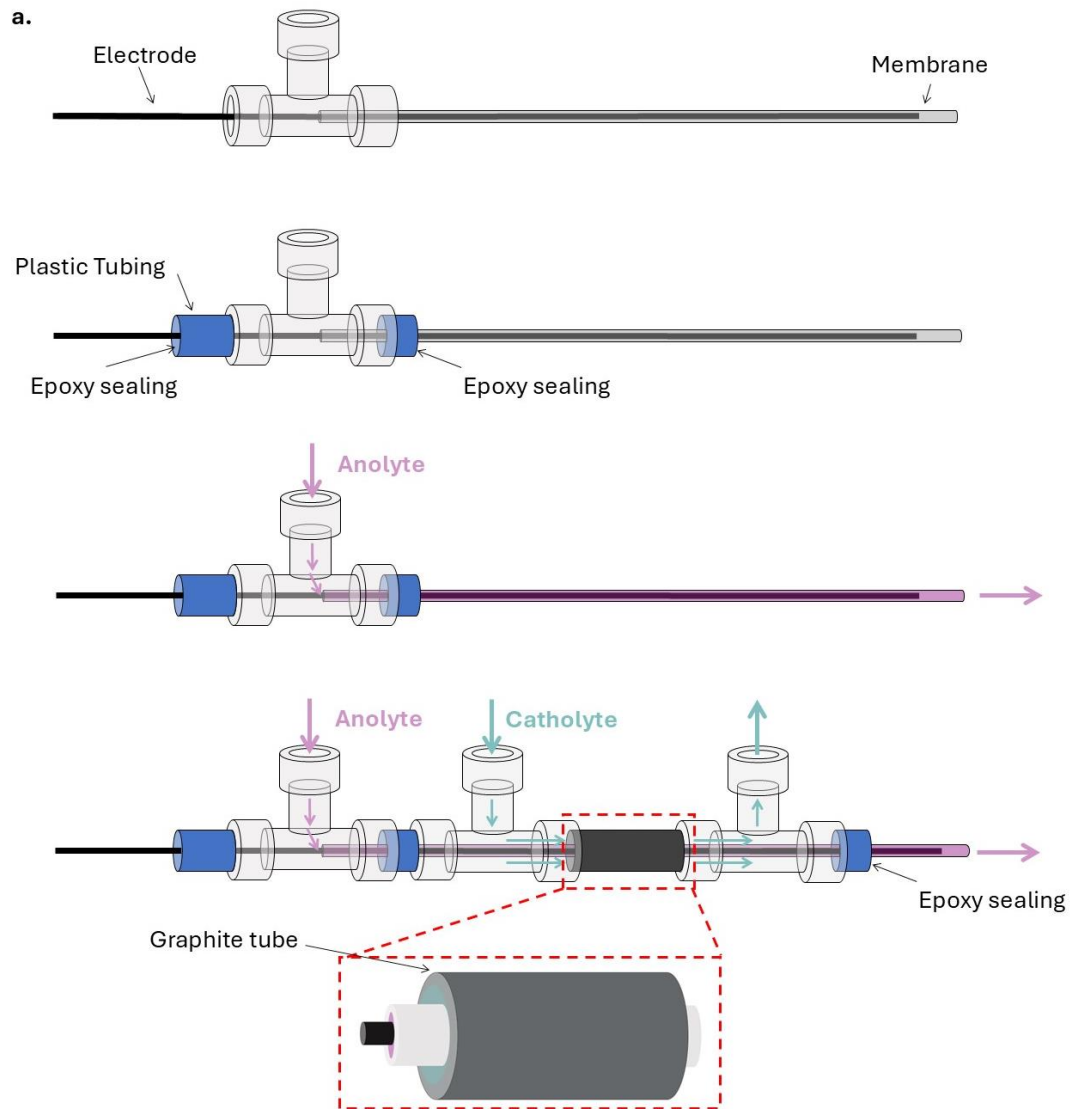


Figure 2.1 – a. Coaxial flow cell fabrication steps b. Picture of the coaxial flow cell

2.2.3 Electrochemical Characterization

Electrochemical testing was conducted using a Bio-Logic SP200 Potentiostat. Electrochemical Impedance Spectroscopy (EIS) was performed at open-circuit voltage (OCV) with a 10 mV voltage amplitude, over a frequency range from 200 kHz to 0.1 Hz. The ohmic losses were estimated by measuring the high-frequency x-intercept of the Nyquist plot, also referred to as High-Frequency Resistance (HFR). Polarization curves were generated using chronoamperometry. For each measurement, a voltage was applied for 1-2 minutes until the current stabilized, followed by holding at OCV for the same duration until the current approached zero. Each positive polarization voltage step was followed by a corresponding negative step to minimize variations in the electrolyte's state of charge (SOC). Voltage steps ranged from 10 mV to 20 mV, and the final current data points were used to construct the polarization curve.

2.2.4 Numerical Simulations

The Primary Current Distribution interface in COMSOL Multiphysics was used to model the current distribution in the electrolyte and the separator. This involves solving the Laplace equation for the potential in the electrolyte, and solid electrodes:

$$\nabla^2 \varphi_i = 0 \tag{1}$$

Where i equals 1,2, or s for the inner electrode, the outer electrode, and the electrolyte solution, respectively. The equation for the electrode-electrolyte interface is:

$$\varphi_i - \varphi_s = U_i \tag{2}$$

Where i is equal to 1 and 2 for the two electrodes and U is the equilibrium potential for the reaction at each electrode. Constant potential boundary conditions were applied at the center of the inner electrode, at the center of the outer electrode for the quasi-coaxial configuration, and at the OD of the outer tube for the non-coaxial configuration. The resistance estimation is based on the current response to a 50 mV applied voltage. The membrane properties used are those from Nafion as given in COMSOL's material library for fuel cells and electrolyzers.

2.3 Results and Discussion

2.3.1 Overview

The electrodes of the microtubular VRFB need to be selected so that they are compatible with Vanadium redox couples. Guided by literature studies on conventional VRFBs, graphite is a material with facile kinetics towards the reaction that the vanadium ions participate and is also chemically stable in these electrolytes.⁴⁸ In parallel plate vanadium flow battery cells, the most common electrodes are fibrous carbon-based electrodes such as carbon paper, carbon felt, and carbon cloth (Figure 2.2a).³⁹ None of these electrodes, however, are suitable for a microtubular reactor due to the size and shape of the membrane. Wu et al. proposed the use of carbon fiber bundles which satisfy most requirements for an VRFB electrode: fast kinetics towards the vanadium ions, high surface area, and adequate conductivity due to their graphitic structure (Figure 2.2b).¹⁶

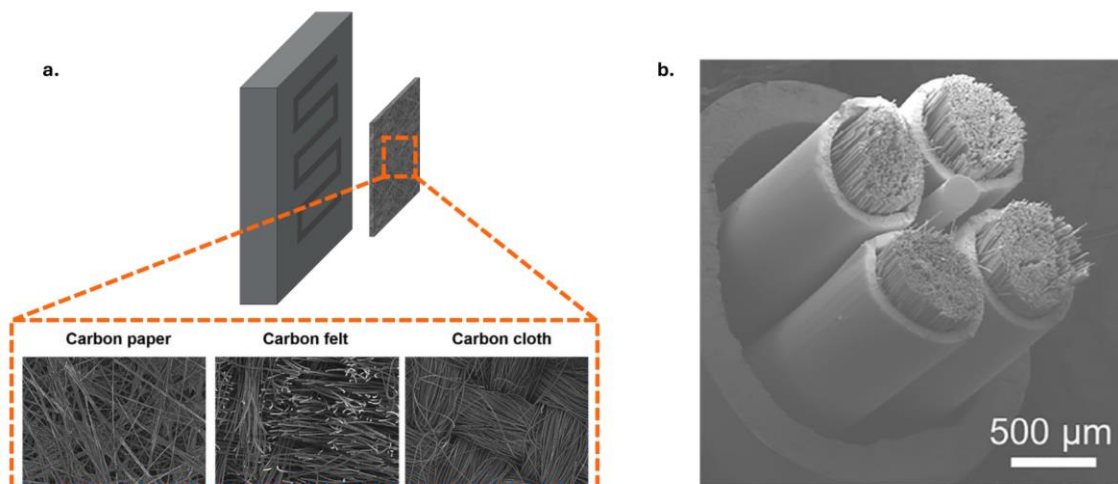


Figure 2.2 – a. Porous carbon fiber-based electrodes typically used in VRFBs, b. Carbon fiber bundle electrode used in ZnI_2 microtubular flow batteries.^{16,39}

2.3.2 Preliminary Results

The preliminary tests aimed to evaluate the performance of the microtubular reactor using the simplest possible design with a single membrane. The initial assessment was conducted on a flow battery utilizing carbon fiber bundles for both electrodes. A schematic of the reactive zone in this battery is depicted in Figure 2.3a. The electrochemical impedance spectroscopy (EIS) spectra and the corresponding polarization curve are shown in Figure 2.3b and Figure 2.3c, respectively.

The High-Frequency Resistance (HFR), which reflects the ohmic resistance of the flow cell, was measured to be $15 \Omega \cdot \text{cm}^2$. From the polarization curve (Figure 2.3c), the maximum discharge current density reached $5 \text{ mA} \cdot \text{cm}^{-2}$, while the maximum charge current density was $6 \text{ mA} \cdot \text{cm}^{-2}$. This preliminary evaluation revealed significantly lower current densities compared to parallel-plate reactors, with ohmic losses appearing as the

primary limiting factor. These results highlight the need for a more detailed analysis of the sources of ohmic resistance in this configuration to better understand and reduce resistive losses.

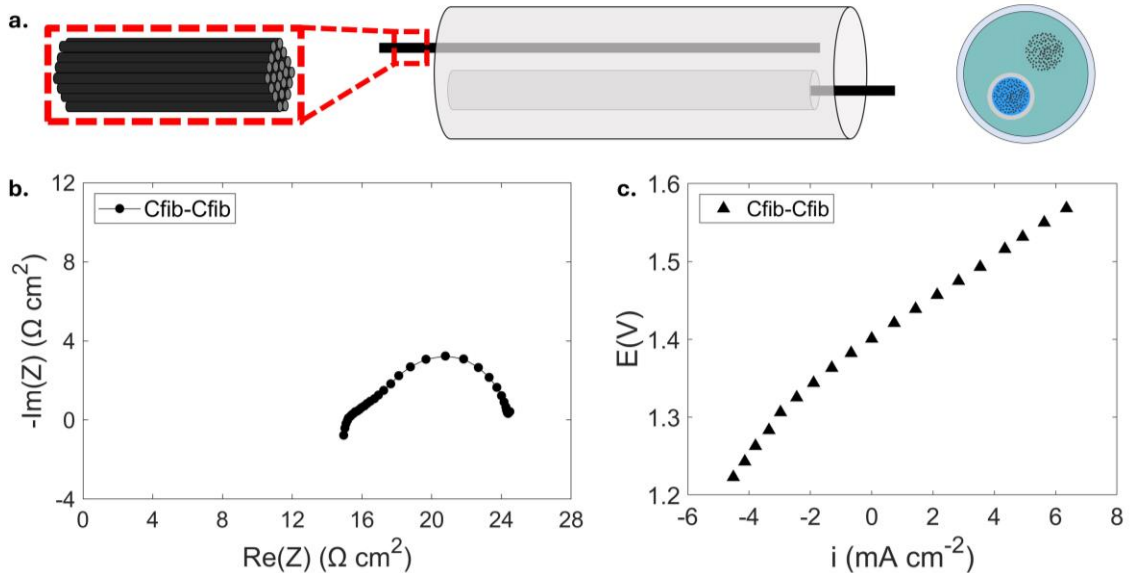


Figure 2.3 – a. Schematic of the microtubular carbon VRFB with carbon fiber electrodes, b. EIS spectrum and c. polarization curve of the carbon fiber-based VRFB. The flowrates of the inner and outer flow channels were 5 mL min^{-1} and 15 mL min^{-1} respectively.

2.3.3 Ohmic Resistance Analysis

Electrons travel along the electrodes, participate in charge transfer reactions at the electrode surface, and pass through the electrolyte and separator. The overall ohmic resistance, measured through the high-frequency resistance (HFR), arises from contributions by the electrodes, separator, and electrolyte (Figure 2.4). The electrode resistance is influenced by the material's resistivity, the cross-sectional area, and the length of the electrode based on the following formula:

$$R_{electrode} = \rho \frac{L}{A} \quad (3)$$

This formula holds when the current density across the cross section is uniform, which is a good approximation for long and thin electrodes. In the case of the electrolyte and the separator in this tubular geometry, the current density may not be uniform and such an analytical formula cannot be used. In this case, a numerical solution of Laplace's equation is required to estimate this resistance (Figure 2.4).⁴⁹

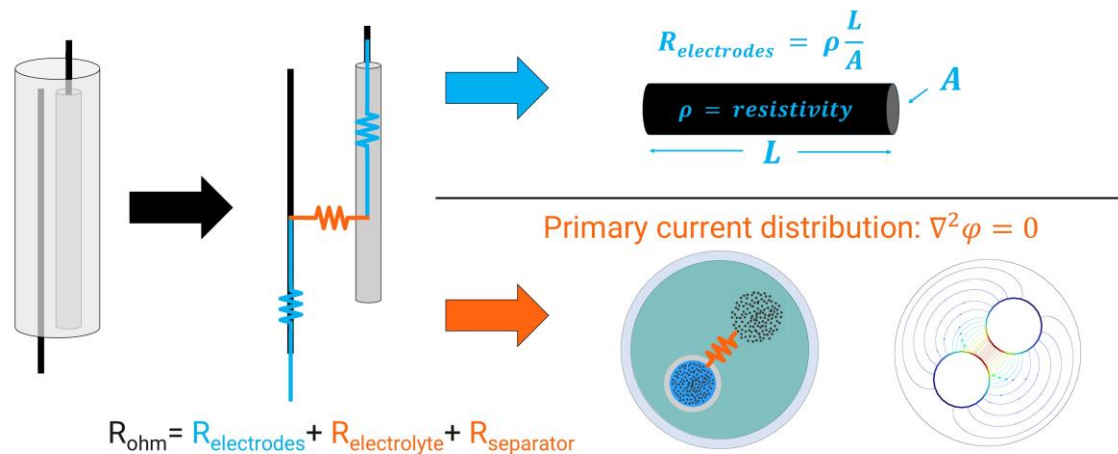


Figure 2.4 – The components of the ohmic resistance in a tubular flow battery showing the solid phase resistance from the electrode and the ionic resistance of the electrolyte and the separator.

2.3.4 Electrode Resistance

The electrode resistance can be adjusted by altering the material or the dimensions of the electrode, specifically its cross-sectional area or length. In VRFBs, the high acidity of the electrolyte limits the choice of materials, as only a few have proven stable in both the anolyte and catholyte. For this reason, we focus on graphite-based materials.

One way to evaluate the impact of electrode resistance while using the same material is by varying the cross-sectional area. Carbon fiber-based electrodes have a much smaller cross-sectional area compared to solid graphite rods of the same dimensions. The total cross-sectional area of a carbon fiber bundle can be estimated by considering the fiber diameter (7 μm) and the number of fibers per bundle (12,000). Based on these values, the graphite rod has approximately four times the cross-sectional area. Since the resistivity of both materials is comparable, this should result in a fourfold reduction in ohmic resistance due to the electrode alone.

In Figure 2.5 the HFR decreases from 15 $\Omega \text{ cm}^2$ to 6.4 $\Omega \text{ cm}^2$ when switching from carbon fibers to graphite rods. Similarly, the slope of the polarization curve in the linear region is reduced for the graphite rod-based flow battery indicating lower ohmic resistance (Figure 2.5). These results reveal the important role that electrode resistance plays in the microtubular flow battery performance.

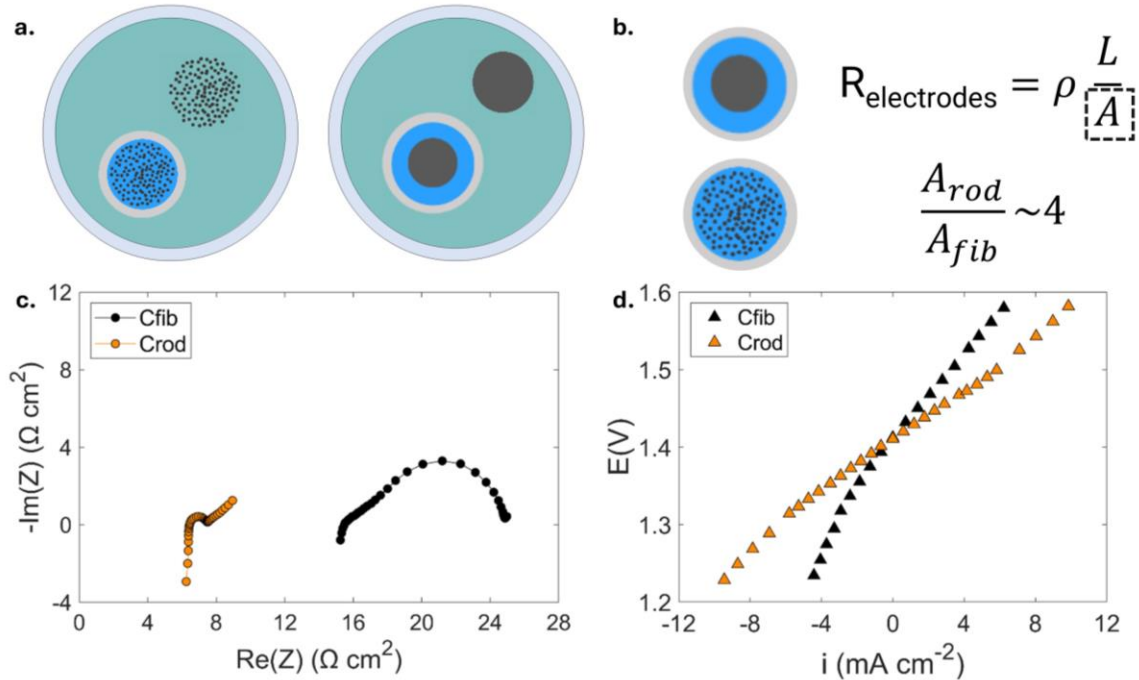


Figure 2.5 – a. Schematic of a flow battery with carbon fiber and carbon rod-based electrodes, b. Cross-section are comparison, c. EIS spectra and d. polarization curves of the two VRFBs. The flowrates of the inner and outer flow channels were 5 mL min^{-1} and 15 mL min^{-1} respectively.

2.3.5 Electrolyte and Separator Resistance

Our hypothesis in this analysis is that the electrode configuration dictates the current distribution in the electrolyte and the separator and, therefore, their contribution to the resistance. A non-uniform current distribution forces parts of the electrode to operate at different current densities, which may lead to poor utilization of the available surface area. We expect that this non-uniformity will manifest through an increased ohmic resistance. The question that remains to be answered is how significant this increase is. To test the hypothesis, we compare the ASR of a coaxial and a non-coaxial flow battery. While the membrane and the inner electrode are the same, the outer electrode is a graphite tube in the coaxial battery and a graphite rod in the quasi-coaxial battery. (Figure 2.6a,b)

In Figure 2.6 we demonstrate the effect of the configuration on the ohmic losses and the current distribution in a tubular flow battery. We compare the EIS spectra we experimentally collected for two tubular flow battery configurations, coaxial(Cx) and non-coaxial (N-Cx). (Figure 2.6c) The ASR_{HFR} , obtained from the High Frequency Resistance (HFR) in the EIS plot is compared, showing that the quasi-coaxial configuration has almost twice the ASR_{HFR} as the coaxial. (Figure 2.6e) This difference is attributed to the non-uniformity of the current distribution. To validate this hypothesis, we numerically solve for the primary current distribution using COMSOL. The primary current distribution assumes infinitely fast kinetics on the electrode surface, electroneutrality in the electrolyte and homogeneous electrolyte. Therefore, the current response to an applied overpotential depends solely on the ohmic resistance of the solution and the separator. The simulations show lower ohmic losses for the coaxial configuration, following the same trend as the experiments.(Figure 2.6e)The current density distribution in the electrolyte seems localized in the area where the two electrodes are facing each other and the distance between them is at its minimum. (Figure 2.6d) This leaves the rest of the electrode surface experiencing low current densities and being poorly utilized. This comparison demonstrated the importance of the electrode configuration on the resistive losses in a tubular flow battery.

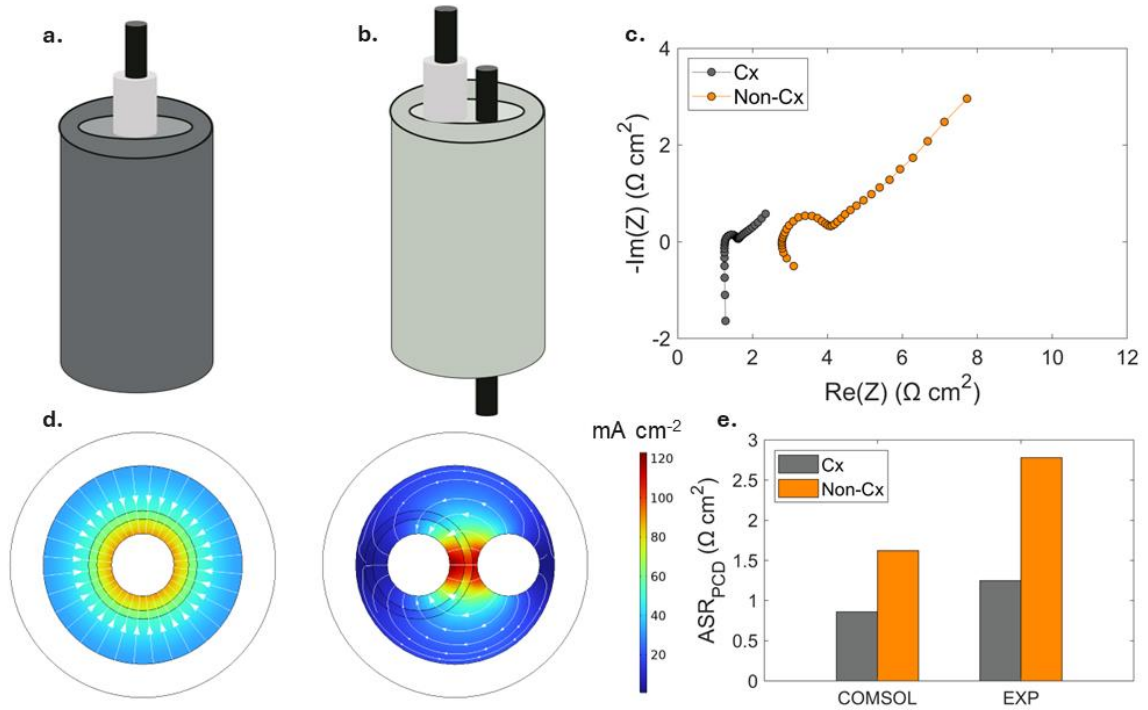


Figure 2.6 - a. Schematic of the co-axial configuration b. Schematic of the non-coaxial configuration with one outer electrode c. EIS of the co-axial and non-coaxial configuration d. Primary current distribution of the two configurations obtained in COMSOL e. ASR measured based on COMSOL's primary current distribution solution and the HFR obtained from EIS experimentally. The flowrates of the inner and outer flow channels were 10 mL min^{-1} and 25 mL min^{-1} respectively.

Table 2.1 – Parameters of the coaxial and non-coaxial flow cells used in the experiments and the simulations.⁵⁰

Parameter	Value	Units	Description
r_1	0.75	mm	Inner electrode radius of both Cx and NCx
$r_{2,Cx}$	2.35	mm	ID of the graphite tube of Cx
$d_{2,Cx}$	0.825	mm	Thickness of the graphite tube of Cx
$r_{2,QCx}$	0.75	mm	Outer electrode radius of N-Cx
r_m	1.09	mm	Membrane radius (from supplier)
w	250	um	Membrane thickness (from supplier)
κ_{el}	0.2	S cm^{-1}	Electrolyte conductivity
ρ	1.22	$\text{m}\Omega \text{ cm}$	Graphite conductivity (from supplier)

2.3.6 *Evaluation of Electrode Configurations*

We showed that the electrode configuration has an important effect on the current distribution and, as a result, on the ohmic resistance of the tubular flow battery. At first glance, it seems logical to choose a coaxial configuration over a less symmetric non-coaxial configuration. This would indeed be wise if our focus is on designing a tubular flow battery with a single membrane and scaling up only in length. On the other hand, if the goal is scaling up from a single membrane to a multi-tubular flow battery, the optimal configuration is less clear.

As pointed out by Wu et al., microtubular membranes can be densely packed and significantly decrease the size of the flow battery.¹⁶ However, the choice of the electrode configuration may affect the ability of the membranes to achieve high packing efficiency. For instance, a coaxial configuration may not allow the membranes to be tightly packed due to the existence of the outer tubular electrode. In contrast, a quasi-coaxial configuration with rods or wires as outer electrodes could allow for a higher density packing of the membranes. In order to assess these different configurations in a way that the packing efficiency is also accounted for, we propose the use of a Volume Specific Resistance (VSR) in addition to the conventional ASR. This idea of normalizing resistance by volume was introduced by Stolze et al. as a complementary metric for assessing the performance of tubular flow batteries.³⁵

To shed light on this trade-off, we compared a coaxial configuration with a quasi-coaxial configuration. These two configurations and their unit cells, respectively, are shown in Figure 2.7a,b. The current density distributions of the two configurations were

compared, followed by the comparison of their areal and volumetric resistances. To make the comparison as consistent as possible, we used the same size and thickness for the membrane, same size for the inner electrode, and same thickness of the outer electrode in the two configurations.

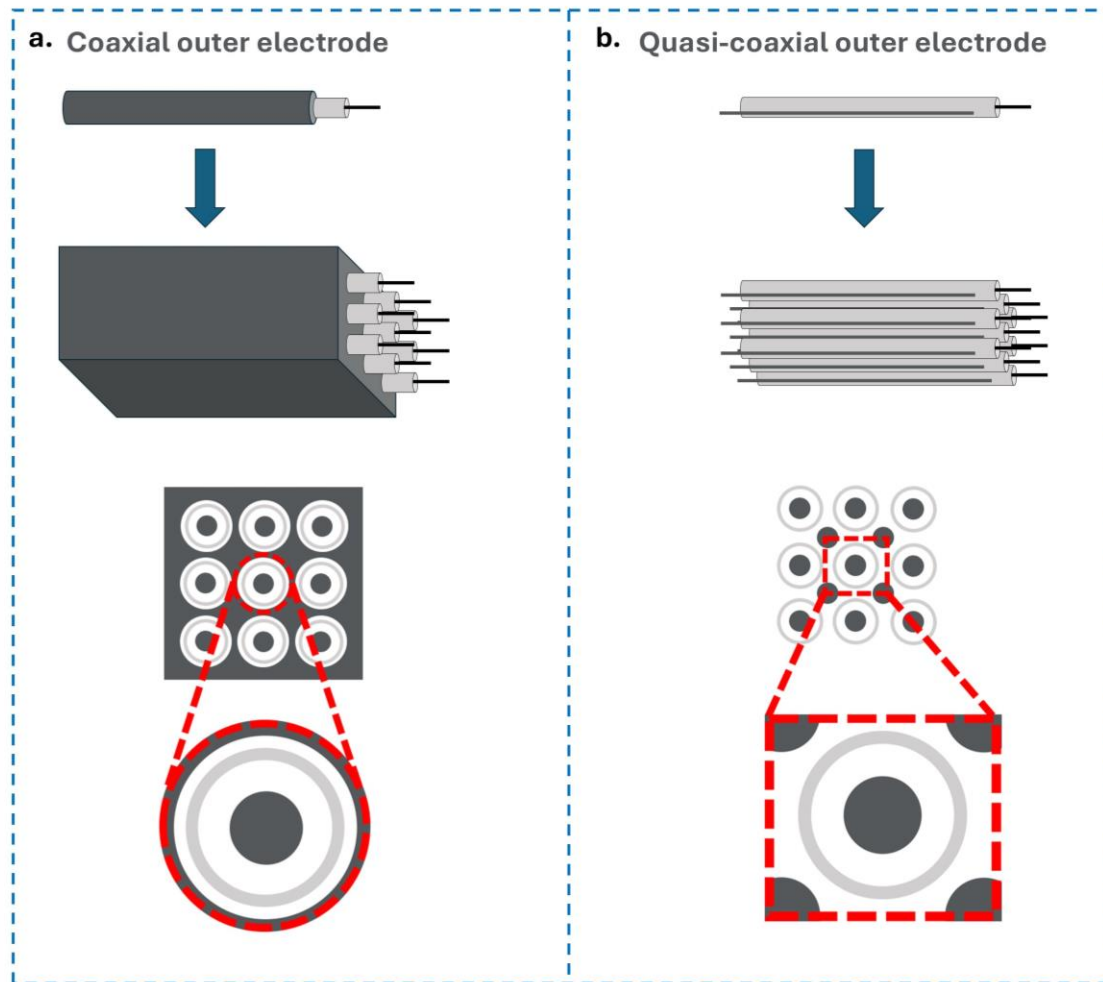


Figure 2.7 – a. A scaled-up coaxial configuration with a honeycomb-structured outer electrode, b. A scaled-up quasi-coaxial configuration with wire/rod-shaped outer electrodes

The quasi-coaxial configuration is expected to experience non-uniformities in the current distribution compared to the coaxial configuration but at the same time maintain a higher packing efficiency than the coaxial. Initially, we compared the current density

distribution of the two configurations. The geometric parameters used in this simulation are shown in Table 2.2 combined with electrode and electrolyte conductivities from Table 2.1. The coaxial configuration showed a uniform current distribution, with the current density slightly decreasing in the radial direction due to an increase in the normal to the current vector area (Figure 2.8a). In the quasi-coaxial configuration the current density was localized where the distance between the electrodes minimizes, following the path of least resistance (Figure 2.8b). These patterns were also confirmed in Figure 2.8c where the current density magnitude at the membrane is plotted against the polar angle. The current density peaks at 45 °, 135 °, 225 °, and 315 ° where the distance between the electrodes is minimized. On the other hand, the coaxial's current density is constant and higher than the quasi-coaxial indicating a lower ASR. Regarding the extent of the non-uniformities of the quasi-coaxial, the current density fluctuates between approximately 75% and 125% of the average current density (Figure 2.8d).

Table 2.2 – Parameters used in the COMSOL simulations to evaluate current density distribution, ASR, and VSR.

Parameter	Value	Units	Description
r_1	0.75	mm	Inner electrode radius of both Cx and NCx
r_m	1.00	mm	Membrane radius
w	50	um	Membrane thickness ⁵¹
d_1	0.25	mm	Defined in Figure 2.9a,b
d_2	0.25	mm	Defined in Figure 2.9c,d

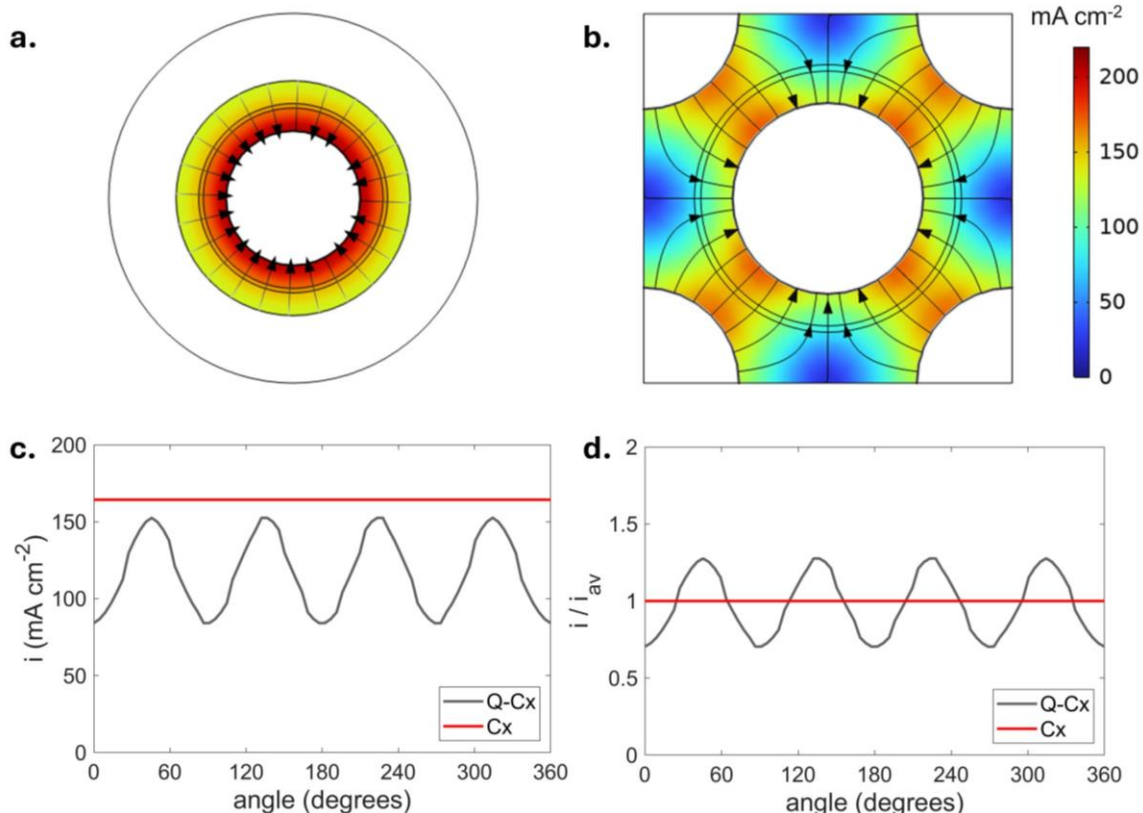


Figure 2.8 – a. Current density distribution for the coaxial configuration b. Current density distribution for the quasi-coaxial configuration, c. The current density distribution at the inner surface of the membrane as it changes with the polar angle d. The current density distribution over the average current density at the inner surface of the membrane as it changes with the polar angle.

For the resistance comparison, we varied the outer electrode distance from the membrane (d_1 in Figure 2.9a,b) and the outer electrode thickness (d_2 in Figure 2.9c,d) to reveal potential trends that relate to the dimensions. The inner electrode remained fixed at 0.75 mm radius since this is the minimum that can be produced consistently and with a low risk of breaking after consulting with our supplier (Table 2.2). In Figure 2.9e we showed that the coaxial configuration is expected to have lower ASR than the quasi-coaxial configuration regardless of the gap between the membrane and the outer electrode. We also observed that the bigger the outer electrode gap the higher the ASR for both configurations,

which can be explained by the increased path the ions have to travel in the electrolyte. (Figure 2.9e) When we measured the volumetric performance through the VSR, we noticed that the quasi-coaxial configuration shows lower resistance (Figure 2.9g). This means that the improved packing efficiency of the quasi-coaxial configuration can compensate for the higher ASR. This ASR difference was maintained across all outer electrode gaps and became more pronounced as the outer electrode thickness decreased (Figure 2.9f). Notably when the outer electrode thickness decreased, the trends changed and the VSR of the quasi-coaxial stopped decreasing. (Figure 2.9h). This behavior can be explained by the fact that when the outer electrode becomes particularly small, the volume of the unit cell will now be limited by the membrane size and the distance d_1 . Overall, this comparison showed that depending on the ease of manufacturing of the two electrode types, the minimum thickness possible, and the cost of production, cells of lower areal or lower volumetric performance may be pursued.

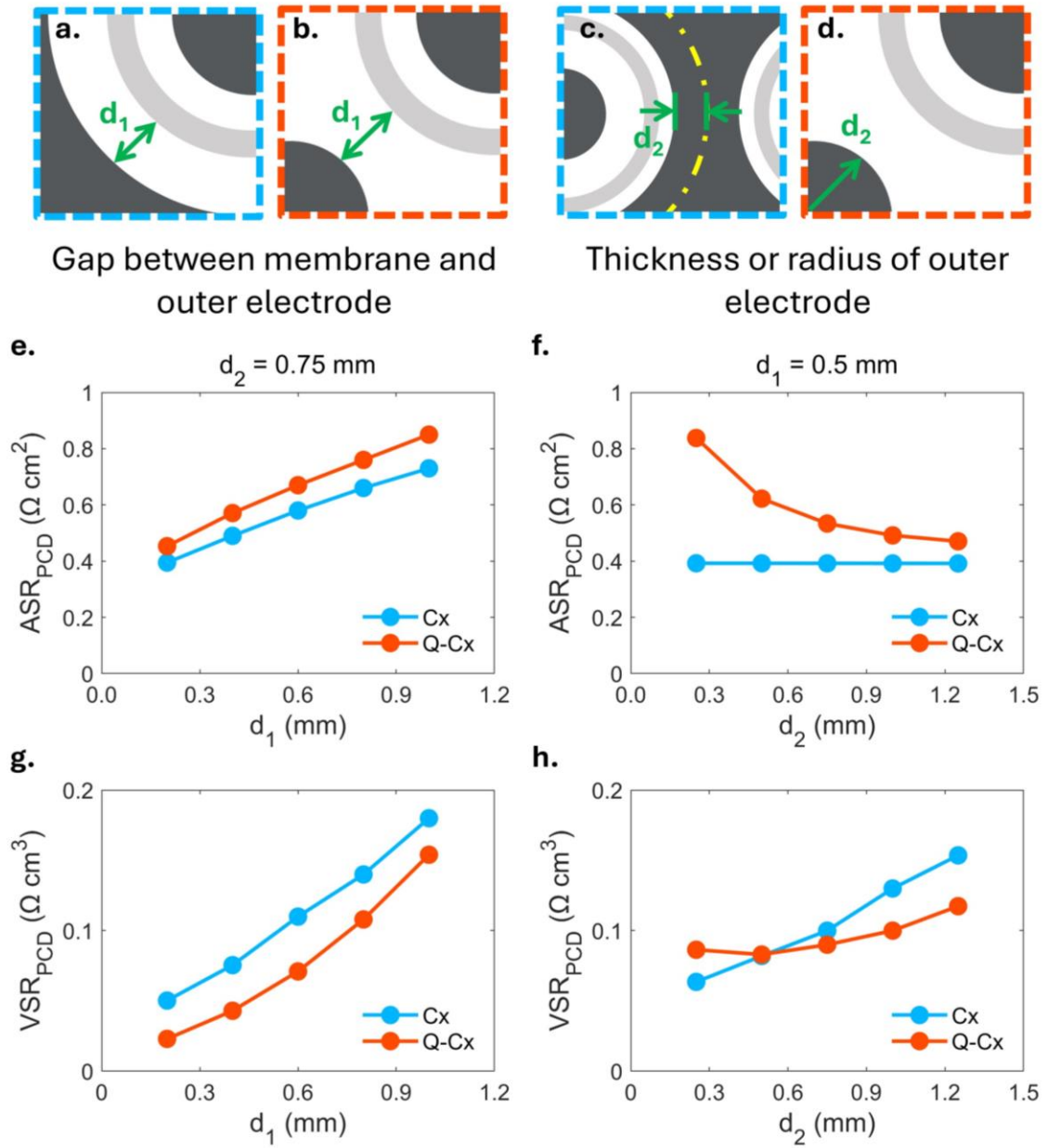


Figure 2.9 – Schematic of the a. gap between the membrane and the outer coaxial tubular electrode, b. gap between the membrane and the outer rod-shaped electrode, c. half the thickness of the outer honeycombed-shaped electrode in the coaxial configuration, d. the radius of the outer rod-shaped electrode in the quasi-coaxial configuration. The variation of the ASR and the VSR as estimated from the primary current distribution simulation versus, e., g. the gap between the outer electrode and the membrane, f., h. half the thickness of the outer electrode.

2.3.7 Scalability

After investigating the scalability of moving from a single reactor to multiple parallel reactors, we evaluated the scalability of increasing the active length of the flow battery. Extending the battery length was expected to proportionally increase the power output. To test this hypothesis, two flow batteries were fabricated with active lengths of 5 cm and 10 cm, and their polarization curves were collected (Figure 2.10a,b). We expected the 10 cm battery to deliver double the current at the same applied voltage. However, the current increased only slightly, resulting in a lower current density (Figure 2.10c). This limited increase was due to a higher ASR in the longer battery, as shown by the EIS (Figure 2.10d,e). The rise in resistance with length raised concerns about the scalability of this configuration, prompting further investigation into the effects of electrode resistance and tubular geometry on performance.

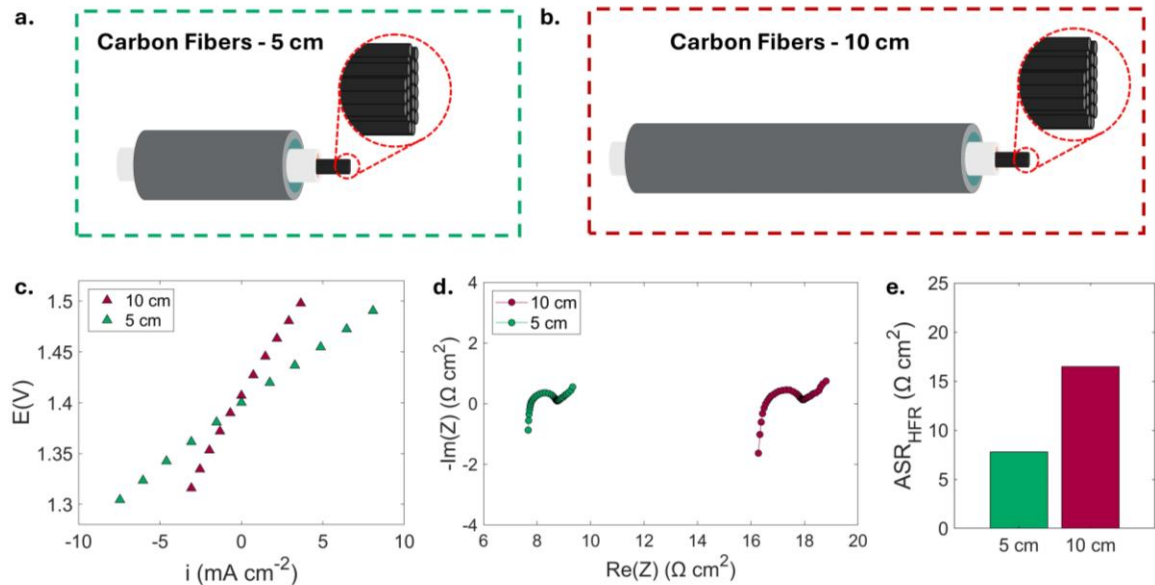


Figure 2.10 – Schematics of the a. 5cm active length battery, b. 10 cm active length battery. c. Polarization curve comparison, d. EIS spectra comparison, e. HFR comparison. The

flowrates of the inner and outer flow channels were 5 mL min^{-1} and 15 mL min^{-1} respectively.

2.4 Conclusions

A preliminary assessment showed that the performance of microtubular VRFBs suffers due to high ohmic resistance. Ohmic losses from the electrode, electrolyte, and separator contributed significantly to the total ASR. Varying the conductivity of the electrode changed the ASR by $10 \text{ } \Omega \cdot \text{cm}^2$, highlighting the importance of electrode conductivity. The electrode configuration in a single-tubular battery was also evaluated. A coaxial configuration resulted in a uniform current distribution and minimized ohmic losses in both the electrolyte and the separator, leading to a lower ASR. The electrode configuration was further examined in the case of a multi-tubular flow battery. When comparing the quasi-coaxial and coaxial configurations, it was found that while the coaxial configuration achieved a lower ASR, this did not necessarily translate into better volumetric performance (VSR). This demonstrates that high areal performance does not always align with high volumetric efficiency.

CHAPTER 3. AN ANALYTICAL MODEL FOR TUBULAR FLOW REACTORS

3.1 Introduction

CHAPTER 2 preliminary results on a microtubular flow battery demonstrated the crucial role that the electrode resistance plays in the ASR of the flow battery. In Section 2.3.7 an attempt to scale-up the battery revealed that the ASR increased when the flow battery length increased. These observations imply that there may be more complex phenomena occurring in the tubular geometry which affect its performance in ways that have not been observed before.

In this chapter we focus on understanding these phenomena, how they affect the performance of tubular reactors and what parameters influence them. Mathematical modeling is a very useful tool in this direction. Models are solved either analytically or numerically. Numerical solutions are typically obtained by solving the coupled momentum, mass transport, and electrochemical equations for specified conditions while analytical solutions focus on capturing trends and key variables that govern the behavior of the electrochemical reactors.⁵²⁻⁵⁵ To our knowledge, there are few comprehensive efforts to model the tubular reactor in the open literature.⁵⁶⁻⁵⁸ Most research has been conducted in the tubular fuel cell field where numerical simulations are used to study the effects of mass transport, pressure, and operating conditions.⁵⁹⁻⁶¹ Little to no attention, however, has been paid to the current distribution and the resistance of tubular reactors.⁶² A model that

studies the effect of the geometry and material properties on the behavior of the reactor would be highly useful for tubular reactor design and potential towards scaling-up.

Here we introduce an analytical model tailored for tubular flow reactors. This theoretical approach allows us to visualize and understand the effects of reactor design parameters and material selection on the performance of the reactor. The performance is evaluated based on the current distribution, potential distribution, and reactor resistance. The input parameters used in the analysis can be obtained either from the literature or routine experiments. The model shows that the current distribution along the reactor is determined by the ratio of the ohmic resistance of the electrodes and the radial resistances due to charge transfer on the electrodes, and ohmic resistance of the electrolyte and separator. High ohmic resistance in the electrodes results in uneven current distributions and poor reactor utilization. In addition, high resistance can also cap the maximum length of the reactor, which in turn limits the maximum power rating of the unit. By understanding these relationships, our model offers valuable insights for improving reactor designs and achieving higher power outputs.

3.2 Model Development

The key difference between the parallel plate reactor and the tubular reactor is the path that the electrons need to follow to participate in reactions. In the parallel plate reactor, whether in monopolar or bipolar configuration, the electrons need to cross the graphite, composite, or metal plate to reach the electrode and participate in the charge transfer reaction (Figure 3.1a). In the case of the monopolar configuration, the electrons need to flow along the length of the current collector or the monopolar plate itself if it is made of

metal, but in either case the resistance is significantly lower than that of graphite or composite materials. Overall, no significant non-uniformities are expected to appear due to the ohmic resistance of the plates or current collectors for the parallel plate reactor. On the contrary, in the case of the tubular reactor, the electrons need to travel along the length of the electrode and react at different distances from the current collector (Figure 3.1b). As a result, the electrons reacting close to the current collector will encounter less ohmic resistance than the electrons that react further from it.

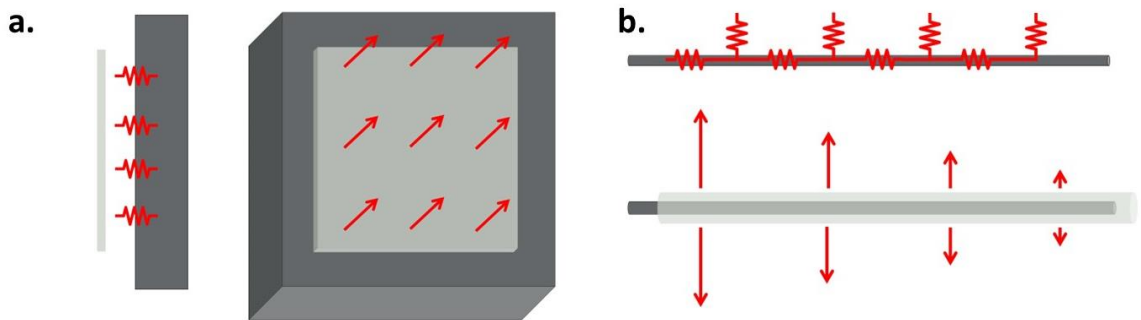


Figure 3.1 - Qualitative current distribution a) throughout the separator of the parallel plate reactor b) along the separator of the tubular reactor.

To carefully examine these phenomena, we created a mathematical model for the full tubular reactor. A schematic is shown in Figure 3.2a. The reactor consists of an inner cylindrical electrode, a tubular separator surrounding the inner electrode and an outer tubular electrode (Figure 3.2a,b). The two electrodes are in contact with current collectors at the two ends of the reactor (Figure 3.2b). The current collectors are assumed to have infinite conductivity and therefore uniform potential.

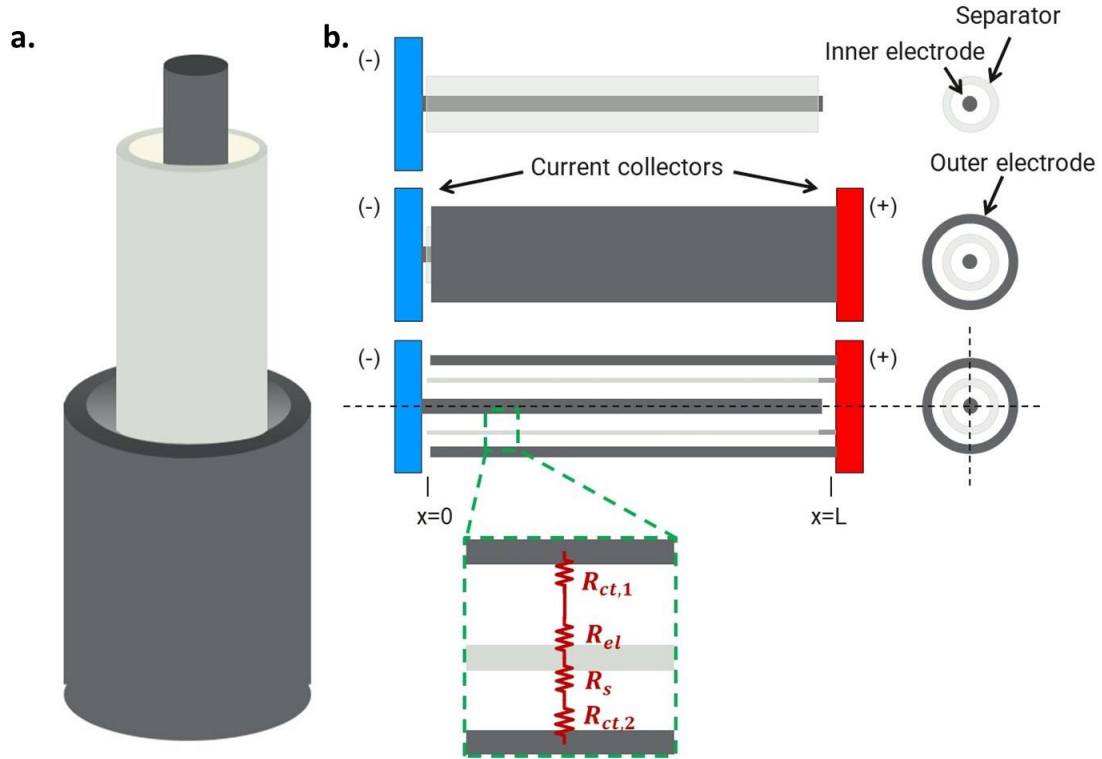


Figure 3.2 - a) Schematic of a tubular reactor. b) Tubular reactor model geometry.

This approach resembles Newman and Tobias's method for porous electrode, treating the inner electrode of the tubular reactor as the solid phase of the porous electrode and the outer electrode as the electrolyte.⁶³ To build the model for the tubular reactor, we start from the charge balance in the inner electrode:^{49,64}

$$\nabla \cdot i_1 = -a_1 i_{n,1} \quad (4)$$

Where i_1 is the current density in the inner electrode, $i_{n,1}$ the current density due to the reaction, and a_1 the specific interfacial area of the inner electrode. For the inner cylindrical electrode, the specific interfacial area is defined as:

$$a_1 = \frac{\text{electrode surface area}}{\text{electrode volume}} = \frac{2\pi r_1}{\pi r_1^2} \quad (5)$$

The current in the solid phase of the two electrodes is assumed to vary only in the x -direction and be uniform on the cross section. In the tubular reactor, it is more convenient to use the total current in the electrode than the current density across the cross-section of the solid electrode. Therefore, assuming one-dimensional current distribution, Eq. (4) is simplified to:

$$\frac{dI_1}{dx} = -2\pi r_1 i_{n,1} \quad (6)$$

To solve for the current distribution, a polarization equation needs to be used to express the current density due to the reaction. Butler-Volmer's equation is the most common choice to relate the reaction rate with the potential difference between the electrode and the solution:

$$i_{n,1} = i_{0,1} \left(e^{\frac{\alpha_{a,1}F}{RT}(\varphi_1 - \varphi_{1,s} - U_1)} - e^{-\frac{\alpha_{c,1}F}{RT}(\varphi_1 - \varphi_{1,s} - U_1)} \right) \quad (7)$$

3.2.1 Linear Kinetics Formulation

At low polarization, linear kinetics is a good approximation and leads to the following equation:

$$\frac{dI_1}{dx} = -2\pi r_1 i_{0,1} \frac{(\alpha_{a,1} + \alpha_{c,1})F}{RT} (\varphi_1 - \varphi_{1,s} - U_1) \quad (8)$$

Using the definition of the charge transfer resistance, Eq. (5) can be rewritten:

$$\frac{dI_1}{dx} = -\frac{2\pi r_1}{R_{ct1}}(\varphi_1 - \varphi_{1,s} - U_1) \quad (9)$$

Where R_{ct1} is the charge transfer resistance of the inner electrode reaction and defined as follows:⁴⁹

$$R_{ct1} = \frac{RT}{i_{0,1}(\alpha_{a,1} + \alpha_{c,1})F} \quad (10)$$

To eliminate the potential in the liquid phase, $\varphi_{1,s}$, which is a quantity that cannot be measured, we use the principle of the voltage divider as it is used in heat transfer phenomena in cylindrical geometries.⁶⁵ A cross section of the tubular reactor is shown in Figure 3.3, to explain how the principle is applied in the tubular reactor context. In this simplified version, we use the charge balance at the interfaces and the electrolyte to eliminate the intermediate potentials:

$$i_{n,1}(2\pi r_1) = i_{1,s}(2\pi r_1) = i_s(2\pi r_s) = i_{2,s}(2\pi r_{2,l}) = i_{n,2}(2\pi r_{2,l}) \quad (11)$$

$$\begin{aligned} \frac{\varphi_1 - \varphi_{1,s}}{R_{ct1}}(2\pi r_1) &= \frac{\varphi_{1,s} - \varphi_{1,sp}}{R_{el1}^l} = \frac{\varphi_{1,sp} - \varphi_{2,sp}}{R_s^l} = \frac{\varphi_{2,sp} - \varphi_{2,s}}{R_{el2}^l} \\ &= \frac{\varphi_{2,s} - \varphi_2}{R_{ct2}}(2\pi r_{2,l}) = \frac{\varphi_1 - \varphi_2}{R_{ct1}^l + R_{el1}^l + R_s^l + R_{el2}^l + R_{ct2}^l} \end{aligned} \quad (12)$$

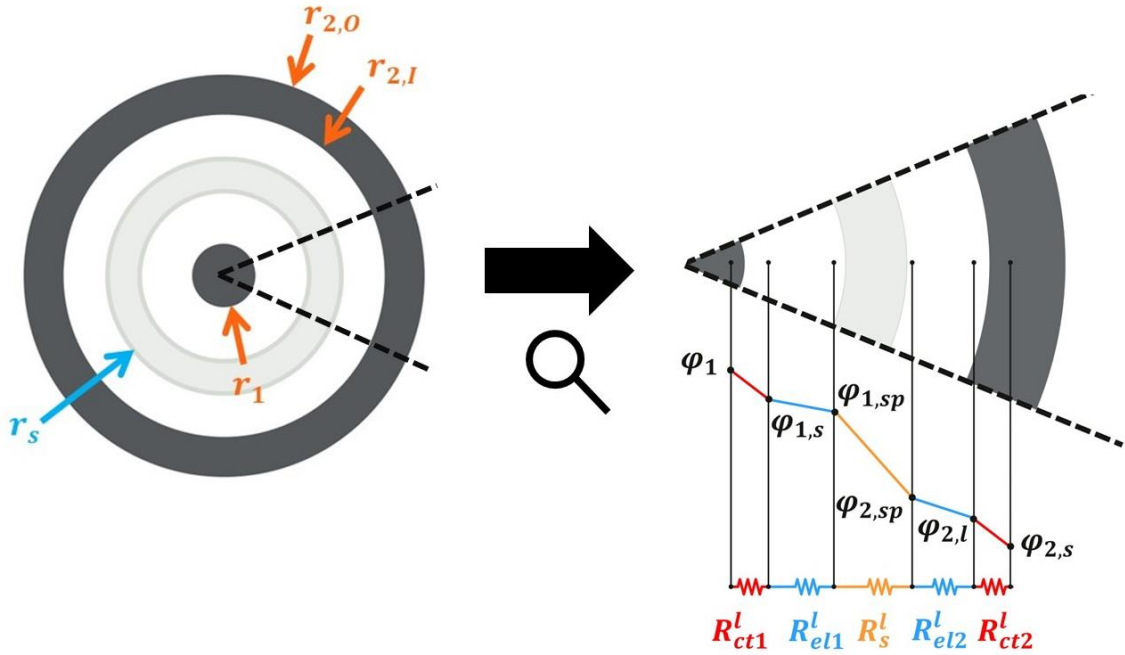


Figure 3.3 – Cross section of the tubular reactor and a sector showing the resistances and the potentials in the radial direction

Where the resistances in the radial direction are now normalized by the unit length (Ω cm) (Figure 3.3, Figure 3.4):

$$R_{ct1}^l = \frac{R_{ct1}}{2\pi r_1} \quad (13)$$

$$R_{ct2}^l = \frac{R_{ct2}}{2\pi r_{2,l}} \quad (14)$$

$$R_{el1}^l = \frac{1}{2\pi\kappa_{el}} \ln \frac{r_s}{r_1} \quad (15)$$

$$R_{el2}^l = \frac{1}{2\pi\kappa_{el}} \ln \frac{r_{2,l}}{r_s + w} \quad (16)$$

$$R_s^l = \frac{1}{2\pi\kappa_s} \ln \frac{r_s + w}{r_s} \quad (17)$$

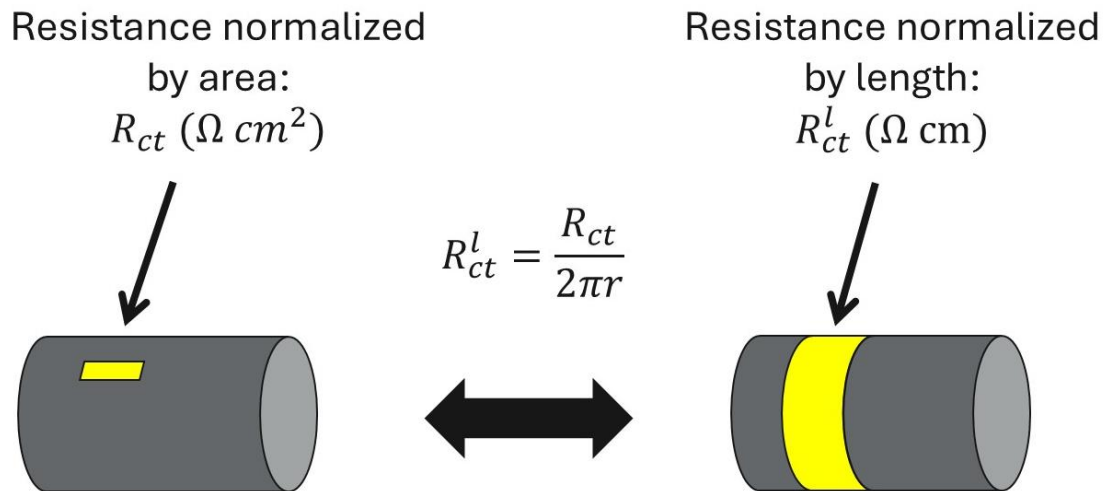


Figure 3.4 - Schematic of the Charge transfer resistance normalized by unit length for the cylindrical geometry.

Where κ_{el} and κ_s represent the ionic conductivities of the electrolyte and the separator, respectively, and w the thickness of the separator. The formulas for the electrolyte and separator resistances are obtained by integrating in the radial direction. The derivation of the electrolyte resistance is shown as an example:

$$R_{el1}^l = \frac{1}{\kappa_{el}} \int_{r_1}^{r_s} \frac{1}{2\pi r} dr = \frac{1}{2\pi\kappa_{el}} \ln \frac{r_s}{r_1} \quad (18)$$

If we assume that the thickness of the separator is much smaller than the interelectrode gap and that the conductivity of the inner and outer electrolyte is the same we can simplify Eq. (15)-(17) to:

$$R_{el}^l = \frac{1}{2\pi\kappa_{el}} \ln \frac{r_{2,l}}{r_1} \quad (19)$$

$$R_s^l = \frac{w}{2\pi\kappa_s} \quad (20)$$

Using Eq. (12) in Eq. (9) the potential in the solution, $\varphi_{1,s}$, is eliminated and the equation can be written as a function of the potential difference between the inner and outer electrode:

$$\frac{dI_1}{dx} = - \frac{1}{R_{ct1}^l + R_{ct2}^l + R_s^l + R_{el}^l} (\varphi_1 - \varphi_2 - U) \quad (21)$$

Where U is the equilibrium voltage of the reactor:

$$U = U_1 - U_2 \quad (22)$$

The concentration of the active species in the electrolyte is assumed to be uniform throughout the length of the reactor. In a flow reactor this can be achieved by adequate

forced convection. As a result, the equilibrium voltage of the reactor, U , will be independent of x . Differentiation of Eq. (21) gives:

$$\frac{d^2 I_1}{dx^2} = -\frac{1}{R_{ct1}^l + R_{ct2}^l + R_s^l + R_{el}^l} \left(\frac{d\varphi_1}{dx} - \frac{d\varphi_2}{dx} \right) \quad (23)$$

Combining the charge balances and Ohm's law, we eliminate the potentials in the two electrodes, and we rewrite Eq. (23) in the following form:

$$\frac{d^2 I_2}{dx^2} = \frac{1}{R_{ct1}^l + R_{ct2}^l + R_s^l + R_{el}^l} \left(\frac{I_2 - I}{A_{c1}\sigma_1} + \frac{I_2}{A_{c2}\sigma_2} \right) \quad (24)$$

Where A_{c1}, A_{c2} are the cross-sectional areas and σ_1, σ_2 are the electronic conductivities of the inner and outer electrode, respectively (Figure 3.3). The individual resistances in the radial direction can be combined in one total resistance:

$$R_{tot}^l = R_{ct1}^l + R_{ct2}^l + R_s^l + R_{el}^l \quad (25)$$

Then, we define dimensionless variables:

$$I^* = \frac{I_2}{I} \quad (26)$$

$$z = \frac{x}{L} \quad (27)$$

$$v^2 = \frac{L^2}{R_{tot}^l} \left(\frac{1}{A_{c1}\sigma_1} + \frac{1}{A_{c2}\sigma_2} \right) \quad (28)$$

$$K_r = \frac{A_{c2}\sigma_2}{A_{c1}\sigma_1} = \frac{(r_{2,0}^2 - r_{2,I}^2)\sigma_2}{r_1^2\sigma_1} \quad (29)$$

Where I is the total current applied on the electrode. After substituting in Eq. (24) we get:

$$\frac{d^2 I^*}{dz^2} = v^2 \left(I^* - \frac{K_r}{1 + K_r} \right) \quad (30)$$

This equation governs the current in the electrodes. The current on the outer electrode is zero at the end of the outer electrode ($x=0$) and equal to the applied current I at the current collector ($x=1$). Therefore, the boundary conditions are:

$$I^*(0) = 0 \quad (31)$$

$$I^*(1) = 1 \quad (32)$$

3.2.2 Tafel Kinetics Formulation

Here, we show the analysis for Tafel kinetics. The Tafel equation is derived from Eq. (7) at high overpotentials. Assuming anodic Tafel kinetics for the inner electrode and cathodic Tafel kinetics for the outer electrode:

$$i_{n,1} = i_{0,1} e^{\beta_1(\varphi_1 - \varphi_{1,s} - U_1)} \quad (33)$$

$$i_{n,2} = -i_{0,2} e^{-\beta_2(\varphi_2 - \varphi_{2,s} - U_2)} \quad (34)$$

Where:

$$\beta_1 = \frac{\alpha_{a,1} F}{RT} \quad (35)$$

$$\beta_2 = \frac{\alpha_{c,2} F}{RT} \quad (36)$$

Differentiating Eq. (6) using the Tafel kinetics instead of linear kinetics we get:

$$\frac{d^2 I_1}{dx^2} = \frac{dI_1}{dx} \beta_1 \left(\frac{d\varphi_1}{dx} - \frac{d\varphi_{1,s}}{dx} \right) \quad (37)$$

$$\frac{d^2 I_2}{dx^2} = -\frac{dI_2}{dx} \beta_2 \left(\frac{d\varphi_2}{dx} - \frac{d\varphi_{2,s}}{dx} \right) \quad (38)$$

From Eq. (37) and Eq. (38) and the total charge balance the following relationship between the potentials can be obtained:

$$\beta_1 \left(\frac{d\varphi_1}{dx} - \frac{d\varphi_{1,s}}{dx} \right) = -\beta_2 \left(\frac{d\varphi_2}{dx} - \frac{d\varphi_{2,s}}{dx} \right) \quad (39)$$

The potentials in the solution next to the two electrodes are also related:

$$\varphi_{2,s} = \varphi_{1,s} - \frac{dI_2}{dx} (R_s^l + R_{el}^l) \quad (40)$$

Eq. (39) and Eq. (40) can be used to eliminate the potential in the solution in Eq. (38):

$$\frac{d^2 I_2}{dx^2} = \frac{dI_2}{dx} \frac{\beta_1 \beta_2}{\beta_1 + \beta_2} \left(\left(\frac{1}{A_{c1} \sigma_1} + \frac{1}{A_{c2} \sigma_2} \right) I_2 - \frac{I}{A_{c1} \sigma_1} - \frac{d^2 I_2}{dx^2} (R_s^l + R_{el}^l) \right) \quad (41)$$

Using dimensionless variables and the B.C. defined in Eq. (31),(32):

$$\left(1 + \gamma \frac{dI^*}{dz} \right) \frac{d^2 I^*}{dz^2} = \frac{dI^*}{dz} (\delta I^* - \varepsilon) \quad (42)$$

Where:

$$\gamma \equiv \frac{I(R_s^l + R_{el}^l)}{L} \frac{\beta_1 \beta_2}{\beta_1 + \beta_2} \quad (43)$$

$$\delta \equiv LI \frac{\beta_1 \beta_2}{\beta_1 + \beta_2} \left(\frac{1}{A_{c1} \sigma_1} + \frac{1}{A_{c2} \sigma_2} \right) \quad (44)$$

$$\varepsilon \equiv \frac{LI}{A_{c1} \sigma_1} \frac{\beta_1 \beta_2}{\beta_1 + \beta_2} \quad (45)$$

Setting:

$$p = \frac{dI^*}{dz} \quad (46)$$

The equation can be simplified to:

$$(1 + \gamma p) \frac{dp}{dI^*} = \delta I^* - \varepsilon \quad (47)$$

Eq. (47) cannot be analytically solved. In the case of $\gamma = 0$, a solution can be obtained in implicit form as in the original work by Newman and Tobias in their treatment of the porous electrode with Tafel kinetics. This condition corresponds to negligible electrolyte and separator resistance.

3.3 Results and Discussion

3.3.1 Current and Current Density Distribution along the Reactor Length

By solving Eq. (30), we obtain the current in the outer and the inner electrode respectively:

$$I^* = \frac{K_r}{1 + K_r} + \frac{\sinh(\nu z) + K_r \sinh(\nu(z - 1))}{(1 + K_r) \sinh(\nu)} \quad (48)$$

$$\frac{I_1}{I} = 1 - I^* = \frac{1}{1 + K_r} - \frac{\sinh(\nu z) + K_r \sinh(\nu(z - 1))}{(1 + K_r) \sinh(\nu)} \quad (49)$$

The current density can be obtained by rearranging Eq. (4). However, to make the distribution independent of the geometry, the derivative of the current will be used since it is directly proportional to the current density:

$$-\frac{dI_1}{dz} = 2\pi r_s Li_{n,1} \quad (50)$$

$$-\frac{dI_1}{dz} = \nu \frac{\cosh(\nu z) + K_r \cosh(\nu(z - 1))}{(1 + K_r) \sinh(\nu)} \quad (51)$$

The total current and the current density distribution along the length of the reactor depends on the two dimensionless parameters ν and K_r . The first parameter ν is the ratio of the total ohmic resistance of electrodes of length L along the x direction and the sum of the other resistances in the radial direction for a reactor of length L :

$$\nu^2 = \frac{\text{Ohmic resistance in the } x - \text{direction}}{\text{Total resistance in the } r - \text{direction}} \quad (52)$$

A higher ν value indicates a predominant influence of the electrodes' ohmic resistance on the current distribution, whereas a lower ν value indicates that kinetic, electrolyte, and separator resistances are dominating. The second parameter, K_r , represents the ratio of the resistances per unit length of the two electrodes. The resistance per unit length is used since it depends on both the specific conductivity of the material and the cross-sectional area. They are both design variables since the first depends on the choice of material and the second on the dimensions of the electrodes. High K_r values suggest high inner electrode resistance, while low values indicate high outer electrode resistance:

$$K_r = \frac{\text{Ohmic resistance of inner electrode}}{\text{Ohmic resistance of outer electrode}} \quad (53)$$

The current distribution along the length of the reactor is shown in Figure 3.5a,c,d. Assuming same conductivity for the two electrodes ($K_r = 1$), the current distribution is symmetric. At high values of ν , the ohmic resistance of the electrodes dominates and the current density is high only near the current collectors to minimize the path the electrons have to travel along the electrodes. At low values of ν , the charge transfer, electrolyte and separator resistances dominate, and the current density becomes more uniform throughout the electrode to avoid high local polarization (Figure 3.5c). For a given ratio of resistances, ν , the value of K_r controls the symmetry of the distribution. Deviations from $K_r = 1$ result in asymmetry. High values of K_r indicate superior conductivity for the outer electrode, and as a result the current density shifts towards the current collector of the inner electrode to reduce ohmic losses (Figure 3.5d). Similarly for low values of K_r the current density would shift towards the current collector of the outer electrode. In fact, the current distribution for

every value of K_r is symmetric with respect to the line at $z = 0.5$ with the current distribution of $\dot{K}_r = 1/K_r$.

Figure 3.5b, e-g illustrate the currents within the solid phases of the two electrodes. Initially, we consider electrodes with the same conductivity. At low values of ν , the current distribution is uniform and as a result the current in the solid phases changes linearly with the distance from the current collectors (Figure 3.5e). With higher values of ν , the current density is high close to the current collectors and low in between. As a result, the current in the solid phases changes significantly close to the current collectors and remains roughly constant in between (Figure 3.5f). When the conductivity of the electrodes is not identical, the current in the solid phase will travel preferably in the electrode of the highest conductivity. This results in shifting the current density closer to the least conductive electrode to minimize the distance it must travel within it (Figure 3.5g).

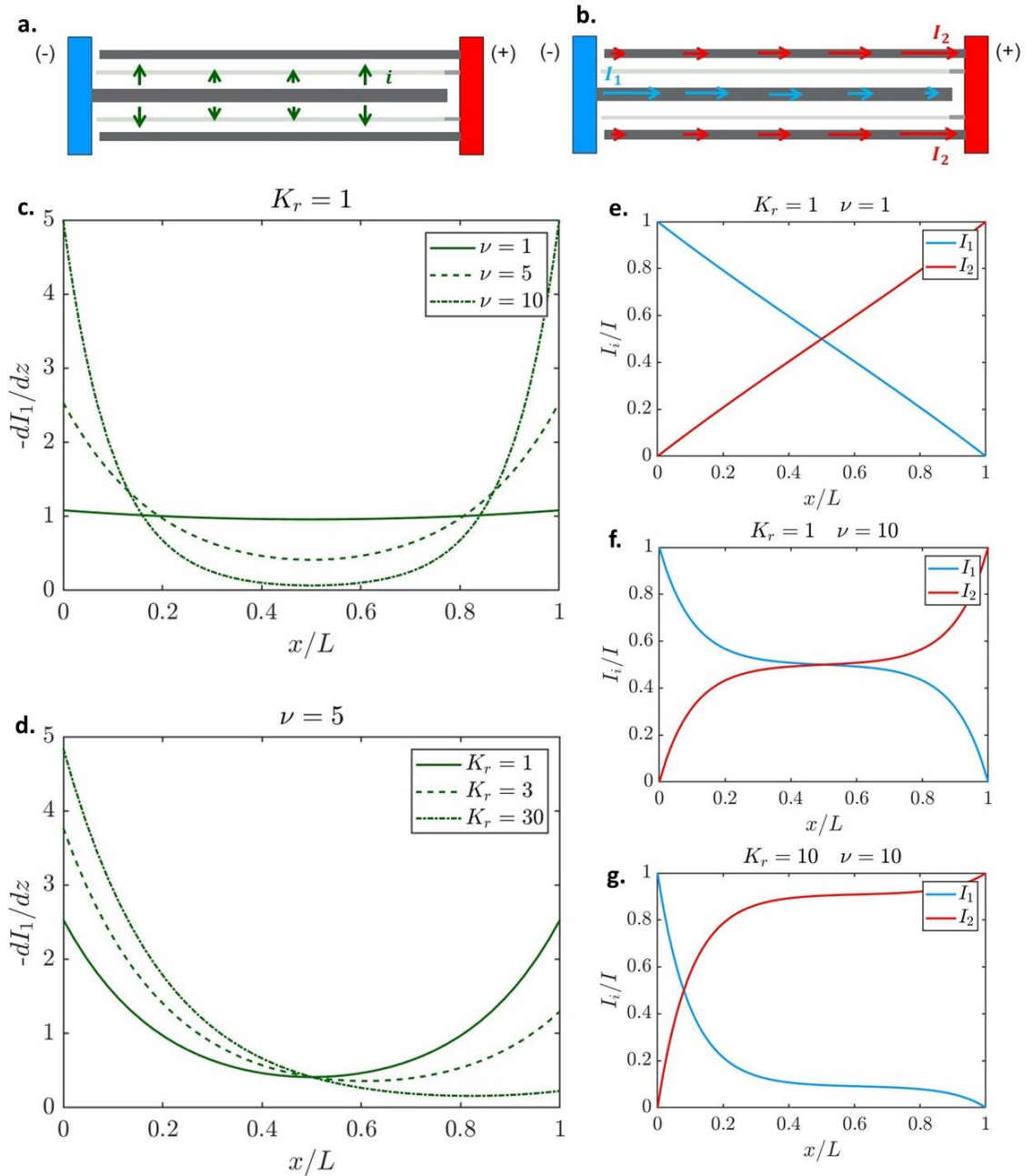


Figure 3.5 - a) Schematic of the current density distribution for a tubular flow reactor. b) Schematic of the distribution of the current in the electrodes for a tubular flow reactor. c) Current density distribution for different values of the parameter ν and for $K_r=1$. d) Current density distribution for different values of the parameter K_r and for $\nu=1$. Distribution of the current in the electrodes for e) $K_r=1$ and $\nu=1$, f) $K_r=1$ and $\nu=10$, g) $K_r=10$ and $\nu=10$.

To evaluate the accuracy of the linear approximation we compare the analytical solution with the solution obtained by COMSOL when simulating the secondary current

distribution with Butler-Volmer kinetics. The simulations were done at different current densities to show how increasing polarization can cause deviations from the analytical model (Figure 3.6). The comparison shows that at 1 mA cm^{-2} the average error is 3%, at 100 mA cm^{-2} the error increases slightly to 5%, and at 1000 mA cm^{-2} the error jumps to 21% showing that the linear approximation becomes less accurate at high polarization (Figure 3.5). The parameters used for both the analytical solution and COMSOL are shown in Table 3.1 and Table 3.2.

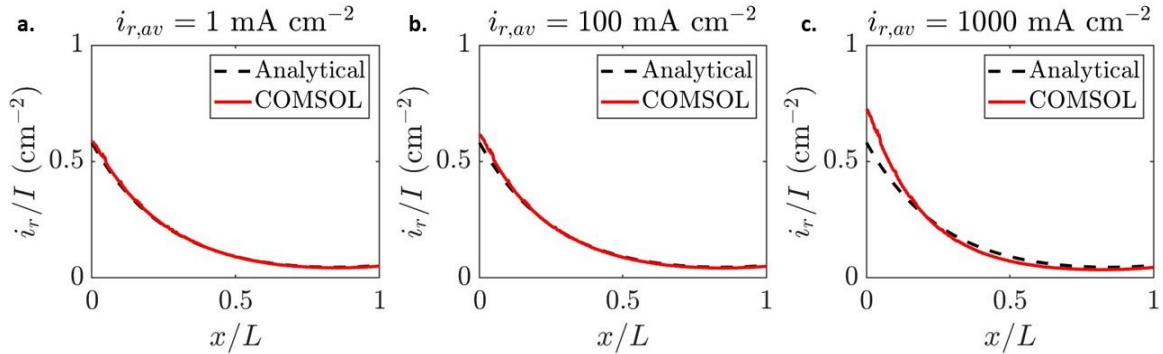


Figure 3.6 - Comparison of the normalized current distribution predicted by the analytical model with linear kinetics and by COMSOL with Butler-Volmer kinetics a) at 1 mA cm^{-2} b) at 10 mA cm^{-2} c) at 1000 mA cm^{-2}

Table 3.1 – Parameters used when using the model equations to visualize trends in the ASR of a tubular Vanadium Flow Battery as a case study. The values depicted are typical values found in parallel plate VRFB studies in the literature.

Parameter	Value	Units	Ref.
R_{ct1}	0.1	$\Omega \text{ cm}^2$	66
R_{ct2}	0.1	$\Omega \text{ cm}^2$	66
w	100	μm	67
κ_s	0.1	S cm^{-1}	67
κ_{el}	0.3	S cm^{-1}	50

Table 3.2 - Geometric parameters used in the COMSOL simulation and the analytical solution to evaluate the deviation at high polarizations.

Parameter	Value	Units
r_s	1	mm
r_1	0.5	mm
$r_{2,I}$	1.3	mm
$r_{2,O}$	2.6	mm
L	10	cm
σ_1	820	S cm
σ_2	820	S cm

3.3.2 Electrode Potential Distribution along the Reactor Length

Ohm's law can be used to obtain the potential distribution on each electrode:

$$I_1 = -\frac{A_{c1}\sigma_1}{L} \frac{d\varphi_1}{dz} \quad (54)$$

$$I_2 = -\frac{A_{c2}\sigma_2}{L} \frac{d\varphi_2}{dz} \quad (55)$$

Integrating Eq. (54),(55) we obtain the dimensionless potential at each location of the electrodes relative to the potential of the corresponding current collectors:

$$\varphi_1^*(z) - \varphi_{1,z=0}^* = \quad (56)$$

$$\frac{K_r}{K_r + 1} \left(\frac{\cosh(\nu z) + K_r \cosh(\nu(z-1)) - K_r \cosh(\nu) - 1}{\nu(1 + K_r) \sinh(\nu)} - \frac{1}{1 + K_r} z \right)$$

$$\varphi_2^*(z) - \varphi_{2,z=1}^* =$$

$$\begin{aligned} & \frac{I}{K_r + 1} \left(\frac{K_r}{1 + K_r} (1 - z) \right. \\ & \left. + \frac{\cosh(\nu) + K_r - \cosh(\nu z) - K_r \cosh(\nu(z-1))}{\nu(1 + K_r) \sinh(\nu)} \right) \end{aligned} \quad (57)$$

Where:

$$\varphi_1^*(z) - \varphi_1^*(0) = \frac{\varphi_1(z) - \varphi_{1,z=0}}{IL \left(\frac{1}{A_{c1}\sigma_1} + \frac{1}{A_{c2}\sigma_2} \right)} \quad (58)$$

$$\varphi_2^*(z) - \varphi_2^*(1) = \frac{\varphi_2(z) - \varphi_{2,z=1}}{IL \left(\frac{1}{A_{c1}\sigma_1} + \frac{1}{A_{c2}\sigma_2} \right)} \quad (59)$$

The results are shown in Figure 3.7a-c. Assuming a current is flowing in the positive z-direction, the potential of both electrodes is decreasing. When the conductivity of the two electrodes is identical ($K_r = 1$) the ohmic potential drop is the same in both electrodes regardless of the value of ν . The value of ν affects the linearity of the potential distribution. For higher values of ν , the potential changes roughly linearly except close to the current collectors, whereas for lower values of ν the potential does not show linear regions (Figure

3.7a,b). This shows that when the ohmic resistance of the electrodes is dominant, the electrodes act as ohmic resistors. When the electrodes have different resistances the ohmic potential drop is not the same for both electrodes. The case for a more conductive outer electrode is shown Figure 3.7c. In this case the ohmic drop is higher for the least conductive electrode.

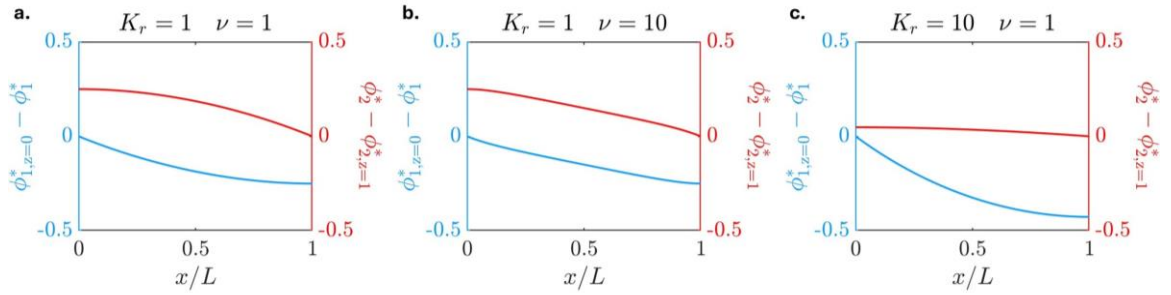


Figure 3.7 - Inner (blue) and outer (red) electrode potential distribution a) $K_r=1$ and $\nu=1$, b) $K_r=1$ and $\nu=10$, c) $K_r=10$ and $\nu=1$.

The potential difference between the two electrodes at each location along the length of the battery can be calculated by rearranging Eq. (21):

$$\varphi_1(z) - \varphi_2(z) - U = -\frac{R_{tot}^l}{L} \frac{dI_1}{dz} \quad (60)$$

$$\varphi_1(z) - \varphi_2(z) - U = \frac{IR_{tot}^l \nu}{L} \left(\frac{\cosh(\nu z) + K_r \cosh(\nu(z - l))}{(1 + K_r) \sinh(\nu)} \right) \quad (61)$$

3.3.3 Reactor Resistance and Area Specific Resistance

Another very important metric of an electrochemical reactor is its resistance. The total resistance of the tubular reactor can be calculated from the following equation, using Eq. (56)-(61):

$$R_{tot} = \frac{\varphi_1(0) - \varphi_2(1) - U}{I} \quad (62)$$

In contrast to the parallel plate reactor, the electrodes and the separator of the tubular reactor do not necessarily have the same geometric surface area. Therefore, the resistance can be normalized by the surface of either electrode or the separator. In this analysis, to obtain an area specific resistance for the reactor we choose to normalize by the separator surface area. After multiplying Eq. (60) by the separator surface area and substituting for the potential difference we get:

$$ASR = 2\pi r_s R_{tot}^l \left(\nu \coth(\nu) + \frac{K_r}{(1 + K_r)^2} \frac{2\nu + \nu^2 \sinh(\nu) - 2\nu \cosh(\nu)}{\sinh(\nu)} \right) \quad (63)$$

This formulation of the ASR includes contributions from both the charge transfer resistance and the ohmic resistance since in the tubular reactor it is not straightforward to isolate the individual components. The expression in the parenthesis depends on the electrode properties, geometry, and relative conductivities of the two electrodes. As the electrode length approaches zero, leading to ν also approaching zero, the term in the parenthesis tends to one. Since the term in the parenthesis is bigger or equal than one, in the limiting case of ν going to zero, we reach the minimum ASR:

$$ASR_{min} = \lim_{v \rightarrow 0} ASR = 2\pi r_s R_{tot}^l \quad (64)$$

The minimum ASR is proportional to the sum of the resistances in the radial direction, which include the charge transfer resistance of each electrode surface, the resistance of the electrolyte and the resistance of the separator (Eq. (13),(14),(19),(20)). These resistances depend on the reaction kinetics, on the conductivities of the electrolyte and the separator, as well as the geometry of the reactor. Specifically, the geometry's impact on the minimum ASR is determined by several factors: the radius of the inner electrode, the inner diameter of the outer electrode, the membrane's radius, and the gap between the electrodes. The principal variables that will be explored are the inner electrode radius, r_1 , and the gap between the inner electrode and the outer electrode, d (Figure 3.8a). By assuming equal electrolyte volumes in the inner and outer flow channels, we can calculate the membrane's radius, r_s , based on these two parameters:

$$L\pi((r_1 + d)^2 - r_s^2) = L\pi(r_s^2 - r_1^2) \quad (65)$$

An expression for the minimum ASR that depends on material properties and the geometry can be obtained by Eq. (64) and Eq. (13),(14),(19),(20):

$$ASR_{min} = 2\pi r_s \left(\frac{R_{ct1}}{2\pi r_1} + \frac{R_{ct2}}{2\pi r_2} + \frac{w}{\kappa_s 2\pi r_s} + \frac{1}{2\pi \kappa_{el}} \ln \frac{r_2}{r_1} \right) \quad (66)$$

$$ASR_{min} = \frac{r_s}{r_1} R_{ct1} + \frac{r_s}{r_{2,l}} R_{ct2} + \frac{W}{\kappa_s} + \frac{r_s}{\kappa_{el}} \ln \frac{r_{2,l}}{r_1} \quad (67)$$

The ASR_{min} is plotted in Figure 3.8b-e for a vanadium flow battery as a case study. The charge transfer resistances, the electrolyte conductivity and separator conductivity used are typical for a vanadium flow battery and are shown in Table 3.1. In Figure 3.8b,d, we keep the inner electrode's radius constant but change the space between the electrodes. At both 0.1 mm and 1 mm electrode radius we observe the same increasing trend with the interelectrode distance. This rise in resistance is mainly due to the electrolyte, as ions have to travel a longer distance when the gap is larger. With smaller electrode radius, this increase in resistance is more pronounced, and there is also a bigger impact from the resistance due to charge transfer at the inner electrode. This behavior can be explained by the smaller surface area of the inner electrode for both the reaction and the ion conduction in the solution. In Figure 3.8c,e the interelectrode distance is kept constant and the radius of the inner electrode varies. The ASR is plotted for two different electrode gaps of 1 mm and 2 mm. In both scenarios, the minimum ASR first drops as the electrode gets thicker but then levels off. This pattern suggests that when the inner electrode becomes too small, its small surface area negatively affects the minimum ASR. Depending on the properties and the interelectrode gap, there is a certain thickness-a 'critical radius'-where the ASR stops decreasing and plateaus. Making the electrode thicker beyond this point doesn't improve the reactor's performance and would only make the electrode larger, thus increasing the footprint. As seen in the previous figures, increasing the gap mainly raises the resistance due to the electrolyte and charge transfer at the inner electrode.

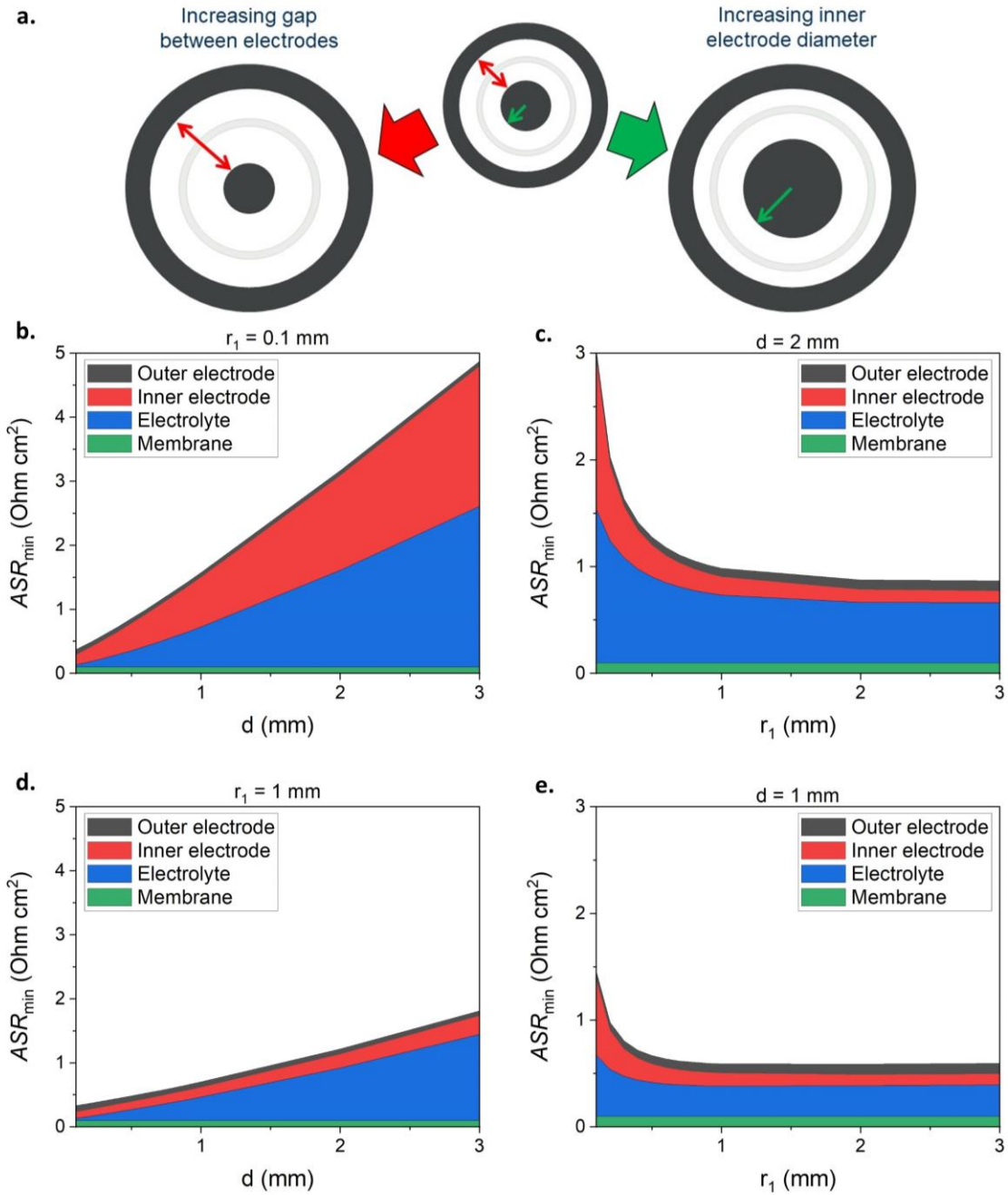


Figure 3.8 - a) Changes in reactor geometry by changing interelectrode gap or radius of inner electrode b) Minimum Area Specific Resistance variation with interelectrode gap when radius of inner electrode equals to 0.1 mm c) Minimum Area Specific Resistance variation with inner electrode radius when interelectrode gap equals to 2 mm d) Minimum Area Specific Resistance variation with interelectrode gap when radius of inner electrode equals to 1 mm c) Minimum Area Specific Resistance variation with inner electrode radius when interelectrode gap equals to 1 mm

Regarding the total ASR, the impact of the parameters ν and K_r is illustrated in Figure 3.9a. Regardless of the value of K_r , the ASR is increasing with increasing ν . This indicates that the ASR increases with increasing electrode length and with increasing electrode ohmic resistance relative to the radial resistance (Eq. (28)). The lowest ASR is achieved when K_r is close to zero or infinity, which occurs when one electrode is much more conductive than the other. Conversely, ASR peaks when K_r is equal to one.

To delve deeper into the ASR, the case of one controlling electrode will be examined using realistic numbers. Assuming the outer electrode is perfectly conductive, we focus on how the inner electrode's properties affect the ASR. A critical aspect is determining a maximum electrode length before ASR notably increases, given that ASR increases with ν . This exploration involves considering both material properties and reactor geometry. In Figure 3.9b we plot the average ASR for reactors up to 50 cm in length with an ASR_{\min} of 1 Ohm cm², a separator of 2 mm diameter and an inner electrode of 1 mm diameter for different inner electrode materials (Graphite: 8.2×10^2 S cm⁻¹, Ti: 2.4×10^4 S cm⁻¹, Cu: 6×10^5 S cm⁻¹). The results indicate that with graphite, at 10 cm length, the ASR of the reactor has already doubled. Ti can reach up to 30 cm before the ASR doubles, whereas Cu does not show any significant increase up to 50 cm long reactors. The electrical conductivity, therefore, has a significant effect on the variation of the ASR with the reactor length.

Furthermore, we analyzed how the reactor geometry affects the total ASR, as shown in Figure 3.9c,d, by varying the inner electrode's diameter and the gap between electrodes, with titanium as the material of choice. The change in the inner electrode's thickness has a dual effect on the reactor's resistance: its influence on both the minimum ASR and the variable ν , which depends on ASR_{\min} and the inner electrode cross-sectional area (A_{c1}).

This dual influence is evident by a reduction in ASR_{min} and a mitigated increase in ASR with reactor length, demonstrating the positive role of increasing inner electrode radius on the total ASR (Figure 3.9c). From Figure 3.9b we observed that low conductivity negatively impacts the ASR and Figure 3.9c shows that for a given conductivity an increase in electrode diameters decreases the ASR. These observations indicate that a low conductivity material requires a larger electrode to maintain a low ASR, whereas a high conductivity material can use smaller electrodes without significantly sacrificing performance. The effect of decreasing the gap between the electrodes is shown in Figure 3.9d. A narrower gap lowers the electrolyte resistance and therefore has a direct effect on the ASR_{min} . The variation of the ASR with the length is not significantly affected by the interelectrode gap.

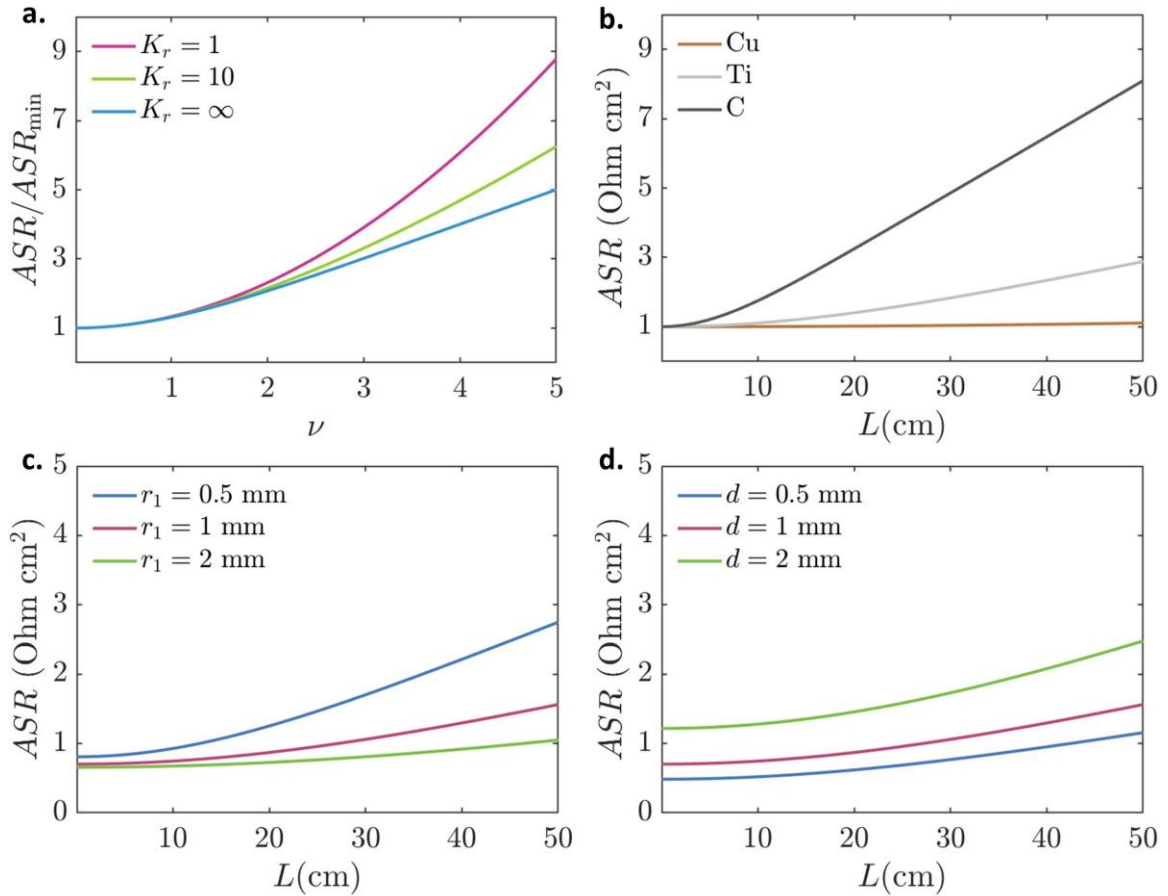


Figure 3.9 - a) Ratio of ASR to minimum ASR variation with ν for different values of K_r b) Total ASR variation with tubular reactor length for different inner electrode materials and $ASR_{min}=1$, $r_s=1$ mm, $r_1=0.5$ mm. c) Total ASR variation with tubular reactor length for Ti inner electrode with different radii and interelectrode gap of $d=0.5$ mm. d) Total ASR variation with tubular reactor length for Ti inner electrode with different interelectrode gaps and inner electrode radius of $r_1=1$ mm.

3.3.4 Porous Electrode Theory and Tubular Reactor Model Comparison

Even though the tubular reactor model is analogous to the model of the porous electrode, the dependence of the ASR on the characteristic length-thickness or length-is different. The ASR of the porous electrode, derived by Newman and Tiedemann, shows a minimum as the thickness of the electrode increases, while the ASR of the tubular reactor increases constantly with increasing length.^{63,64} The reason for this different behavior is

caused by the way the resistance is normalized to area specific resistance. To demonstrate this, we compare a symmetric parallel plate reactor with porous electrodes with a tubular reactor (Figure 3.10a). The total resistance of the planar reactor can be obtained by the following formula:

$$R_{planar} = 2R_p + R_s \quad (68)$$

Where R_p is the total resistance of each porous electrode and R_s the resistance of the separator. The total resistance and the ASR of the porous electrode differ only by the geometric surface area, A_p , with the dependence on the parameters v_p and $K_{r,p}$ being the same.⁴⁹

$$R_p = \frac{1}{A_p} \frac{L_p}{\sigma + \kappa} \left(1 + \frac{2 + \left(\frac{\sigma}{\kappa} + \frac{\kappa}{\sigma} \right) \cosh(v_p)}{v_p \sinh(v_p)} \right) \quad (69)$$

$$ASR_p = \frac{L_p}{\sigma + \kappa} \left(1 + \frac{2 + \left(\frac{\sigma}{\kappa} + \frac{\kappa}{\sigma} \right) \cosh(v_p)}{v_p \sinh(v_p)} \right) \quad (70)$$

Where L_p is the thickness, κ and σ the conductivity of the electrolyte and the solid phase, respectively. The parameter v_p and $K_{r,p}$ are defined as follows:

$$v_p^2 = \frac{aL_p^2}{R_{ct,p}} \left(\frac{1}{\sigma} + \frac{1}{\kappa} \right) \quad (71)$$

$$K_{r,p} = \frac{\kappa}{\sigma} \quad (72)$$

Where $R_{ct,p}$ is defined similarly to $R_{ct,1}$ and $R_{ct,2}$ but for the reaction taking place in the porous electrode. Here the parameter ν_p expresses the ratio of the ohmic resistance to the charge transfer resistance and the parameter $K_{r,p}$ the ratio of the conductivity of the electrolyte to the conductivity of the solid phase of the porous electrode. To compare the trends in the ASR of the two models, it is useful to compare the dependence on the parameters ν_p and ν since the characteristic length of each model is proportional to the corresponding dimensionless parameter. By eliminating the characteristic length from the ASR of the porous electrode we get:

$$ASR_p = \sqrt{\frac{R_{ct,p}\sigma\kappa}{(\sigma + \kappa)^3\alpha}} \left(\nu_p + \frac{2 + \left(K_{r,p} + \frac{1}{K_{r,p}}\right) \cosh(\nu_p)}{\sinh(\nu_p)} \right) \quad (73)$$

In the tubular reactor model, the total resistance can be written as follows:

$$R_{tot} = \sqrt{\frac{R_{tot}^l A_{c1}\sigma_1 A_{c2}\sigma_2}{(A_{c1}\sigma_1 + A_{c2}\sigma_2)^3}} \left(\nu + \frac{2 + \left(K_r + \frac{1}{K_r}\right) \cosh(\nu)}{\sinh(\nu)} \right) \quad (74)$$

However, the ASR of the tubular reactor is obtained by multiplying by the length of the reactor and the circumference of the membrane:

$$ASR = 2\pi r_s L R_{tot} \quad (75)$$

And after eliminating the characteristic length:

$$ASR = \frac{2\pi r_s R_{tot}^l A_{c1} \sigma_1 A_{c2} \sigma_2}{(A_{c1} \sigma_1 + A_{c2} \sigma_2)^2} \left(v^2 + v \frac{2 + \left(K_r + \frac{1}{K_r} \right) \cosh(v)}{\sinh(v)} \right) \quad (76)$$

It is clear from Eq. (73) that the ASR of the planar reactor has the same dependence on the thickness as the ASR of the porous electrode, since the resistance of the separator is not affected by the thickness of the electrodes. To compare the two configurations, we plot the dimensionless ASR of the porous electrode and the dimensionless ASR of the tubular reactor (Figure 3.10b). The ASR of the porous electrode shows a minimum whereas the ASR of the tubular reactor, interestingly, only increases. In a porous electrode, there are two regimes for the ASR. For thinner electrodes, the charge transfer resistance is the main contributor to the resistance of the electrode, since the interfacial area is low (Figure 3.10a,b). Therefore, increasing the thickness decreases the resistance of the electrode and, since the membrane surface area is constant, the ASR decreases as well. When the minimum of the ASR is reached, the interfacial area ceases to be the limitation and the ohmic resistance of the electrolyte and the solid phase becomes the controlling factor. As a result, further increasing the thickness increases the ASR of the electrode (Figure 3.10a,b). These trends can be mathematically derived from Eq. (73) assuming very thin or very thick electrodes:

$$ASR_p \propto \frac{1}{L_p}, \text{ when } L_p \rightarrow 0 \quad (77)$$

$$ASR_p \propto L_p, \text{ when } L_p \rightarrow \infty \quad (78)$$

For the tubular reactor, the total resistance of the reactor follows the same behavior as the total resistance of the porous electrode, experiencing a minimum with the length (Eq. (74)). However, the ASR of the tubular electrode is calculated based on the surface area of the tubular membrane which, in contrast to the porous electrode, increases with the length (Figure 3.10a,b). The initial decrease in the total resistance of the reactor is accompanied by an increase in membrane surface area, keeping the ASR constant. From Eq. (76):

$$ASR \propto \frac{1}{L} L, \text{ when } L \rightarrow 0 \quad (79)$$

$$ASR \propto L^2, \text{ when } L \rightarrow \infty \quad (80)$$

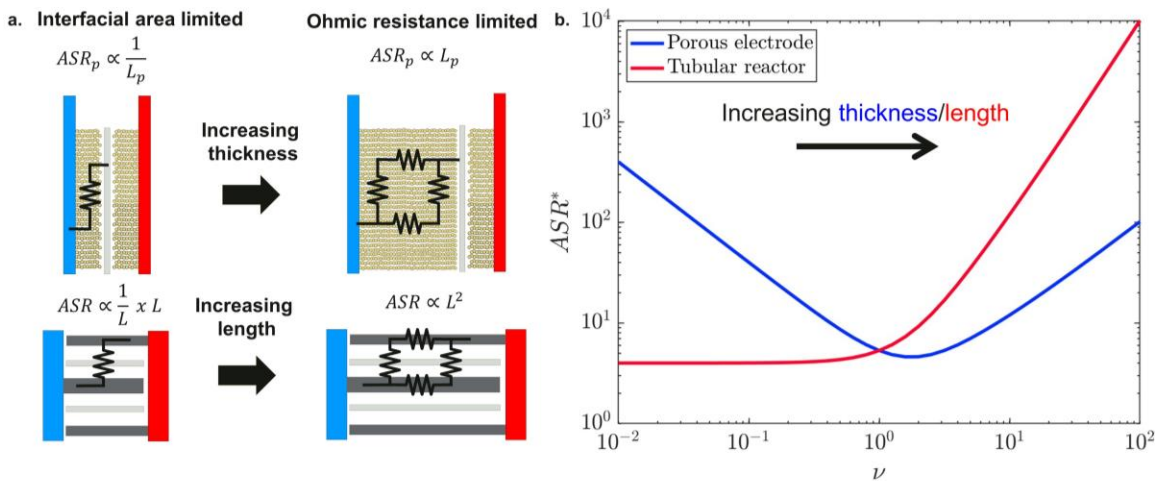


Figure 3.10 - a) Comparison of the ASR of the porous electrode model and tubular reactor model. b) Dependence of dimensionless ASR of the porous electrode model and of the tubular reactor model on the dimensionless parameter ν .

The porous electrode theory with linear kinetics can also be combined with the tubular reactor model when porous electrodes are used in a tubular reactor. The analysis followed in this work is based on a flow-by configuration with the reaction occurring directly on the surface of the electrodes (Figure 3.11a). The addition of a porous electrode can lead to two more configurations that have been used in tubular reactors: flow-by with porous electrode and flow-through with porous electrode (Figure 3.11b,c).^{17,68} To model the flow-by with porous electrode configuration, R_{ct1} and R_{ct2} can be replaced by porous electrode resistances, while keeping the electrolyte resistance for the space between the porous electrodes and the separator (Figure 3.11b). Similarly, the flow-through with porous electrode configuration can be modelled by replacing the charge-transfer resistances with porous electrode resistances and removing the electrolyte resistance (Figure 3.11c).

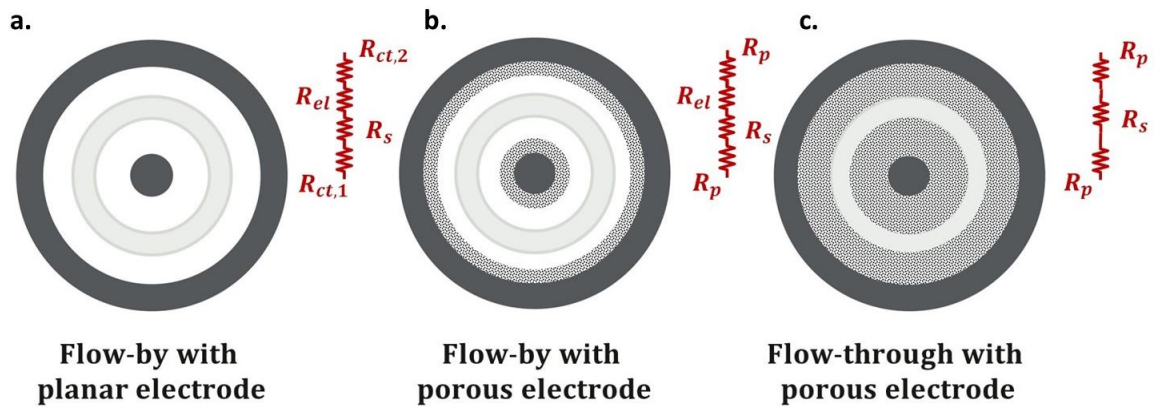


Figure 3.11 - a) Flow-by electrodes b) Flow-by (porous) electrodes c) Flow-through (porous) electrodes

3.3.5 Limitations of the Model

The approach followed in this work simplifies the complex phenomena that occur in an electrochemical flow reactor to allow analytical solution to the equations. The linear kinetics solution limits the applicability of the model in low polarization scenarios, that is

overpotentials of 10 mV or less.⁴⁹ For high active species concentration, the absence of mass-transport limitations in low polarizations is a realistic assumption. However, the Tafel kinetics solution that is presented in the Appendix ignores any mass transport limitation, which typically appears at high polarizations. Such an assumption can lead to an overestimation of the current density in parts of the reactor that the limiting current would be reached. The assumption of constant concentration of active species along the length of the reactor limits the validity to low single pass conversion operation. Low single pass conversion occurs when the total current is low or the flowrate is sufficiently high.

3.4 Conclusions

An analytical model for tubular electrochemical reactors has been developed for the first time. This model offers insight into how the geometry and material choices impact the reactor's performance. A key discovery in our study is that the tubular flow reactor can show uneven current distribution under certain conditions, notably when electrodes have high resistance or small cross-sectional areas, leading to poor electrode utilization. Furthermore, our analysis has identified a critical electrode radius, that optimizes reactor performance while maintaining minimal reactor dimensions. It is evident that reducing the electrode gap is advantageous, as it directly lessens electrolyte resistance. Another significant finding is the increase in the ASR of reactor with the length. Reactors utilizing highly conductive electrodes can mitigate the ASR increase, enabling higher power outputs. Looking forward, this model provides a set of tools that can be used for preliminary assessment of tubular reactor designs before more accurate and thorough computational methods are employed.

CHAPTER 4. ENHANCED SCALABILITY IN MICROTUBULAR VANADIUM FLOW BATTERIES VIA COPPER ANODES

4.1 Introduction

Scaling up microtubular vanadium flow batteries is critical for improving their commercial viability and practical application in energy storage systems. However, their scalability has not been proven yet. The analytical model for tubular reactors indicates that this geometry is susceptible to an increase in the ASR as the length of the battery increases. This increase in resistance presents a significant challenge to scalability, as it directly impacts battery performance by reducing energy efficiency.

A potential solution to this problem is the use of highly conductive electrodes. The conductivity of an electrode is determined by the material's intrinsic electrical properties (resistivity) and its cross-sectional area. Electrodes with low resistivity and larger cross-sectional areas can mitigate the increase in resistance. However, in the context of microtubular reactors, design constraints limit the size of the electrode. For example, the diameter of the inner electrode needs to be less than 1 mm if the membrane's inner diameter is 1 mm. This condition restricts the possibilities for increasing the cross-sectional area of the electrode as a way to increase its conductivity, leaving only the electrical resistivity as the means to mitigate the ASR increase.

In flow battery applications, the selected electrode materials must satisfy additional criteria, apart from low resistivity, such as chemical stability, minimization of side reactions and cost. Chemical stability is crucial to prevent degradation or corrosion during

battery operation, meaning the materials must be compatible with the electrolytes. Furthermore, the electrode surface must act as an effective catalyst for the redox reactions occurring in the flow battery, while minimizing unwanted side reactions. Finally, cost considerations are essential, as the electrode material needs to be affordable to keep the overall capital cost low.

In conventional Vanadium flow batteries, graphite has been the most ubiquitous electrode satisfying all of these requirements to a very high degree. Chemical stability in both anolyte and catholyte, facile kinetics for the Vanadium reaction while suppressing the Hydrogen Evolution Reaction (HER), and low cost. However, in microtubular VRFB use of graphite-based materials may not be ideal. Fiber-shaped batteries have shown high resistance when using graphitic carbon fibers as electrodes.^{69,70} In Zn-I microtubular flow batteries the use of carbon fibers gave a high HFR.^{16,35} These findings indicate that graphite's resistivity may not be low enough for this geometry.

In this work, we present copper wires as anodic electrodes to enhance the scalability of microtubular vanadium flow batteries. Our findings demonstrate that while graphite-based materials are effective for small, lab-scale batteries, they lead to high area-specific resistance (ASR) and limit scalability in larger systems. A systematic electrode selection process is outlined, identifying copper as the most promising alternative based on cost and conductivity. Copper electrodes exhibit more reversible kinetics for the anodic reaction, lower ohmic resistance, and higher current densities than graphite-based materials, ultimately leading to improved performance and scalability. However, cycling performance revealed stable operation with a slight reduction in coulombic efficiency, primarily due to the faster hydrogen evolution reaction (HER) on copper.

4.2 Methods

4.2.1 Materials

Microtubular flow batteries were made with microtubular membranes purchased from Perma Pure. The ID of the membranes used were 2.17 mm and 1.32 mm, with 254 μm and 127 μm wall thickness respectively.

Graphite materials were purchased from Ohio Carbon Blank Inc. The rods used were 1.5 mm in diameter and 15 to 20 cm in length. The OD of all graphite tubes was 0.24 in and the inner diameter (ID) ranged from 0.125 in to 0.185 in. The graphitic carbon fibers were supplied by Toray Composites (Item #: T700SC-12K-50C). The carbon fibers were heat treated before use to carbonize the polymer sizing.

Cu wires and tubes were purchased from McMaster-Carr. Two wire diameters were used, 1.64 mm and 0.5 mm with lengths ranging from 15 to 20 cm depending on the experiment. The copper tube used had 0.25 in OD and 0.18 in ID. Copper was sanded to remove surface oxides and then sonicated in ethanol before use.

4.2.2 Flow Cells

Each tubular flow battery was made using three polypropylene tee compression tube fittings (for 0.25 in. tube OD, McMaster-Carr). Fluorinated ethylene propylene (FEP) tubing (for 0.25 in. OD, McMaster-Carr) were used to house the electrolyte inside the flow cells. The graphite tubes were used as electrodes in the active section of the cell. Comparisons between Cu wire and graphite rods were conducted in membranes with diameters of 2.17 mm, while comparisons between the carbon fibers and the Cu wire were

conducted in membranes with diameter of 1.32 mm. J-B WELD Epoxy Adhesive (Grainger, Inc.) was used to seal where necessary. Teflon tape (Swagelok) was used to on the threads of the fittings. The electrolytes were circulated using two Masterflex L/S Standard Digital PTFE-Tubing Pump Systems supplied by Avantor. For the symmetric flow battery experiments the outlet of the outer flow channel was connected to the inlet of the inner flow channel and therefore one single anolyte reservoir was used. The flowrates were set at the maximum value possible to minimize mass transport limitations, since the focus of this work is the resistive losses. The maximum flowrate is limited by permeation through the graphite tube when the fluid pressure increases significantly.

4.2.3 *Electrochemical Characterization*

The electrochemical testing was performed with a Bio-Logic SP200 Potentiostat utilizing four-terminal testing to eliminate contact resistances,

Cyclic voltammetry tests were performed using a three-electrode setup. Working electrodes were Cu wires and graphite rods as described in the Materials section. The counter electrode was a 0.25 in. carbon rod and the reference electrode was Ag/AgCl in 3M NaCl (Bio-Logic). Five mL of electrolyte was used with composition 1 M H₂SO₄ (Sigma-Aldrich) and 0.1 M V³⁺ (VCl₃, 97%, Sigma-Aldrich). The solution was purged with argon before testing.

Electrochemical Impedance Spectroscopy (EIS) spectra were collected at OCV with a voltage amplitude of 10 mV and a frequency range of 200 kHz to 0.1 Hz. The high frequency x-intercept of the Nyquist plot or high-frequency resistance (HFR) was used to estimate the ohmic losses.

The polarization curves were obtained by chronoamperometry measurements. Each measurement involved applying a voltage for 1-2 minutes until current stabilization and then OCV for the same duration until the current became approximately zero. Each positive polarization voltage step was followed by a negative step of equal magnitude to minimize variations in the SOC of the electrolyte. The voltage steps were either 10 mV or 20 mV. The last current data points were collected to create the polarization curve.

Galvanostatic cycling was performed between 1.0 V and 1.6 V. The volume of electrolyte used was 6.5 mL and the composition was 1.6 M $V^{3.5+}$ with 4.25M H_2SO_4 .

4.3 Results

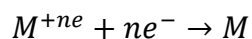
In Section 2.3.7 we showed the limitations that carbon fibers have in microtubular VRFBs in terms of high ASR and scalability. A carbon rod electrode showed lower ASR due to the higher cross-sectional area, but the ASR remained much higher than that of its parallel plate counterpart.⁴⁷ These observations, along with the analytical model's prediction (Section 0) indicated that Graphite-based electrodes do not fulfill the requirements for a high performance and scalable microtubular VRFB.

4.3.1 Anode Material Selection Process

To seek alternative materials, more suitable for microtubular VRFBs we adopted a screening approach. Material conductivity was the first property we considered, with the condition of being higher than graphite. Radioactive elements were excluded.

In Figure 4.1a we show the materials of the periodic table that are more conductive than graphite.⁷¹ The second criterion was stability in the electrolyte. We focused on

materials which can maintain their pure form, and this is possible only in the anolyte. A cathodic electrode would require a broader screening process that includes the possibility of passivation of these materials and the inclusion of alloys; however, this is beyond the scope of the current study. The stability was determined on the basis of the material's equilibrium reduction potential:



A threshold value for the equilibrium potential for these materials needs to be defined. Materials whose equilibrium potential is above the anolyte potential are expected to be stable. The potential range of the anolyte from 0.1% to 99.9% SOC is shown in Figure 4.1b. Since VRFBs are typically cycled between 20% and 80% SOC, a safe choice could be 1% SOC.⁷² This number is -0.142 V vs SHE. The elements that their equilibrium potential is above this threshold potential value are shown in Figure 4.1c.⁷³

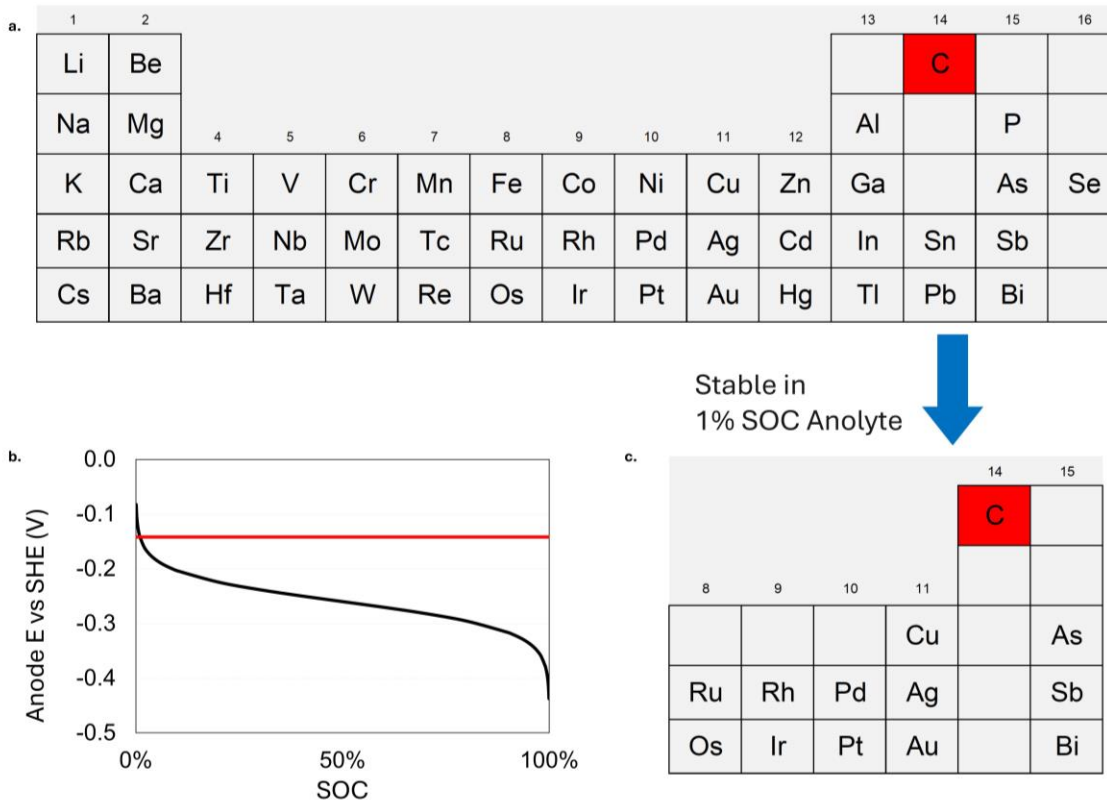


Figure 4.1 – a. The elements of the periodic table that are more conductive than graphite b. The potential of the anode as the SOC changes (black line) and the potential at 0.1% SOC (red line) c. The elements of the periodic table whose standard reduction potential is above the potential at 0.1% SOC.^{71,73,74}

Based on stability and conductivity we narrowed down the candidates to a few metalloids and transition metals. To further classify these materials, we evaluated the conductivity again while also considering the cost. Precious metals for example, even though they are highly conductive they may be too expensive for such an application, given that the ultimate goal of exploring the microtubular reactor configuration is to lower cost. In this comparison, the conductivity was evaluated based on the estimated percentage increase of the ASR. We estimated this ASR increase using an analytical model developed by Filippas et al.⁷⁵ The cost of the material was estimated in USD per m² of membrane for

a tubular membrane of 1 mm diameter and a wire electrode of 0.75 mm diameter (Table 4.1).

To obtain a more tangible metric of the effect of the material conductivity on the performance, we estimated the percentage increase of the ASR for a reactor of 50 cm length compared to one of infinitely small length where the electrode resistance has no practical contribution to the ASR. For this estimation we used Eq. (63) assuming a highly conductive outer electrode ($K_r \rightarrow \infty$), membrane and inner electrode dimensions the same as the ones used for the cost estimates (Table 4.1):

$$\frac{ASR}{ASR_{min}} = v \coth(v) \quad (81)$$

Where:

$$v = \frac{L}{\sqrt{\sigma_1}} \sqrt{\frac{2r_s}{ASR_{min}r_1^2}} \quad (82)$$

The kinetic, electrolyte, and separator resistance appear in the parameter ASR_{min} which is assumed to be $1 \Omega \text{ cm}^2$ due to the lack of literature data for the kinetic resistance of all these materials.

Figure 4.2 shows the cost and the ASR increase combined. We see that Cu, Ag, and Au show negligible increase in the ASR, followed by the platinum-group metals. All these materials, most of which are precious metals, have significantly high costs with only Cu

having a very low cost due to its high availability. The metalloids are also low cost, however, their ASR at 50 cm is more than double the initial ASR.

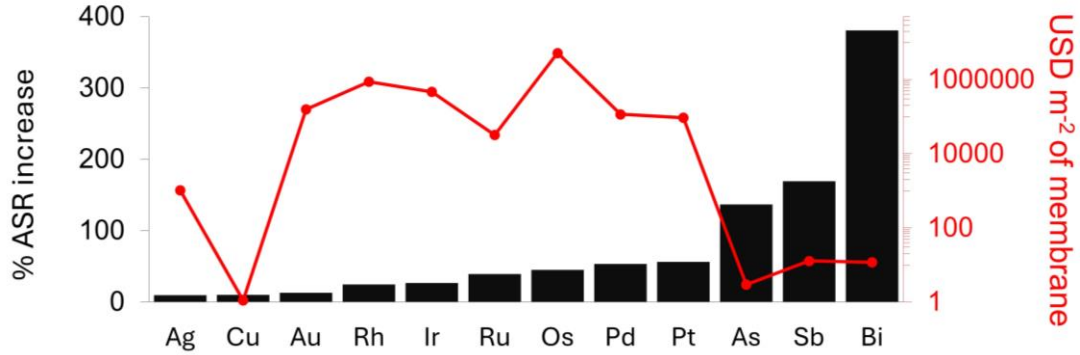


Figure 4.2 - The percentage ASR increase from a infinitesimally short electrode to a 50 cm electrode and the cost of the electrode material.⁷⁶

Table 4.1 – Parameters used in the estimation of the ASR of a 50 cm long electrode.

Parameter	Value	Units
r_1	0.75	mm
r_s	1.00	mm
L	50	cm
ASR_{min}	1	$\Omega \text{ cm}^2$

Last and foremost are the kinetic properties of these materials. The dominance of graphite-based electrodes in the parallel plate cells has left most other materials unexplored.⁷⁷⁻⁷⁹ Non-carbon materials have been mainly implemented as catalysts deposited on a graphite-based materials rather than electrodes themselves.^{48,80,81} Among the materials that have passed the previous criteria, Ag and Cu have been studied as nanoparticles deposited on graphite felts.^{82,83} The metalloids, especially Bi, have also been studied as catalysts, however their conductivity seems to be low for the microtubular design

(Figure 4.2).⁸⁴⁻⁸⁷ These materials that are good catalysts but not good enough conductors could be used as coatings on a more conductive but less catalytically active material to create an effective “composite” electrode.

Based on all these criteria, Cu seems to be the most promising option in terms of scalability and cost. It needs to be determined whether the theoretical estimates for its scalability are valid and whether it is a good enough catalyst towards the anodic reaction. To examine the kinetic properties, we used a graphite rod and a copper wire. In Figure 4.3a we compared the cyclic voltammograms of the two materials. The CVs contained three key features: a vanadium peak at around -500 mV, HER peaks below -800 mV, and copper dissolution-deposition peaks between -200 mV and 0. The vanadium reaction regime was further studied with the Laviron method (Figure 4.3b,c).⁸⁸ CVs were obtained at different scan rates and the peak separation was recorded. The peak separation for copper was significantly smaller than that of graphite indicating higher reversibility (Figure 4.3b). With the increasing scan rate, the peak separation increased for both materials which is a sign of quasi-reversible kinetics (Figure 4.3b,c). The slope of the peak separation and the logarithm of the scan rate is inversely proportional to the kinetic constant of the reaction.^{89,90} As a result, the copper wire that exhibited the smaller slope is expected to exhibit faster kinetics towards the anodic vanadium reaction.

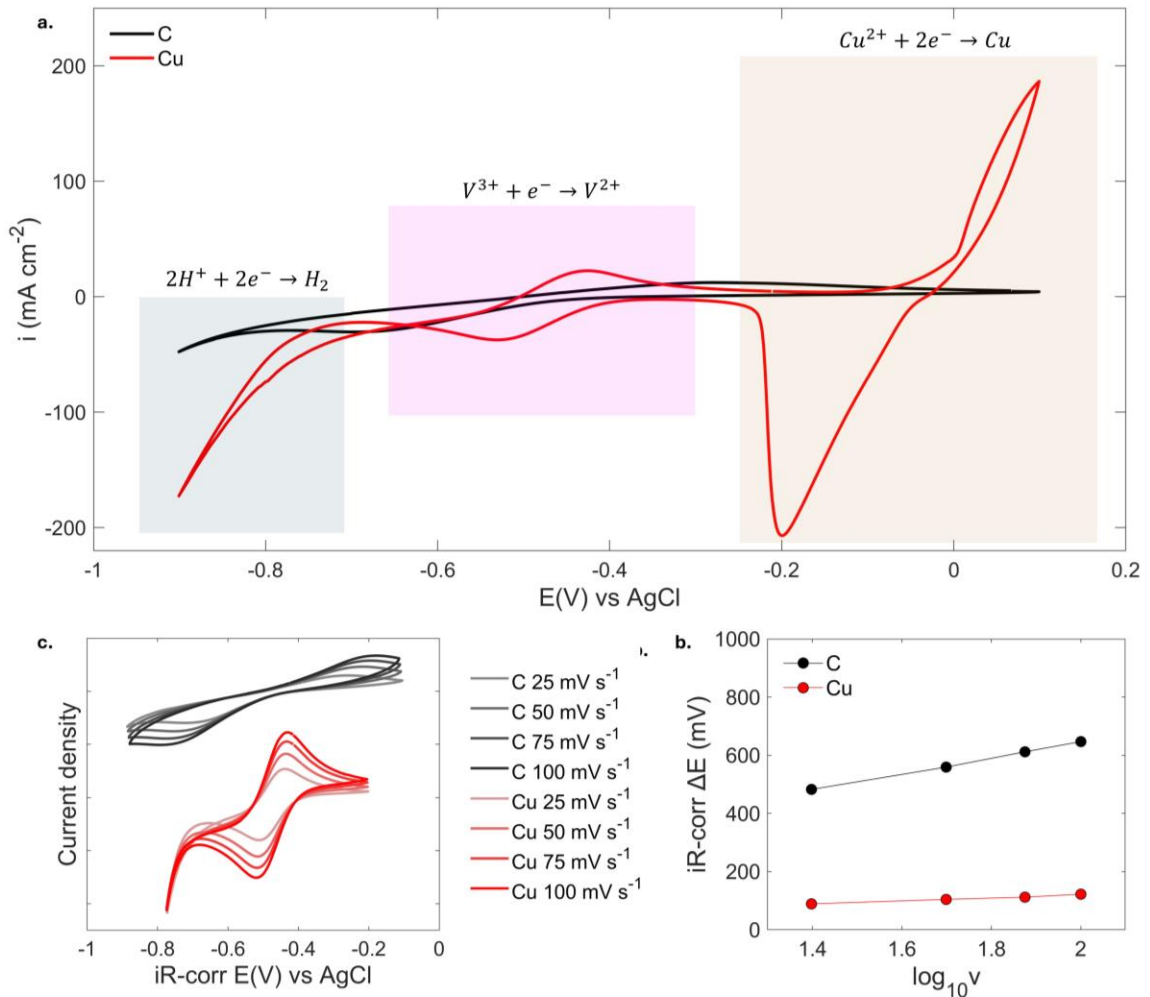


Figure 4.3 – a. Cyclic voltammograms of Cu wire and graphite rod in V^{3+} solution at 50 $mV s^{-1}$ in a wide potential range showing all possible reactions b. Cyclic voltammograms of Cu wire and graphite rod at 25, 50, 75, and 100 $mV s^{-1}$ targeting the potential range that the anodic vanadium reaction occurs c. The peak separation for the two samples at each scan rate plotted against the logarithm of the scan rate.

In a realistic setup, the stability of copper depends on the actual concentration of Cu^{2+} ions in the solution. According to our supplier's datasheet, the Cu^{2+} concentration was no more than 8 μM , which corresponds to an equilibrium potential of 0.18 V vs SHE—still significantly higher than the potential of the anolyte at 1% SOC (-0.142 V vs SHE).

However, this contradicts the general aim of maintaining the lowest possible Cu concentration in VRFB electrolytes, since copper ions are known to lead to parasitic hydrogen generation in planar cells.^{91,92} In this tubular reactor, the electrode itself is made of copper; therefore, the Cu²⁺ concentration in the electrolyte needs to be sufficiently high to ensure electrode stability in V³⁺ or even V^{3.5+} solutions, which compromises the stringent requirements of VRFB electrolyte composition.

While the use of copper may lead to lower coulombic efficiency and faster oxidation state imbalance due to copper dissolution, it could also allow for the use of a potentially lower-cost electrolyte where copper purification steps are unnecessary. Addressing this dilemma would require a holistic techno-economic analysis that considers all these factors.

4.3.2 *Copper Anode and Graphite Anode VRFB Full-Cell Testing*

Moving on from the three electrode tests to battery performance, we compared the full cell performance of a flow battery with a copper anode and a flow battery with graphite anode (Figure 4.4a,b). Figure 4.4c shows the EIS of these two batteries, showing significantly lower ASR_{HFR} for the copper battery. The same conclusion was supported by the polarization curves of the two flow batteries, with the graphite anode having a higher slope than the copper one (Figure 4.4d). The current densities achieved by the flow battery with the copper anode were noticeably higher than the graphite with mass transport eventually taking over at high polarizations. Plotting the iR-free polarization curve (current-voltage curve with the voltage corrected for the ohmic overpotential through the ASR) we observed that copper has a significantly smaller ohmic overpotential (Figure 4.4e). In Figure 4.4f, the overpotential breakdown at 10 mA cm⁻² shows that copper

decreases the ohmic overpotential from 32 mV to 11 mV and the kinetic overpotential by 34 mV (assuming same mass transport overpotential). Overall, the use of copper had a dual effect on the performance by decreasing both the ohmic and kinetic overpotentials.

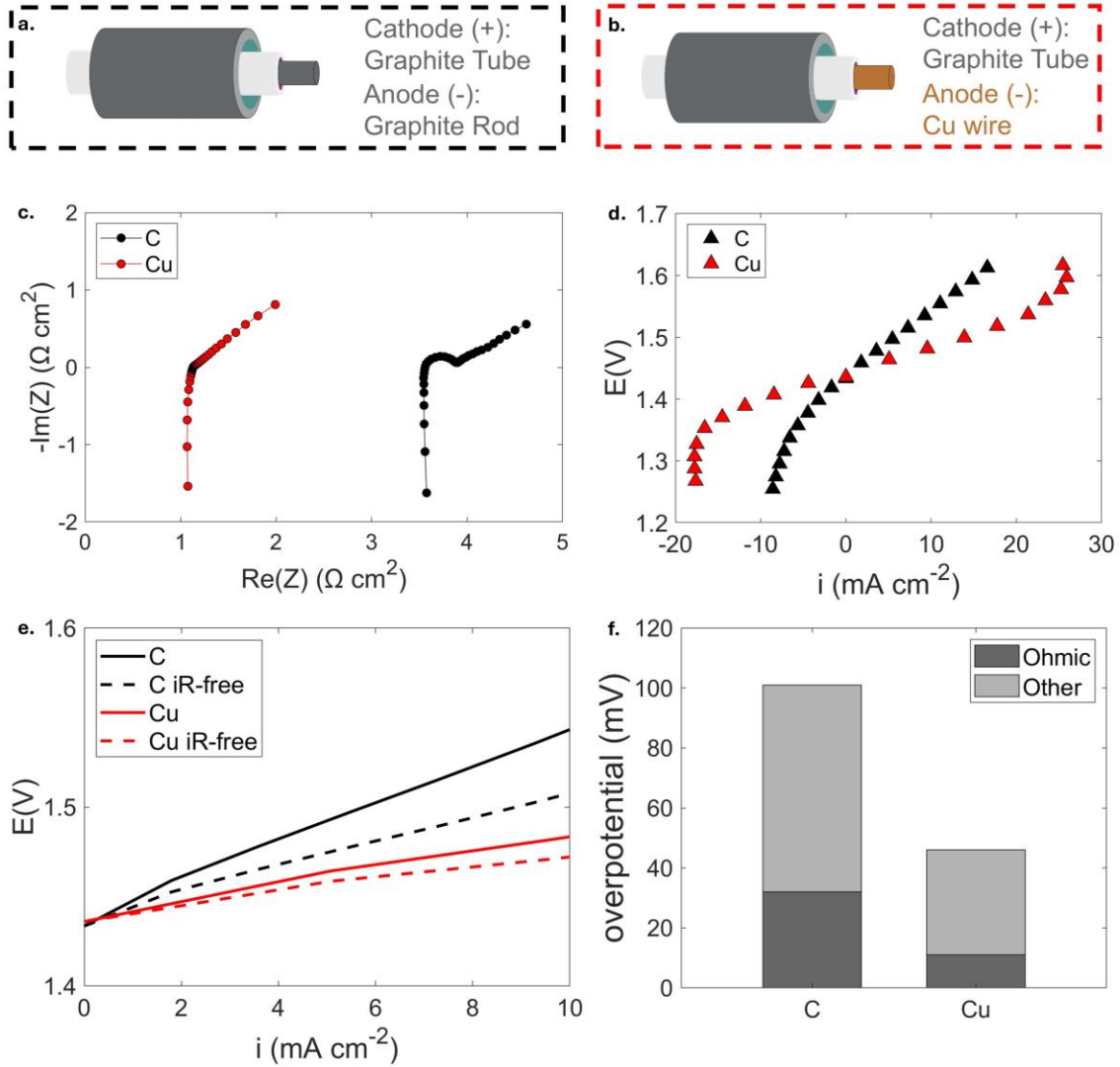


Figure 4.4 – Schematics of a. the graphite-anode flow battery configuration and b. the copper-anode flow battery c. EIS spectra and d. Polarization curves of the VRFBs with Cu and the graphite anodes e. The polarization curve along with the iR -free polarization curve f. Overpotential breakdown into ohmic and non-ohmic(kinetic and mass transport) at 10 mA cm^{-2} . The flowrates of the inner and outer flow channel were 10 mL min^{-1} and 25 mL min^{-1} respectively.

4.3.3 Scalability Comparison of Half-Cell Symmetric Flow Batteries

One of the key arguments made in this work was that more conductive materials would improve the scalability of the microtubular design. To validate this argument, we used symmetric flow batteries, with both electrodes made of copper or both electrodes made of graphite (Figure 4.5a). The experiments were done with analyte flowing in both flow channels. Two all-copper flow batteries were made, one 5cm long and one 10 cm long and their EIS spectra were collected. The increase in the HFR was plotted in Figure 4.5b. The same experiments were done for the all-graphite flow batteries. The ASR of the copper batteries did not increase with length, in contrast to the all-graphite batteries which showed a doubling with increased length. These experiments showed the critical roll of the electrode material in the scalability of the microtubular design.

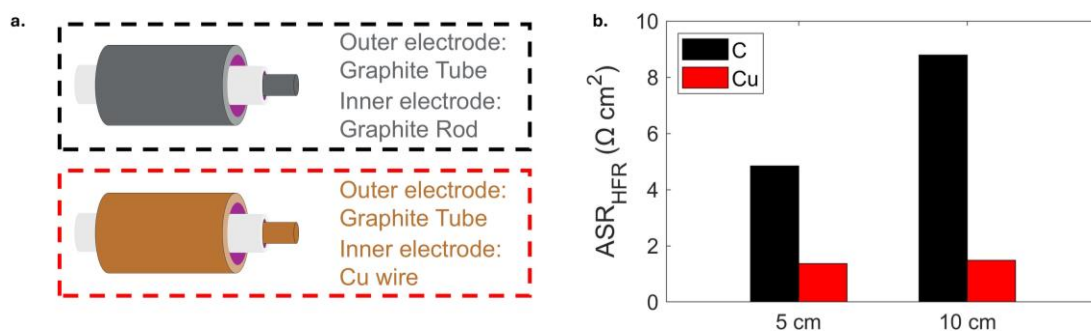


Figure 4.5 – a. Schematic of the symmetric batteries b. Comparison of the ASR increase over length for copper and graphite symmetric batteries. The flowrates was 15 mL min⁻¹.

4.3.4 Full-Cell Cycling Performance Comparison of Copper and Graphite Anode

Figure 4.6a shows cycling performance data for the batteries in Figure 4.4b. Cycling was performed at 3 mA cm⁻² between 1.0 V and 1.6 V. The coulombic efficiency was lower for the copper-based battery, possibly due to the higher hydrogen evolution rate (Figure

4.6b). The low overall CE observed is likely due to the high crossover caused by the 8hr cycling duration. Lab-scale planar cells show similar behavior, reaching 90% or lower CE at 4hr cycles.^{67,93} The reduced ohmic and kinetic overpotentials of the copper-based battery, as shown in Figure 4.4f, led to a higher voltage efficiency (Figure 4.6c). The energy efficiency, being the product of the coulombic and the voltage efficiency, was lower for the copper-based electrode which indicates that the parasitic reactions offset the benefit of lower ohmic losses (Figure 4.6d).

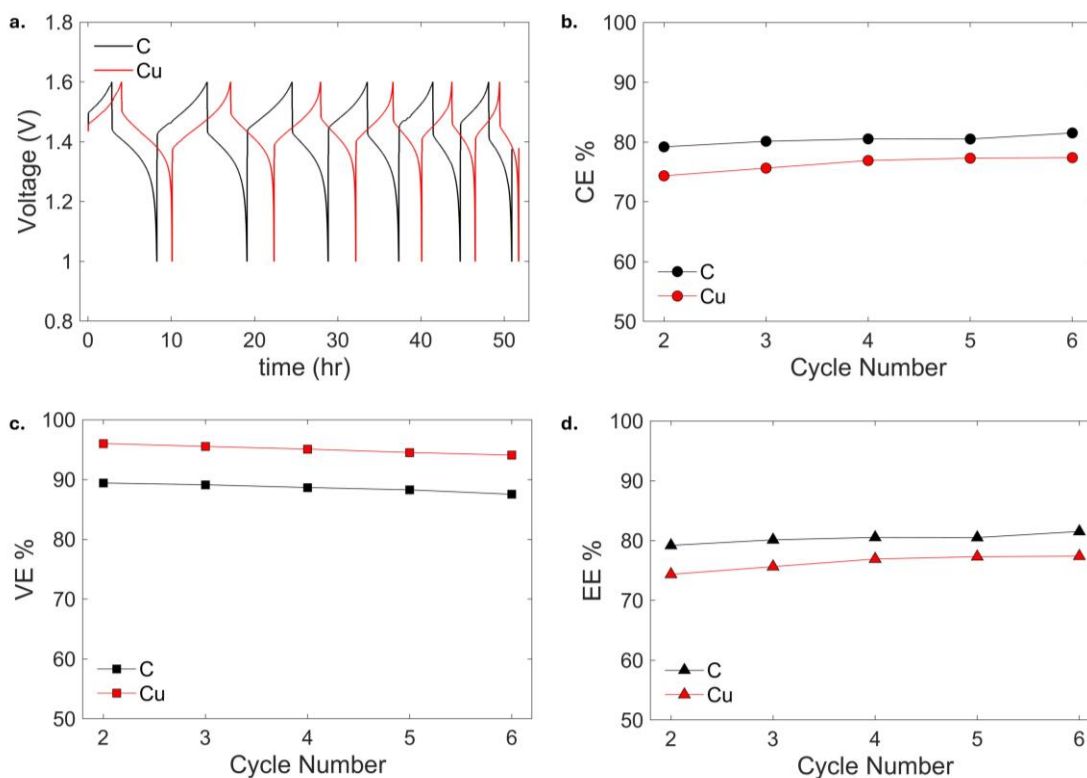


Figure 4.6 – a. Full cell cycling data at 3 mA cm⁻² for two flow batteries, one with copper anode and one with graphite anode b. Coulombic efficiency c. Voltage efficiency and d. Energy Efficiency comparison for the 2nd to the 6th cycle. The flowrates were 9 mL min⁻¹ and 18 mL min⁻¹ in the inner and outer electrode respectively

4.3.5 Microtubular Copper and Carbon Fiber-based Anode Full-Cell Testing

The last comparison was focused on testing smaller membranes, of 1.3 mm ID. At this size it becomes more challenging to find suitable inner or anodic electrodes. Graphite rods of such diameter are difficult to extrude, and even if they can be extruded, they would be quite brittle; therefore, carbon fibers are a better option (Figure 4.7a). For copper it is straightforward to find wires with 0.5 mm diameter or even smaller which allow the membrane size to go below 1 mm (Figure 4.7b). In Figure 4.7c,d we show the performance of these two flow batteries with carbon fibers and Cu wire as anodic electrodes. The EIS spectra showed a significantly lower ohmic resistance for the Cu wire, attributed to its higher conductivity (Figure 4.7c). Similarly, Cu can reach higher current densities under polarization, with a smaller slope in its linear region (Figure 4.7d). Mass transport limitations, however, appeared even at low current densities due to the lower available surface area. Overall, these experiments demonstrated the higher potential of Cu based anodes in microtubular flow batteries, offering lower ohmic losses, and improving scalability with reversible kinetics towards the anodic reaction of VRFBs.

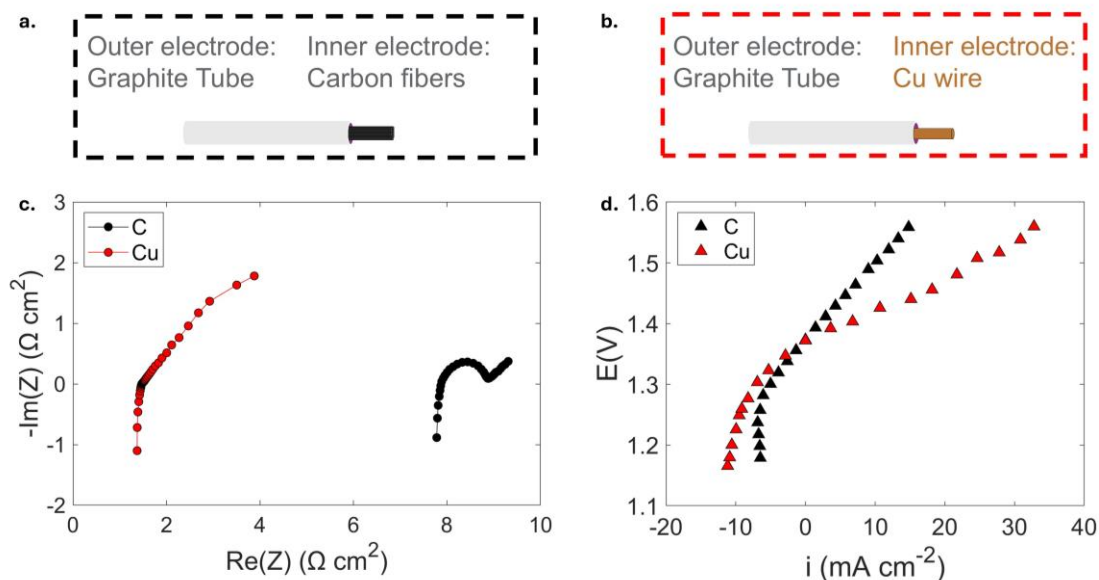


Figure 4.7 – Schematic of a microtubular VRFB with a. carbon fibers as anode b. copper wire as anode c. EIS and d. polarization curve comparison of these two batteries. The flowrates of the inner and the outer flow channels were 10 mL min^{-1} and 20 mL min^{-1} .

4.4 Conclusions

This work demonstrated that bare copper is a scalable, cost effective, and high-performance anode material for microtubular flow batteries. Copper was rationally selected out of all the materials of the periodic table for its unique combination of low cost, high conductivity and stability in the anolyte of VRFBs. Cyclic voltammetry (CV) and full-cell tests confirmed that copper not only exhibits favorable kinetic properties for the anodic reaction but also significantly reduces ohmic resistance, improving overall performance. Symmetric cell tests further validated copper's scalability by showing a negligible increase in ASR with length. Graphite showed higher coulombic efficiency in cycling tests, likely due to reduced hydrogen evolution. This research challenges the conventional reliance on graphite and introduces copper as an alternative for microtubular VRFBs. These findings

suggest that copper could play a crucial role in developing scalable microtubular flow batteries.

CHAPTER 5. CONCLUSIONS AND FUTURE DIRECTIONS

5.1 Conclusions

This thesis has explored the performance, scalability, and electrochemical behavior of microtubular VRFBs, focusing on key factors such as the ohmic resistance, the electrode configuration, and the material selection. Through a combination of experimental assessments, analytical modelling, and numerical simulations, this research has provided important insights into the challenges and opportunities for advancing microtubular VRFBs and tubular electrochemical reactors in general.

The initial investigation revealed that ohmic losses significantly limit the performance of microtubular VRFBs. By studying the effects of electrode conductivity and configuration, it was demonstrated that the conductivity of the electrode and the uniformity of the current distribution in the electrolyte play a key role in the ohmic resistance of the battery. Although the coaxial configuration led to a lower areal resistance, numerical simulations showed that it may lead to a higher volumetric resistance, suggesting that a quasi-coaxial configuration may be a better alternative. These results emphasized the need to carefully consider areal and volumetric performance in flow battery design, particularly when scaling up from single-tubular to multi-tubular configurations.

Experiments showing an increased ASR with increasing battery length raised the need for a deeper understanding of the tubular reactor behavior. An analytical model was developed to study the current distribution and the ASR scaling of tubular reactors. The model highlighted the impact of electrode geometry and material properties on current

distribution, electrode utilization, and overall reactor efficiency. Key dimensionless parameters were identified that dictate the current distribution and the reactor resistance. A strong dependence of the ASR on electrode material conductivity was revealed, emphasizing the need for careful material selection for tubular reactors. This model can serve as a valuable tool for preliminary design assessment, providing foundational understanding that can be used to optimize tubular reactors.

Building upon the insights from the model, the final experimental phase of the thesis introduced bare copper as a promising anode material for microtubular VRFBs. Copper was selected for its low cost, high conductivity, and stability in the anolyte, and it demonstrated superior scalability compared to graphite. Cyclic voltammetry (CV) and full-cell tests confirmed copper's favorable kinetic properties and its ability to reduce ohmic resistance. While graphite exhibited better coulombic efficiency, copper's scalability and conductivity offer a significant advantage for larger-scale applications. These findings challenge the conventional use of graphite-based materials in microtubular configurations and suggest that copper could play a pivotal role in advancing scalable microtubular VRFB systems.

At this stage of flow battery development, it is useful to compare the tubular VRFB field with past tubular reactor development efforts in fuel cells (See 1.3). Similar to tubular hydrogen and solid oxide fuel cells, tubular VRFBs exhibit lower areal performance compared to planar cells. The longer current collection paths remain a challenge of the tubular geometry, as both experiments and modeling in this thesis have shown. Highly conductive electrodes, such as copper, can be used to mitigate resistive losses, as we demonstrated in Chapter 4. Unlike tubular fuel cells, tubular flow batteries, especially with

wire electrodes, have significantly less complex cell fabrication, which could be a strong advantage. The cathodic electrode in a VRFB needs to meet corrosion resistance requirements that are potentially more stringent than those for fuel cell electrodes due to the highly corrosive environment at the cathode.

In summary, this thesis contributes to the field of electrochemical reactor design by offering insight and addressing key challenges in microtubular flow reactors for VRFBs. By optimizing electrode configurations, developing analytical tools, and proposing new materials, this work significantly boosts microtubular flow battery performance and paves the way for further research and development of scalable, high performance, and cost-effective tubular flow reactors (Figure 5.1). The insights gained here can facilitate the development of next-generation energy storage solutions, crucial for the growing demand for renewable energy integration.

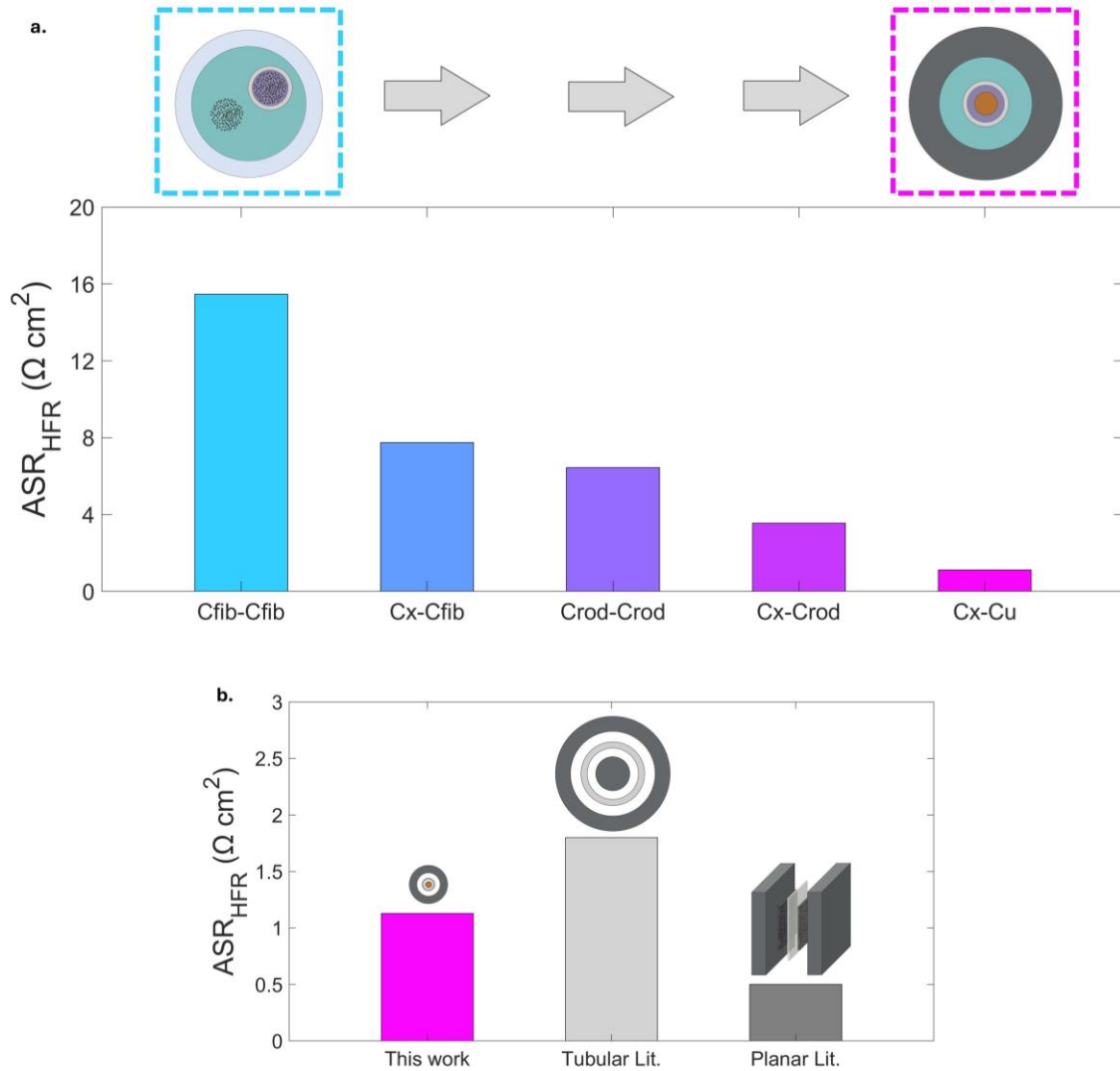


Figure 5.1 – a. Evolution of ASR over the design generations in this thesis b. Comparison of the ASR of the final microtubular flow battery with a Cu-based anode, the best tubular flow battery performance in the literature along with a typical parallel plate flow battery ASR.^{18,47}

5.2 Future Work

This thesis provides a foundational understanding of the phenomena governing microtubular flow battery ohmic losses and performance; however, there are still questions to be answered to holistically assess the potential of this reactor configuration. From this work we showed that the tubular configuration has a potential for higher volumetric

performance than the planar in a multi-tubular configuration. Before scaling up, however, the single-tubular configuration needs to be fully understood and optimized. At the current state of this reactor geometry, there are challenges compared to the planar due to the longer electron conduction pathways which manifest as higher ohmic losses. Potential advantages could appear in transport related losses since tubular configurations are known to improve heat and mass transport in other technologies (heat exchangers, hollow-fiber modules).

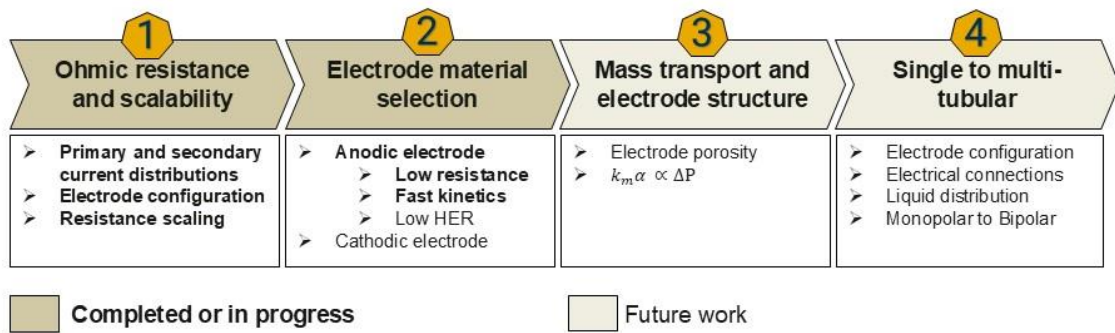


Figure 5.2 - Outline of completed and future work to be done.

5.2.1 Anode Coulombic Efficiency Improvements

The use of copper significantly reduces ohmic losses and enhances the scalability of the microtubular flow battery. However, the lower coulombic efficiency indicates that side reactions are more severe on copper compared to graphite, which impacts the energy efficiency (Figure 4.6). One approach to address this issue is to use a coated wire. The coating needs to be made of a material that catalyzes the anodic reaction while suppressing HER. A carbon-based coating, such as a slurry of carbon nanoparticles or other carbon materials, may be a suitable option. In fact, preliminary experiments have shown that it is possible to coat a copper wire with a slurry of carbon black powder (Super P) (Figure 5.3). Other possible pathways would be to coat, electrodeposit, or sputter the surface of the core

wire with a different metal that can act as an electrocatalyst and suppress HER. Similar approaches have been widely used in conventional planar VRFBs to improve kinetics and suppress HER with metals such as Bi and Sb.^{87,94}

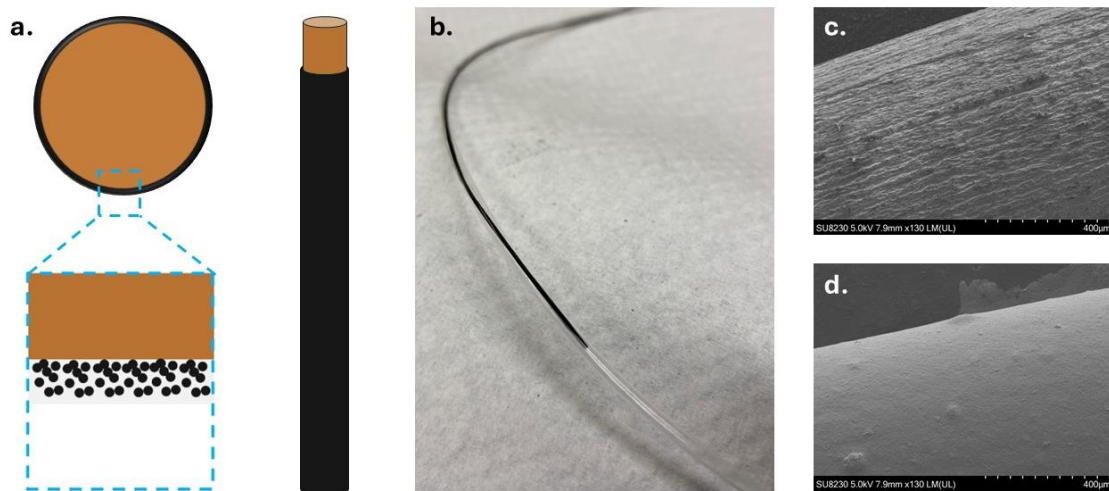


Figure 5.3 – a. Schematic of slurry coated Cu wire b. Picture of a coated wire inside a hollow fiber membrane. SEM picture of c. Bare wire d. Slurry coated wire

5.2.2 Cathode Electrode Design

While a highly conductive anode improves scalability, the graphite-based cathode may eventually become a bottleneck as reactor length increases. Already the flow battery in Figure 4.4b has a K_r of approximately 0.02 which means that the copper wire is 50 times more conductive than the graphite tube. This conductivity difference can lead to a non-uniform current distribution and drive an increase in ASR with length. Whether a tube or wire outer electrode is used, it needs to be equally conductive as the anode, stable, and catalytically active towards the V(IV)/V(V) reaction. Guided by studies in planar VRFBs, several transition and post-transition metal oxides exhibit good stability and catalytic properties towards the cathodic reaction. Examples include TiNb_2O_7 , ZrO_2 , Ta_2O_5 , Nb_2O_5 , Cr_2O_3 , MoO_3 , WO_3 , Mn_3O_4 , CoO , NiO , PbO_2 , SnO_2 .^{95–106} These oxides, however, may

not be conductive enough. In such cases, a hybrid electrode could be used, with the core being a highly conductive material and the surface modified or coated with one of these materials.

5.2.3 Mass Transport Investigation

The thesis focused on understanding the effect of ohmic resistance. Mass transport is naturally the next step towards performance improvements. As can be seen in Figure 4.4d and Figure 4.7d, at high polarization the current density reaches a maximum value and it does not increase further. This maximum current density occurs when the reactants are depleted on the surface of the electrode and it is called the limiting current density, i_L :

$$i_L = nF \frac{\alpha}{a_m} k_m C \quad (83)$$

Where α , a_m the surface area per unit volume of the electrode and the membrane respectively, k_m the mass transport coefficient to the electrode surface, and C and concentration of the reactant in the bulk of the electrolyte. A starting point to increase the limiting current of the tubular batteries would be to increase the specific surface area of the electrode. This could be achieved by replacing the single wire electrode with a multiwire electrode, such as a bundle or a braided electrode, to increase electrode surface area per unit volume and increase the limiting current of the flow battery.¹⁰⁷ The structure of the electrode and the mass transport coefficient expected with its structure can be investigated using both experiments and modelling. The analytical model developed in this thesis is limited to the secondary current distributions leaving numerical simulations as the most accurate way to study mass transport and tertiary current distributions.^{108,109}

$$\alpha = \frac{\text{Electrode surface area}}{\text{Inner flow channel volume}}$$

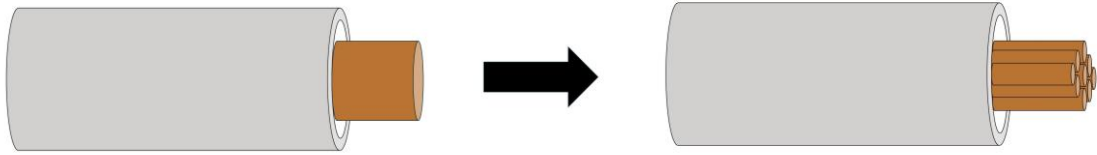


Figure 5.4 – Increasing electrode surface area by using bundled wires.

REFERENCES

1. R. Xia, S. Overa, and F. Jiao, *JACS Au*, **2**, 1054–1070 (2022).
2. S. Xin et al., *Sci. China Chem.*, **67**, 13–42 (2024).
3. T. Noël, Y. Cao, and G. Laudadio, *Acc. Chem. Res.*, **52**, 2858–2869 (2019).
4. F. C. Walsh and C. Ponce de León, *Electrochimica Acta*, **280**, 121–148 (2018).
5. L. F. Arenas, C. Ponce de León, and F. C. Walsh, *Journal of Energy Storage*, **11**, 119–153 (2017).
6. C. V. Pham, D. Escalera-López, K. Mayrhofer, S. Cherevko, and S. Thiele, *Advanced Energy Materials*, **11**, 2101998 (2021).
7. D. R. Dekel, *Journal of Power Sources*, **375**, 158–169 (2018).
8. O. Gröger, H. A. Gasteiger, and J.-P. Suchsland, *J. Electrochem. Soc.*, **162**, A2605 (2015).
9. F. C. Walsh and G. W. Reade, in *Studies in Environmental Science*, Environmental Oriented Electrochemistry. C. A. C. Sequeira, Editor, vol. 59, p. 3–44, Elsevier (1994) <https://www.sciencedirect.com/science/article/pii/S0166111608705466>.
10. S. C. Perry, C. P. de León, and F. C. Walsh, *J. Electrochem. Soc.*, **167**, 155525 (2020).
11. N. Yamada, T. Yaguchi, H. Otsuka, and M. Sudoh, *J. Electrochem. Soc.*, **146**, 2587 (1999).
12. A. Tschöpe, M. Wyrwoll, M. Schneider, K. Mandel, and M. Franzreb, *Chemical Engineering Journal*, **385**, 123845 (2020).
13. S. A. Martínez-Delgadillo, J. Ramírez-Muñoz, H. R. Mollinedo, O. M. Huerta, C. Barrera-Diaz, and V. X. Mendoza-Escamilla, *International Journal of Electrochemical Science*, **8**, 3939–3952 (2013).
14. H. V. Parys, E. Tourwé, T. Breugelmans, M. Depauw, J. Deconinck, and A. Hubin, *Journal of Electroanalytical Chemistry*, **622**, 44–50 (2008).
15. *Energy.gov* <https://www.energy.gov/eere/analysis/2022-grid-energy-storage-technology-cost-and-performance-assessment>.

16. Y. Wu, F. Zhang, T. Wang, P.-W. Huang, A. Filippas, H. Yang, Y. Huang, C. Wang, H. Liu, X. Xie, R. P. Lively, and N. Liu, *Proceedings of the National Academy of Sciences*, **120**, e2213528120 (2023).
17. S. Ressel, A. Laube, S. Fischer, A. Chica, T. Flower, and T. Struckmann, *Journal of Power Sources*, **355**, 199–205 (2017).
18. S. Ressel, P. Kuhn, S. Fischer, M. Jeske, and T. Struckmann, *Journal of Power Sources Advances*, **12**, 100077 (2021).
19. A. Laube, A. Hofer, B. Sánchez Batalla, S. Ressel, A. Chica, S. Fischer, C. Weidlich, J. Bachmann, and T. Struckmann, *International Journal of Hydrogen Energy*, **47**, 15943–15951 (2022).
20. Z.-G. Shao, W.-F. Lin, F. Zhu, P. A. Christensen, H. Zhang, and B. Yi, *Journal of Power Sources*, **160**, 1003–1008 (2006).
21. K. Huang and S. C. Singhal, *Journal of Power Sources*, **237**, 84–97 (2013).
22. K. I. Lee, S. W. Lee, M. S. Park, and C. N. Chu, *International Journal of Hydrogen Energy*, **35**, 11844–11854 (2010).
23. A. Laube, B. Sánchez Batalla, C. Weidlich, A. Hofer, J. Bachmann, S. Zallmann, C. Körner, S. Fischer, A. Chica, and T. Struckmann, *International Journal of Hydrogen Energy*, **49**, 437–448 (2024).
24. R.-J. Yu, G.-Y. Cao, X.-Q. Liu, Z.-F. Li, W. Xing, and X.-J. Zhu, *Journal of Fuel Cell Science and Technology*, **4**, 520–524 (2006).
25. M. C. Bermúdez Agudelo, M. Hampe, T. Reiber, and E. Abele, *Materials*, **13**, 2096 (2020).
26. S. R. Suseendiran, S. Pearn-Rowe, and R. Rengaswamy, *International Journal of Hydrogen Energy*, **45**, 10549–10558 (2020).
27. S. S. Ravichandran, G. Mohandass, A. C. Bhosale, R. Rengasamy, R. Ramkumar, and S. R. Choudhury, in, p. 119–126, Atlantis Press (2021) <https://www.atlantispress.com/proceedings/ires-20/125952212>.
28. M. C. Bermúdez Agudelo and M. J. Hampe, *Electrochemical Science Advances*, **3**, e2100193 (2023).
29. S. K. Sethy and A. C. Bhosale, *Journal of Power Sources*, **600**, 234258 (2024).
30. R. Chen, Y. Gao, J. Gao, H. Zhang, M. Motola, M. B. Hanif, and C.-X. Li, *Journal of Energy Chemistry*, **97**, 79–109 (2024).

31. T. Alston, K. Kendall, M. Palin, M. Prica, and P. Windibank, *Journal of Power Sources*, **71**, 271–274 (1998).
32. V. Lawlor, S. Griesser, G. Buchinger, A. G. Olabi, S. Cordiner, and D. Meissner, *Journal of Power Sources*, **193**, 387–399 (2009).
33. K. Kendall, *Int J Applied Ceramic Tech*, **7**, 1–9 (2010).
34. S. M. Jamil, M. H. D. Othman, M. A. Rahman, J. Jaafar, A. F. Ismail, and K. Li, *Journal of the European Ceramic Society*, **35**, 1–22 (2015).
35. C. Stolze, T. Janoschka, J. Winsberg, M. Strumpf, M. D. Hager, and U. S. Schubert, *Energy Technology*, **6**, 2296–2310 (2018).
36. M. Bartolozzi, *Journal of Power Sources*, **27**, 219–234 (1989).
37. M. Skyllas-Kazacos, M. H. Chakrabarti, S. A. Hajimolana, F. S. Mjalli, and M. Saleem, *J. Electrochem. Soc.*, **158**, R55 (2011).
38. L. F. Arenas, C. P. de León, and F. C. Walsh, *J. Electrochem. Soc.*, **167**, 023504 (2020).
39. A. Forner-Cuenca and F. R. Brushett, *Current Opinion in Electrochemistry*, **18**, 113–122 (2019).
40. Z. Rhodes, J. R. Cabrera-Pardo, M. Li, and S. D. Minteer, *Israel Journal of Chemistry*, **61**, 101–112 (2021).
41. Imre Gyuk, M. Johnson, J. Vetrano, K. Lynn, W. Parks, R. Handa, L. Kannberg, S. Hearne, K. Waldrip, and R. Braccio, *Grid Energy Storage*, U.S. Department of Energy, (2013).
42. A. Frazier, W. Cole, P. Denholm, S. Machen, N. Gates, and N. Blair, *Storage Futures Study: Economic Potential of Diurnal Storage in the U.S. Power Sector*, (2021), p. NREL/TP-6A20-77449, 1785688, MainId:27385
<https://www.osti.gov/servlets/purl/1785688/>.
43. B. Li and J. Liu, *National Science Review*, **4**, 91–105 (2017).
44. M. L. Perry, K. E. Rodby, and F. R. Brushett, *ACS Energy Lett.*, **7**, 659–667 (2022).
45. C. Minke and T. Turek, *Journal of Power Sources*, **376**, 66–81 (2018).
46. P. Alotto, M. Guarnieri, and F. Moro, *Renewable and Sustainable Energy Reviews*, **29**, 325–335 (2014).
47. D. S. Aaron, Q. Liu, Z. Tang, G. M. Grim, A. B. Papandrew, A. Turhan, T. A. Zawodzinski, and M. M. Mench, *Journal of Power Sources*, **206**, 450–453 (2012).

48. A. Parasuraman, T. M. Lim, C. Menictas, and M. Skyllas-Kazacos, *Electrochimica Acta*, **101**, 27–40 (2013).
49. T. F. Fuller and J. N. Harb, *Electrochemical engineering*, First edition., p. 1, Wiley, Hoboken, NJ, USA, (2018).
50. M. Skyllas-Kazacos, L. Cao, M. Kazacos, N. Kausar, and A. Mousa, *ChemSusChem*, **9**, 1521–1543 (2016).
51. D. Chen, M. A. Hickner, E. Agar, and E. C. Kumbur, *Journal of Membrane Science*, **437**, 108–113 (2013).
52. F. F. Rivera, T. Pérez, L. F. Castañeda, and J. L. Nava, *Chemical Engineering Science*, **239**, 116622 (2021).
53. J. Martinez Lopez, I. Aramendia, U. Fernandez-Gamiz, E. Sanchez-Diez, A. Beloki, E. Kurt, and J. M. Lopez-Guede, *JOM*, **76**, 130–140 (2024).
54. X. Ke, J. M. Prah, J. I. D. Alexander, and R. F. Savinell, *Journal of Power Sources*, **384**, 295–302 (2018).
55. Y. Chen, Z. Xu, C. Wang, J. Bao, B. Koepfel, L. Yan, P. Gao, and W. Wang, *Journal of Power Sources*, **482**, 228817 (2021).
56. D. Bhattacharyya, R. Rengaswamy, and C. Finnerty, *Chemical Engineering Science*, **62**, 4250–4267 (2007).
57. L. Li, G. Nikiforidis, M. K. H. Leung, and W. A. Daoud, *Applied Energy*, **177**, 729–739 (2016).
58. M. A. R. S. Al-Baghdadi, *Proceedings of the Institution of Mechanical Engineers, Part A: Journal of Power and Energy*, **222**, 569–585 (2008).
59. M. S. Celtek and T. Demircan, *Global Challenges*, **7**, 2300096 (2023).
60. J. M. Sierra, S. J. Figueroa-Ramírez, S. E. Díaz, J. Vargas, and P. J. Sebastian, *International Journal of Hydrogen Energy*, **39**, 16694–16705 (2014).
61. S. Modekurti, B. Bullocks, D. Bhattacharyya, and R. Rengaswamy, *Ind. Eng. Chem. Res.*, **51**, 5003–5010 (2012).
62. A. D. Villalobos-Lara, T. Pérez, A. R. Uribe, J. A. Alfaro-Ayala, J. de J. Ramírez-Minguela, and J. I. Minchaca-Mojica, *Journal of Electroanalytical Chemistry*, **858**, 113807 (2020).
63. J. S. Newman and C. W. Tobias, *J. Electrochem. Soc.*, **109**, 1183 (1962).
64. J. Newman and W. Tiedemann, *AIChE Journal*, **21**, 25–41 (1975).

65. F. Incropera, D. DeWitt, T. Bergman, and A. Lavine, *Fundamentals of Heat and Mass Transfer*, 8th ed., John Wiley & Sons, (2018).
66. C.-N. Sun, F. M. Delnick, D. S. Aaron, A. B. Papandrew, M. M. Mench, and T. A. Zawodzinski, *ECS Electrochem. Lett.*, **2**, A43 (2013).
67. B. Jiang, L. Wu, L. Yu, X. Qiu, and J. Xi, *Journal of Membrane Science*, **510**, 18–26 (2016).
68. S. P. Ressel, thesis, Universitat Politècnica de València, Valencia (Spain) (2019) <https://riunet.upv.es/handle/10251/131203>.
69. F. Mo, G. Liang, Z. Huang, H. Li, D. Wang, and C. Zhi, *Advanced Materials*, **32**, 1902151 (2020).
70. J. He, C. Lu, H. Jiang, F. Han, X. Shi, J. Wu, L. Wang, T. Chen, J. Wang, Y. Zhang, H. Yang, G. Zhang, X. Sun, B. Wang, P. Chen, Y. Wang, Y. Xia, and H. Peng, *Nature*, **597**, 57–63 (2021).
71. W. Research, (2014) <https://reference.wolfram.com/language/ref/ElementData.html>.
72. T. Haisch, H. Ji, and C. Weidlich, *Electrochimica Acta*, **336**, 135573 (2020).
73. D. C. Harris, *Quantitative chemical analysis*, 7. ed., 2. print., Freeman, New York, (2007).
74. Á. Cunha, J. Martins, N. Rodrigues, and F. P. Brito, *International Journal of Energy Research*, **39**, 889–918 (2015).
75. A. Filippas, T. F. Fuller, and N. Liu, *J. Electrochem. Soc.*, **171**, 093509 (2024).
76. *Mineral commodity summaries 2024*, (2024) <https://pubs.usgs.gov/publication/mcs2024>.
77. L. F. Castañeda, F. C. Walsh, J. L. Nava, and C. Ponce De León, *Electrochimica Acta*, **258**, 1115–1139 (2017).
78. Q. Jiang, Y. Ren, Y. Yang, L. Wang, L. Dai, and Z. He, *Composites Part B: Engineering*, **242**, 110094 (2022).
79. C. T.-C. Wan, R. R. Jacquemond, Y.-M. Chiang, K. Nijmeijer, F. R. Brushett, and A. Forner-Cuenca, *Advanced Materials*, **33**, 2006716 (2021).
80. S. Chandrabose Raghu, M. Ulaganathan, T. M. Lim, and M. Skyllas Kazacos, *Journal of Power Sources*, **238**, 103–108 (2013).
81. M. Park, J. Ryu, and J. Cho, *Chemistry – An Asian Journal*, **10**, 2096–2110 (2015).

82. Q. Zhang, T. Liu, H. Zhang, and X. Li, *ACS Appl. Energy Mater.*, **4**, 3913–3920 (2021).
83. L. Wei, T. S. Zhao, L. Zeng, X. L. Zhou, and Y. K. Zeng, *Applied Energy*, **180**, 386–391 (2016).
84. H. Agarwal, E. Roy, N. Singh, P. A. A. Klusener, R. M. Stephens, and Q. T. Zhou, *Advanced Science*, **11**, 2307209 (2024).
85. D. M. Kabtamu, Y.-Z. Li, A. W. Bayeh, Y.-T. Ou, Z.-J. Huang, T.-C. Chiang, H.-C. Huang, and C.-H. Wang, *ACS Appl. Energy Mater.*, **6**, 3301–3311 (2023).
86. X. Zhang, A. Valencia, W. Li, K. Ao, J. Shi, X. Yue, R. Zhang, and W. A. Daoud, *Advanced Materials*, **36**, 2305415 (2024).
87. J. Shen, S. Liu, Z. He, and L. Shi, *Electrochimica Acta*, **151**, 297–305 (2015).
88. N. Patil, A. Mavrandonakis, C. Jérôme, C. Detrembleur, N. Casado, D. Mecerreyes, J. Palma, and R. Marcilla, *J. Mater. Chem. A*, **9**, 505–514 (2021).
89. E. Laviron, *Journal of Electroanalytical Chemistry and Interfacial Electrochemistry*, **101**, 19–28 (1979).
90. E. Sum and M. Skyllas-Kazacos, *Journal of Power Sources*, **15**, 179–190 (1985).
91. D. Reynard, H. Vrabel, C. R. Dennison, A. Battistel, and H. Girault, *ChemSusChem*, **12**, 1222–1228 (2019).
92. L. Cao, M. Skyllas-Kazacos, C. Menictas, and J. Noack, *Journal of Energy Chemistry*, **27**, 1269–1291 (2018).
93. R. M. Darling, A. Z. Weber, M. C. Tucker, and M. L. Perry, *J. Electrochem. Soc.*, **163**, A5014 (2015).
94. Y. Wen, T. P. Neville, A. Jorge Sobrido, P. R. Shearing, D. J. L. Brett, and R. Jarvis, *Journal of Power Sources*, **566**, 232861 (2023).
95. A. W. Bayeh, D. M. Kabtamu, Y.-C. Chang, G.-C. Chen, H.-Y. Chen, G.-Y. Lin, T.-R. Liu, T. H. Wondimu, K.-C. Wang, and C.-H. Wang, *J. Mater. Chem. A*, **6**, 13908–13917 (2018).
96. H. Zhou, Y. Shen, J. Xi, X. Qiu, and L. Chen, *ACS Appl. Mater. Interfaces*, **8**, 15369–15378 (2016).
97. A. W. Bayeh, D. M. Kabtamu, Y.-C. Chang, G.-C. Chen, H.-Y. Chen, G.-Y. Lin, T.-R. Liu, T. H. Wondimu, K.-C. Wang, and C.-H. Wang, *ACS Sustainable Chem. Eng.*, **6**, 3019–3028 (2018).

98. B. Li, M. Gu, Z. Nie, X. Wei, C. Wang, V. Sprenkle, and W. Wang, *Nano Lett.*, **14**, 158–165 (2014).
99. Y. Xiang and W. A. Daoud, *Electrochimica Acta*, **290**, 176–184 (2018).
100. L. Cao, M. Skyllas-Kazacos, and D.-W. Wang, *ChemElectroChem*, **4**, 1836–1839 (2017).
101. C. Yao, H. Zhang, T. Liu, X. Li, and Z. Liu, *Journal of Power Sources*, **218**, 455–461 (2012).
102. K. J. Kim, M.-S. Park, J.-H. Kim, U. Hwang, N. J. Lee, G. Jeong, and Y.-J. Kim, *Chem. Commun.*, **48**, 5455–5457 (2012).
103. Y. Xiang and W. A. Daoud, *Journal of Power Sources*, **416**, 175–183 (2019).
104. N. Yun, J. J. Park, O. O. Park, K. B. Lee, and J. H. Yang, *Electrochimica Acta*, **278**, 226–235 (2018).
105. X. Wu, H. Xu, L. Lu, H. Zhao, J. Fu, Y. Shen, P. Xu, and Y. Dong, *Journal of Power Sources*, **250**, 274–278 (2014).
106. S. Mehboob, G. Ali, H.-J. Shin, J. Hwang, S. Abbas, K. Y. Chung, and H. Y. Ha, *Applied Energy*, **229**, 910–921 (2018).
107. X. Huang, C. Wang, C. Li, M. Liao, J. Li, H. Jiang, Y. Long, X. Cheng, K. Zhang, P. Li, B. Wang, and H. Peng, *Angewandte Chemie International Edition*, **62**, e202303616 (2023).
108. L. F. Arenas, C. P. de León, and F. C. Walsh, *Electrochimica Acta*, **221**, 154–166 (2016).
109. M. van der Heijden and A. Forner Cuenca, in *Transport Phenomena and Cell Overpotentials in Redox Flow Batteries*, vol. 2, p. 480–499, Elsevier (2022)
<http://www.scopus.com/inward/record.url?scp=85151740124&partnerID=8YFLogxK>.